E-ISSN: 2147-1959

MIRT

Molecular Imaging and Radionuclide Therapy

February 2022 Volume 31 Issue 1 www.tsnm.org

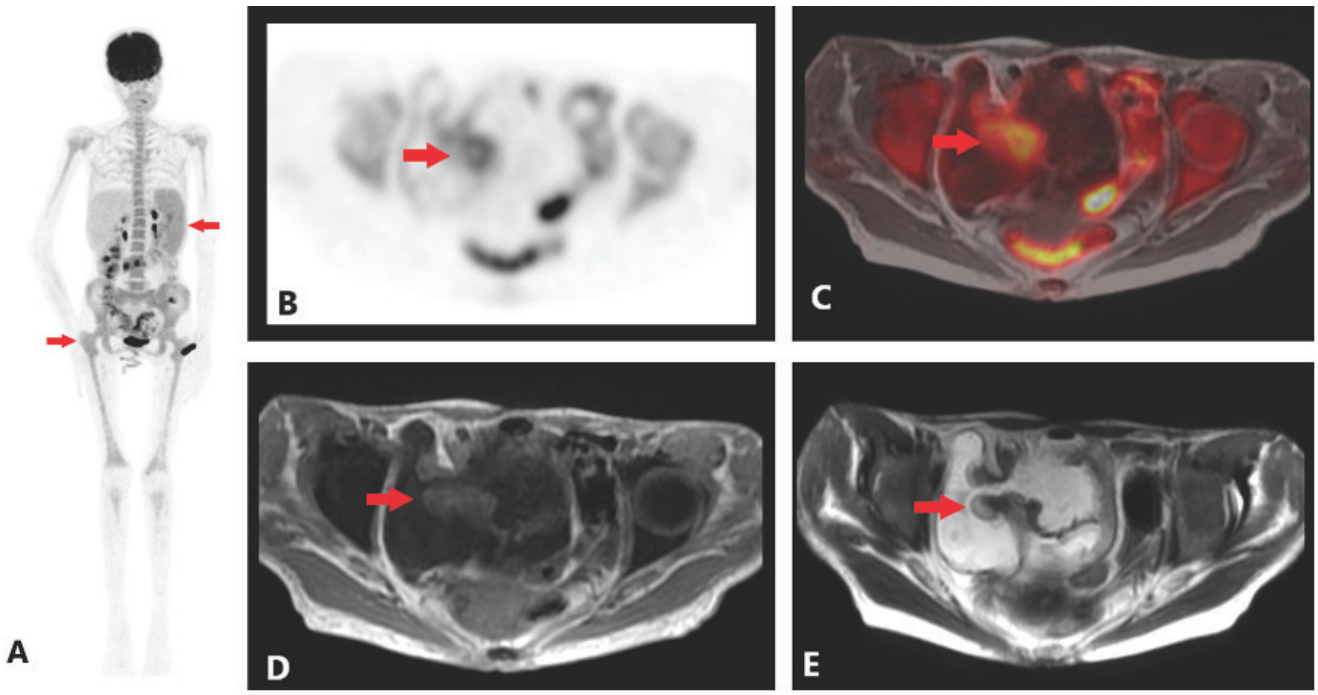

"Official Journal of the Turkish Society of Nuclear Medicine"

galenos yayınevi

TURKISH SOCIETY OF NUCLEAR MEDICINE 1975

MIRT

Molecular Imaging and Radionuclide Therapy

MIRT

Molecular Imaging and Radionuclide Therapy

Turkish Society of Nuclear Medicine
Cinnah Caddesi Pilot Sokak No: 10/12 Çankaya 06650 Ankara, Turkey **Phone:** +90 312 441 00 45 **Fax:** +90 312 441 12 95 **Web:** www.tsnm.org **E-mail:** dernekmerkezi@tsnm.org
"Formerly Turkish Journal of Nuclear Medicine"

Reviewing the articles' conformity to the publishing standards of the Journal, typesetting, reviewing and editing the manuscripts and abstracts in English, creating links to source data, and publishing process are realized by Galenos.

Galenos Publishing House
Owner and Publisher
Derya Mor
Erkan Mor

Publication Coordinator
Burak Sever

Web Coordinators
Fuat Hocalar
Turgay Akpınar

Graphics Department
Ayda Alaca
Çiğdem Birinci
Gülşah Özgül
Gülay Saday

Finance Coordinator
Sevinç Çakmak

Project Coordinators
Aysel Balta
Duygu Yıldırm
Gamze Aksoy
Gülay Akın
Hatice Sever
Melike Eren
Özlem Çelik Çekil
Pınar Akpınar
Rabia Palazoğlu

Research&Development
Melisa Yiğitoğlu
Nihan Karamanlı

Digital Marketing Specialist
Ümit Topçuoğlu

Publisher Contact
Address: Molla Gürani Mah. Kaçamak Sk. No: 21/1
34093 İstanbul, Turkey
Phone: +90 (212) 621 99 25 **Fax:** +90 (212) 621 99 27
E-mail: info@galenos.com.tr/yayin@galenos.com.tr
Web: www.galenos.com.tr
Publisher Certificate Number: 14521

Online Publication Date: February 2022
ISSN: 2146-1414 **E-ISSN:** 2147-1959
International scientific journal published quarterly.

MIRT

Molecular Imaging and Radionuclide Therapy

ABOUT US

Molecular Imaging and Radionuclide Therapy (formerly Turkish Journal of Nuclear Medicine) is the official publication of Turkish Society of Nuclear Medicine.

Focus and Scope

Molecular Imaging and Radionuclide Therapy (Mol Imaging Radionucl Ther, MIRT) is a double-blind peer-review journal published in English language. It publishes original research articles, invited reviews, editorials, short communications, letters, consensus statements, guidelines and case reports with a literature review on the topic, in the field of molecular imaging, multimodality imaging, nuclear medicine, radionuclide therapy, radiopharmacy, medical physics, dosimetry and radiobiology. MIRT is published three times a year (February, June, October). Audience: Nuclear medicine physicians, medical physicists, radiopharmaceutical scientists, radiobiologists.

The editorial policies are based on the "Recommendations for the Conduct, Reporting, Editing, and Publication of Scholarly Work in Medical Journals (ICMJE Recommendations)" by the International Committee of Medical Journal Editors (2016, archived at http://www.icmje.org/) rules.

Molecular Imaging and Radionuclide Therapy is indexed in **Pubmed, Pubmed Central (PMC), Emerging Sources Citation Index (ESCI), TUBITAK-ULAKBIM, DOAJ, Scopus, Gale/Cengage Learning, EBSCO databases, Embase, ProQuest Health & Medical Complete, CINAHL, Index Copernicus, J-Gate, IdealOnline, ROOT INDEXING, Türkiye Atıf Dizini-Turkiye Citation Index, Turk Medline, EuroPub, Hinari, GOALI, ARDI, OARE** and **AGORA.**

Open Access Policy

This journal provides immediate open access to its content on the principle that making research freely available to the public supports a greater global exchange of knowledge.

Open Access Policy is based on rules of Budapest Open Access Initiative (BOAI) (http://www.budapestopenaccessinitiative.org/). By "open access" to [peer-reviewed research literature], we mean its free availability on the public internet, permitting any users to read, download, copy, distribute, print, search, or link to the full texts of these articles, crawl them for indexing, pass them as data to software, or use them for any other lawful purpose, without financial, legal, or technical barriers other than those inseparable from gaining access to the internet itself. The only constraint on reproduction and distribution, and the only role for copyright in this domain, should be to give authors control over the integrity of their work and the right to be properly acknowledged and cited.

Subscription Information

Manuscripts can only be submitted electronically through the Journal Agent website (http://www.journalagent.com/mirt/?plng=eng) after creating an account. This system allows online submission and review.

All published volumes in full text can be reached free of charge through the website http://mirt.tsnmjournals.org

Copyright Statement

Turkish Society of Nuclear Medicine holds the international copyright of all the content published in the journal.

Republication and reproduction of images or tables in any published material should be done with proper citation of source providing authors names; article title; journal title; year (volume) and page of publication; copyright year of the article.

The author(s) hereby affirms that the manuscript submitted is original, that all statement asserted as facts are based on author(s) careful investigation and research for accuracy, that the manuscript does not, in whole or part, infringe any copyright, that it has not been published in total or in part and is not being submitted or considered for publication in total or in part elsewhere.

Completed Copyright Statement form should be submitted to the online article system.

By signing this form,

1. Each author acknowledge that he/she participated in the work in a substantive way and is prepared to take public responsibility for the work.

2. Each author further affirms that he or she has read and understands the "Ethical Guidelines for Publication of Research".

3. The author(s), in consideration of the acceptance of the manuscript for publication, does hereby assign and transfer to the Molecular Imaging and Radionuclide Therapy all of the rights and interest in and the copyright of the work in its current form and in any form subsequently revised for publication and/or electronic dissemination.

Instructions for Authors

Instructions for authors are published in the journal and on the website http://mirt.tsnmjournals.org

Material Disclaimer

Scientific and legal responsibilities pertaining to the papers belong to the authors. Contents of the manuscripts and accuracy of references are also the author's responsibility. The Turkish Society of Nuclear Medicine, the Editor, the Editorial Board or the publisher do not accept any responsibility for opinions expressed in articles.

Financial expenses of the journal are covered by Turkish Society of Nuclear Medicine.

Correspondence Address

Editor in Chief Prof. Murat Fani Bozkurt, MD, FEBNM Hacettepe University, Medical School, Department of Nuclear Medicine, Ankara, Turkey

E-mail: fanibozkurt@gmail.com

Web page: http://mirt.tsnmjournals.org/

Publisher Corresponding Address

Galenos Yayınevi Tic. Ltd. Şti.
Address: Molla Gürani Mah. Kaçamak Sk. No: 21/1 34093 Fındıkzade, İstanbul, Turkey
Phone: +90 212 621 99 25
Fax: +90 212 621 99 27
E-mail: info@galenos.com.tr

MIRT

Molecular Imaging and Radionuclide Therapy

INSTRUCTIONS TO AUTHORS

Molecular Imaging and Radionuclide Therapy (Mol Imaging Radionucl Ther, MIRT) publishes original research articles, short communications, invited reviews, editorials, case reports with a literature review on the topic, interesting images, consensus statements, guidelines, letters in the field of molecular imaging, multimodality imaging, nuclear medicine, radionuclide therapy, radiopharmacy, medical physics, dosimetry and radiobiology. MIRT is published by the Turkish Society of Nuclear Medicine three times a year (February, June, October).

Molecular Imaging and Radionuclide Therapy does not charge any article submission or processing fees.

GENERAL INFORMATION

MIRT commits to rigorous peer review, and stipulates freedom from commercial influence, and promotion of the highest ethical and scientific standards in published articles. Neither the Editor(s) nor the publisher guarantees, warrants or endorses any product or service advertised in this publication. All articles are subject to review by the editors and peer reviewers. If the article is accepted for publication, it may be subjected to editorial revisions to aid clarity and understanding without changing the data presented.

Manuscripts must be written in English and must meet the requirements of the journal. The journal is in compliance with the uniform requirements for manuscripts submitted to biomedical journals published by the International Committee of Medical Journal Editors (NEJM 1997; 336:309-315, updated 2016). Manuscripts that do not meet these requirements will be returned to the author for necessary revision before the review. Authors of manuscripts requiring modifications have a maximum of two months to resubmit the revised text. Manuscripts returned after this deadline will be treated as new submissions.

It is the authors' responsibility to prepare a manuscript that meets ethical criteria. The Journal adheres to the principles set forth in the Helsinki Declaration October 2013 (https://www.wma.net/policies-post/wma-declaration-of-helsinki-ethical-principles-for-medical-research-involving-human-subjects/) and holds that all reported research involving "Human beings" conducted in accordance with such principles.

Reports describing data obtained from research conducted in human participants must contain a statement in the MATERIALS AND METHODS section indicating approval by the ethical review board (including the approval number) and affirmation that INFORMED CONSENT was obtained from each participant.

All manuscripts reporting experiments using animals must include a statement in the MATERIALS AND METHODS section giving assurance that all animals have received humane care in compliance with the Guide for the Care and Use of Laboratory Animals (www.nap.edu) and indicating approval by the ethical review board.

If the study should have ethical approval, authors asked to provide ethical approval in order to proceed the review process. If they provide approval, review of the manuscript will continue.

In case report(s) and interesting image(s) a statement regarding the informed consent of the patients should be included in the manuscript and the identity of the patient(s) should be hidden.

Subjects must be identified only by number or letter, not by initials or names. Photographs of patients' faces should be included only if scientifically relevant. Authors must obtain written consent from the patient for use of such photographs. In cases of image media usage that potentially expose patients' identity requires obtaining permission for publication from the patients or their parents/guardians.

If the proposed publication concerns any commercial product, the author must include in the cover letter a statement indicating that the author(s) has (have) no financial or other interest with the product or explaining the nature of any relations (including consultancies) between the author(s) and editor the manufacturer or distributor of the product.

All submissions will be screened by Crossref Smilarity Check powered by "iThenticate". Manuscripts with an overall similarity index of greater than 25%, or duplication rate at or higher than 5% with a single source will be returned back to authors.

MANUSCRIPT CATEGORIES

1. Original Articles

2. Short Communications are short descriptions of focused studies with important, but very straightforward results.

3. Reviews address important topics in the field. Authors considering the submission of uninvited reviews should contact the editor in advance to determine if the topic that they propose is of current potential interest to the Journal. Reviews will be considered for publication only if they are written by authors who have at least three published manuscripts in the international peer reviewed journals and these studies should be cited in the review. Otherwise only invited reviews will be considered for peer review from qualified experts in the area.

4. Editorials are usually written by invitation of the editor by the editors on current topics or by the reviewers involved in the evaluation of a submitted manuscript and published concurrently with that manuscript.

5. Case Report and Literature Reviews are descriptions of a case or small number of cases revealing a previously undocumented disease process, a unique unreported manifestation or treatment of a known disease process, unique unreported complications of treatment regimens or novel and important insights into a condition's pathogenesis, presentation, and/or management. The journal's policy is to accept case reports only if it is accompanied by a review of the literature on the related topic. They should include an adequate number of images and figures.

6. Interesting Image

One of the regular parts of Molecular Imaging and Radionuclide Therapy is a section devoted to interesting images. Interesting image(s) should describe case(s) which are unique and include interesting findings adding insights into the interpretation of patient images, a condition's pathogenesis, presentation, and/or management.

7. Consensus Statements or Guidelines may be submitted by professional societies. All such submissions will be subjected to peer review, must be modifiable in response to criticisms, and will be published only if they meet the Journal's usual editorial standards.

8. Letters to the Editor may be submitted in response to work that has been published in the Journal. Letters should be short commentaries related to specific points of agreement or disagreement with the published work.

Note on Prior Publication

Articles are accepted for publication on the condition that they are original, are not under consideration by another journal, or have not been previously published. Direct quotations, tables, or illustrations that have appeared in

MIRT
Molecular Imaging and Radionuclide Therapy

copyrighted material must be accompanied by written permission for their use from the copyright owner and authors. Materials previously published in whole or in part shall not be considered for publication. At the time of submission, authors must report that the manuscript has not been published elsewhere. Abstracts or posters displayed at scientific meetings need not be reported.

MANUSCRIPT SUBMISSION PROCEDURES

MIRT only accepts electronic manuscript submission at the web site http://www.journalagent.com/mirt/. After logging on to the website Click the 'online manuscript submission' icon. All corresponding authors should be provided with a password and a username after entering the information required. If you already have an account from a previous submission, enter your username and password to submit a new or revised manuscript. If you have forgotten your username and/or password, please send an e-mail to the editorial office for assistance. After logging on to the article submission system please read carefully the directions of the system to give all needed information and attach the manuscript, tables and figures and additional documents.

All Submissions Must Include:

1. Completed Copyright Assignment & Disclosure of Potential Conflict of Interest Form; This form should be downloaded from the website (provided in the author section), filled in thoroughly and uploaded to the website during the submission.
2. All manuscripts describing data obtained from research conducted in human participants must be accompanied with an approval document by the ethical review board.
3. All manuscripts reporting experiments using animals must include approval document by the animal ethical review board.
4. All submissions must include the authorship contribution form which is signed by all authors.

Authors must complete all online submission forms. If you are unable to successfully upload the files please contact the editorial office by e-mail.

MANUSCRIPT PREPARATION

General Format

The Journal requires that all submissions be submitted according to these guidelines:

- Text should be double spaced with 2.5 cm margins on both sides using 12-point type in Times Roman font.
- All tables and figures must be placed after the text and must be labeled.
- Each section (abstract, text, references, tables, figures) should start on a separate page.
- Manuscripts should be prepared as a word document (*.doc) or rich text format (*.rtf).
- Please make the tables using the table function in Word.
- Abbreviations should be defined in parenthesis where the word is first mentioned and used consistently thereafter.
- Results should be expressed in metric units. Statistical analysis should be done accurately and with precision. Please consult a statistician if necessary.
- Authors' names and institutions should not be included in the manuscript text and should be written only in the title page.

Title Page

The title page should be a separate form from the main text and should include the following:

- Full title (in English and in Turkish). Turkish title will be provided by the editorial office for the authors who are not Turkish speakers.
- Authors' names and institutions.
- Short title of not more than 40 characters for page headings.
- At least three and maximum eight keywords. (in English and in Turkish). Do not use abbreviations in the keywords. Turkish keywords will be provided by the editorial office for the authors who are not Turkish speakers. If you are not a native Turkish speaker, please reenter your English keywords to the area provided for the Turkish keywords. English keywords should be provided from http://www.nlm.nih.gov/mesh (Medical Subject Headings) while Turkish keywords should be provided from http://www.bilimterimleri.com.
- Word count (excluding abstract, figure legends and references).
- Corresponding author's e-mail and address, telephone and fax numbers.
- Name and address of person to whom reprint requests should be addressed.

Original Articles

Authors are required to state in their manuscripts that ethical approval from an appropriate committee and informed consents of the patients were obtained.

Original Articles should be submitted with a structured abstract of no more than 250 words. All information reported in the abstract must appear in the manuscript. The abstract should not include references. Please use complete sentences for all sections of the abstract. Structured abstract should include background, objective, methods, results and conclusions. Turkish abstract will be provided by the editorial office for the authors who are not Turkish speakers. If you are not a native Turkish speaker, please reenter your English abstract to the area provided for the Turkish abstract.

- Introduction
- Materials and Methods
- Results
- Discussion
- Study Limitations
- Conclusion

May be given for contributors who are not listed as authors, or for grant support of the research.

References should be cited in numerical order (in parentheses) in the text and listed in the same numerical order at the end of the manuscript on a separate page or pages. The author is responsible for the accuracy of references. Examples of the reference style are given below. Further examples will be found in the articles describing the Uniform Requirements for Manuscripts Submitted to Biomedical Journals (Ann Intern Med.1988; 208:258-265, Br Med J. 1988; 296:401-405). The titles of journals should be abbreviated according to the style used in the Index Medicus. Journal Articles and Abstracts: Surnames and initials of author's name, title of the article, journal name, date, volume number, and pages. All authors should be listed regardless of number. The citation of unpublished papers, observations or personal communications is not permitted. Citing an abstract is not recommended. Books: Surnames and initials of author's names, chapter title, editor's name, book title, edition, city, publisher, date and pages.

MIRT
Molecular Imaging and Radionuclide Therapy

Sample References

Journal Article: Sayit E, Söylev M, Capa G, Durak I, Ada E, Yilmaz M. The role of technetium-99m-HMPAO-labeled WBC scintigraphy in the diagnosis of orbital cellulitis. Ann Nucl Med 2001;15:41-44.

Erselcan T, Hasbek Z, Tandogan I, Gumus C, Akkurt I. Modification of Diet in Renal Disease equation in the risk stratification of contrast induced acute kidney injury in hospital inpatients. Nefrologia 2009 doi: 10.3265/Nefrologia.2009.29.5.5449.en.full.

Article in a journal published ahead of print: Ludbrook J. Musculovenous pumps in the human lower limb. Am Heart J 2009;00:1-6. (accessed 20 February 2009).

Lang TF, Duryea J. Peripheral Bone Mineral Assessment of the Axial Skeleton: Technical Aspects. In: Orwoll ES, Bliziotes M (eds). Osteoporosis: Pathophsiology and Clinical Management. New Jersey, Humana Pres Inc, 2003;83-104.

Books: Greenspan A. Orthopaedic Radiology a Pratical Approach. 3th ed. Philadelphia, Lippincott Williams Wilkins 2000, 295-330.

Website: Smith JR. 'Choosing Your Reference Style', Online Referencing 2(3), http://orj.sagepub.com (200, accessed October 2008).

- Tables

Tables must be constructed as simply as possible. Each table must have a concise heading and should be submitted on a separate page. Tables must not simply duplicate the text or figures. Number all tables in the order of their citation in the text. Include a title for each table (a brief phrase, preferably no longer than 10 to 15 words). Include all tables in a single file following the manuscript.

– Figure Legends

Figure legends should be submitted on a separate page and should be clear and informative.

– Figures

Number all figures (graphs, charts, photographs, and illustrations) in the order of their citation in the text. At submission, the following file formats are acceptable: AI, EMF, EPS, JPG, PDF, PPT, PSD, TIF. Figures may be embedded at the end of the manuscript text file or loaded as separate files for submission. All images MUST be at or above intended display size, with the following image resolutions: Line Art 800 dpi, Combination (Line Art + Halftone) 600 dpi, Halftone 300 dpi. Image files also must be cropped as close to the actual image as possible.

Short Communications:

Short communications should be submitted with a structured abstract of no more than 200 words. These manuscripts should be no longer than 2000 words, and include no more than two figures and tables and 20 references. Other rules which the authors are required to prepare and submit their manuscripts are the same as described above for the original articles.

Invited Review Articles:

- Title page (see above)
- Abstract: Maximum 250 words; without structural divisions; in English and in Turkish . Turkish abstract will be provided by the editorial office for the authors who are not Turkish speakers. If you are not a native Turkish speaker, please reenter your English abstract to the area provided for the Turkish abstract.
- Text
- Conclusion
- Acknowledgements (if any)
- References

Editorial:

- Title page (see above)
- Abstract: Maximum 250 words; without structural divisions; in English and in Turkish. Turkish abstract will be provided by the editorial office for the authors who are not Turkish speakers. If you are not a native Turkish speaker, please re enter your English abstract to the area provided for the Turkish abstract.
- Text
- References

Case Report and Literature Review

- Title page (see above)
- Abstract: Approximately 100-150 words; without structural divisions; in English and in Turkish. Turkish abstract will be provided by the editorial office for the authors who are not Turkish speakers. If you are not a native Turkish speaker, please re-enter your English abstract to the area provided for the Turkish abstract.
- Introduction
- Case report
- Literature Review and Discussion
- References

Interesting Image:

No manuscript text is required. Interesting Image submissions must include the following:

Title Page: (see Original article section)

Abstract: Approximately 100-150 words; without structural divisions; in English and in Turkish. Turkish abstract will be provided by the editorial office for the authors who are not Turkish speakers. If you are not a native Turkish speaker, please re-enter your English abstract to the area provided for the Turkish abstract.

Image(s): The number of images is left to the discretion of the author. (See Original article section)

Figure Legend: Reference citations should appear in the legends, not in the abstract. Since there is no manuscript text, the legends for illustrations should be prepared in considerable detail but should be no more than 500 words total. The case should be presented and discussed in the Figure legend section.

References: Maximum eight references (see original article section).

Letters to the Editor:

- Title page (see above)
- Short comment to a published work, no longer than 500 words, no figures or tables.
- References no more than five.

Consensus Statements or Guidelines: These manuscripts should typically be no longer than 4000 words and include no more than six figures and tables and 120 references.

Proofs and Reprints

Proofs and a reprint orders are sent to the corresponding author. The author should designate by footnote on the title page of the manuscript the name and

MIRT
Molecular Imaging and Radionuclide Therapy

address of the person to whom reprint requests should be directed. The manuscript when published will become the property of the journal.

Archiving

The editorial office will retain all manuscripts and related documentation (correspondence, reviews, etc.) for 12 months following the date of publication or rejection.

Submission Preparation Checklist

As part of the submission process, authors are required to check off their submission's compliance with all of the following items, and submissions may be returned to authors that do not adhere to these guidelines.

1. The submission has not been previously published, nor is it before another journal for consideration (or an explanation has been provided in Comments to the Editor).
2. The submission file is in Microsoft Word, RTF, or WordPerfect document file format. The text is double-spaced; uses a 12-point font; employs italics, rather than underlining (except with URL addresses); and the location for all illustrations, figures, and tables should be marked within the text at the appropriate points.
3. Where available, URLs for the references will be provided.
4. All authors should be listed in the references, regardless of the number.
5. The text adheres to the stylistic and bibliographic requirements outlined in the Author Guidelines, which is found in About the Journal.
6. English keywords should be provided from http://www.nlm.nih.gov/mesh(Medical Subject Headings), while Turkish keywords should be provided fromhttp://www.bilimterimleri.com
7. The title page should be a separate document from the main text and should be uploaded separately.
8. The "Affirmation of Originality and Assignment of Copyright/The Disclosure Form for Potential Conflicts of Interest Form" and Authorship Contribution Form should be downloaded from the website, filled thoroughly and uploaded during the submission of the manuscript.

TO AUTHORS

Copyright Notice

The author(s) hereby affirms that the manuscript submitted is original, that all statement asserted as facts are based on author(s) careful investigation and research for accuracy, that the manuscript does not, in whole or part, infringe any copyright, that it has not been published in total or in part and is not being submitted or considered for publication in total or in part elsewhere. Completed Copyright Assignment & Affirmation of Originality Form will be uploaded during submission. By signing this form;

1. Each author acknowledges that he/she participated in the work in a substantive way and is prepared to take public responsibility for the work.
2. Each author further affirms that he or she has read and understands the "Ethical Guidelines for Publication of Research".
3. The author(s), in consideration of the acceptance of the manuscript for publication, does hereby assign and transfer to the Molecular Imaging and Radionuclide Therapy all of the rights and interest in and the copyright of the work in its current form and in any form subsequently revised for publication and/or electronic dissemination.

Privacy Statement

The names and email addresses entered in this journal site will be used exclusively for the stated purposes of this journal and will not be made available for any other purpose or to any other party.

Peer Review Process

1. The manuscript is assigned to an editor, who reviews the manuscript and makes an initial decision based on manuscript quality and editorial priorities.
2. For those manuscripts sent for external peer review, the editor assigns at least two reviewers to the manuscript.
3. The reviewers review the manuscript.
4. The editor makes a final decision based on editorial priorities, manuscript quality, and reviewer recommendations.
5. The decision letter is sent to the author.

Contact Address

All correspondence should be directed to the Editorial Office:
Cinnah Caddesi Pilot Sokak No:10/12 06650 Çankaya / Ankara, Turkey
Phone: +90 312 441 00 45
Fax: +90 312 441 12 97
E-mail: info@tsnmjournals.org

MIRT

Molecular Imaging and Radionuclide Therapy

CONTENTS

Original Articles

MIRT
Molecular Imaging and Radionuclide Therapy

CONTENTS

Interesting Images

Original Article
Mol Imaging Radionucl Ther 2022;31:1-6 DOI:10.4274/mirt.galenos.2021.63308

Relative Efficacy of ^{225}Ac-PSMA-617 and ^{177}Lu-PSMA-617 in Prostate Cancer Based on Subcellular Dosimetry

Prostat Kanserinde ^{225}Ac-PSMA-617 ve ^{177}Lu-PSMA-617'nin Subsellüler Dozimetriye Dayalı Göreceli Etkinliği

Hwan Lee

University of Pennsylvania Perelman School of Medicine, Department of Radiology, Philadelphia, United States

Abstract

Objectives: Radionuclide therapy targeting prostate-specific membrane antigen (PSMA) with alpha-emitting ^{225}Ac-PSMA-617 has shown clinical efficacy even in cases of failed therapy with beta-emitting ^{177}Lu-PSMA-617. We investigated the efficacy of ^{225}Ac-PSMA-617 relative to ^{177}Lu-PSMA-617 using subcellular dosimetry.

Methods: A 3-dimensional model of prostate cancer was constructed. For each decay, the absorbed and equivalent radiation dose to the cell nuclei was calculated. The relative efficacy per administered activity was calculated by taking into account the differences in residence time and tumor uptake.

Results: As the tumor size increased, the absorbed dose from ^{225}Ac-PSMA-617 increased linearly (R^2: 0.99) and reached an asymptote near the maximum alpha range (85 µm), whereas the absorbed dose from ^{177}Lu-PSMA-617 continued to increase linearly (R^2: 0.99). The equivalent dose per decay was 2,320, 2,900, and 823-fold higher in favor of ^{225}Ac-PSMA-617 compared to ^{177}Lu-PSMA-617 in a single cell, 100 µm-radius micrometastasis, and macroscopic tumor, respectively. Per administered activity, the relative efficacy of ^{225}Ac-PSMA-617 compared to ^{177}Lu-PSMA-617 in respective tumor sizes was at least 3,480, 4,350, and 1,230-fold higher, and possibly 11,800, 14,900, and 4,200-fold higher considering differences in tumor uptake.

Conclusion: At commonly administered 1,000-fold lower activity of ^{225}Ac-PSMA-617 relative to ^{177}Lu-PSMA-617, the equivalent radiation dose deposited by ^{225}Ac-PSMA-617 is higher in measurable disease and much higher in microscopic disease compared to ^{177}Lu-PSMA-617.

Keywords: Prostate cancer, prostate-specific membrane antigen, radionuclide therapy, dosimetry, alpha particle, beta particle

Öz

Amaç: Alfa yayıcı ^{225}Ac-PSMA-617 ile prostata özgü membran antijenini (PSMA) hedefleyen radyonüklit tedavi, beta yayıcı ^{177}Lu-PSMA-617 ile tedavinin başarısız olduğu durumlarda bile klinik etkinlik göstermiştir. ^{177}Lu-PSMA-617'ye göre ^{225}Ac-PSMA-617'nin etkinliğini, subsellüler dozimetri kullanarak araştırdık.

Yöntem: Prostat kanserinin 3 boyutlu bir modeli oluşturuldu. Her bozunma için hücre çekirdeğine absorbe olan ve eşdeğer radyasyon dozu hesaplandı. Uygulanan aktivite başına göreceli etkinlik, kalış süresi ve tümör tutulumundaki farklılıklar dikkate alınarak hesaplandı.

Bulgular: Tümör boyutu arttıkça, ^{225}Ac-PSMA-617'den absorbe olan doz doğrusal olarak artıp (R^2: 0,99) maksimum alfa aralığına (85 µm) yakın bir asimptota ulaşırken, ^{177}Lu-PSMA-617'den absorbe olan doz doğrusal olarak artmaya devam etti (R^2: 0,99). Bozunma başına eşdeğer doz, tek bir hücrede, 100 µm yarıçaplı mikrometastazda ve makroskopik tümörde, ^{177}Lu-PSMA-617'ye kıyasla ^{225}Ac-PSMA-617 lehine sırasıyla 2.320, 2.900 ve 823 kat daha yüksekti. Uygulanan her aktivite için, ^{177}Lu-PSMA-617'ye kıyasla ^{225}Ac-PSMA-617'nin görece etkinliği ilgili tümör boyutlarında en az 3.480, 4.350 ve 1.230 kat ve tümör alımındaki farklılıklar dikkate alındığında muhtemelen 11.800, 14.900 ve 4.200 kat daha yüksekti.

Address for Correspondence: Hwan Lee MD, University of Pennsylvania Perelman School of Medicine, Department of Radiology, Philadelphia, United States
Phone: 215-662-3264 **E-mail:** hwan.lee@pennmedicine.upenn.edu ORCID ID: orcid.org/0000-0001-6950-1207
Received: 24.08.2021 **Accepted:** 16.10.2021

Sonuç: Genel kullanımda ^{177}Lu-PSMA-617'ye göre 1.000 kat daha düşük aktivitede uygulanan ^{225}Ac-PSMA-617'in oluşturduğu eşdeğer radyasyon dozu, ^{177}Lu-PSMA-617 ile karşılaştırıldığında ölçülebilir hastalıkta ve mikroskobik hastalıkta çok daha yüksektir.

Anahtar kelimeler: Prostat kanseri, prostata özgü membran antijeni, radyonüklid tedavi, dozimetri, alfa parçacığı, beta parçacığı

Introduction

Metastatic castration-resistant prostate cancer (mCRPC) carries a poor prognosis despite multiple approved therapies with antiproliferative, immunologic, and endocrine effects (1). Targeted radionuclide therapy for mCRPC has gained much interest secondary to the development of small molecules and antibodies that target the prostate-specific membrane antigen (PSMA) (2). PSMA is a surface protein that is overexpressed in over 90% of prostate cancer cases, including mCRPC, and is a promising molecular target for radionuclide delivery based on the clinical success of PSMA-targeted imaging (3). PSMA-targeted radionuclide therapy was shown to successfully treat mCRPC with efficacy on both visceral and osseous metastases (4).

The most commonly used radionuclide in PSMA-targeted therapy is the beta emitter ^{177}Lu-PSMA-617 (4). With a half-life of 6.6 days, ^{177}Lu emits low-linear energy transfer (LET) beta particles with a maximum energy of 0.5 MeV and a soft tissue range of 1.7 mm (5). An alternative strategy in PSMA-targeted radionuclide therapy is the use of an alpha emitter such as ^{225}Ac-PSMA-617 (6). Alpha particles deposit MeV-scale energy within <100 μm range as a form of high-LET radiation, efficiently causing double-strand DNA breaks that lead to cytotoxicity (7). Specifically, ^{225}Ac decays with a half-life of 9.9 days to produce four alpha particles with 47-85 μm range (6). While there is relative paucity of pre-clinical and clinical literature on ^{225}Ac-PSMA-617 compared to ^{177}Lu-PSMA-617, the limited available literature on ^{225}Ac-PSMA-617 shows a higher biochemical response rate with survival benefit even among patients who previously failed ^{177}Lu-PSMA-617 therapy (8,9).

Clinical studies that involve ^{177}Lu-PSMA-617 generally have used 4-9 GBq of radioactivity compared to 4-8 MBq for ^{225}Ac-PSMA-617 therapy (6,10). The common use of a 1,000-fold lower dose for ^{225}Ac-PSMA-617 is based on empirical results and extrapolation of organ-level ^{177}Lu-PSMA-617 dosimetry (11,12). From a physics perspective, the required radioactivity of ^{225}Ac-PSMA-617 vs. ^{177}Lu-PSMA-617 to produce a comparable cytotoxic effect on the cellular level remains to be investigated.

The present study used subcellular dosimetry in a 3-dimensional prostate cancer model to calculate the relative efficacy of ^{225}Ac-PSMA-617 vs. ^{177}Lu-PSMA-617 for the delivery of absorbed and equivalent radiation doses to the cell nuclei of a single cell, micrometastasis, and macroscopic tumor. An estimation of the equivalent administered doses for the two radiopharmaceuticals was then performed.

Materials and Methods

Biophysical Modeling

Based on the existing literature, several assumptions were made for modeling the radiolabeled PSMA-617 therapy. Once bound to the PSMA protein on the cell surface, the radiolabeled PSMA-617 molecules were considered internalized (Figure 1A) (13). The activity was then considered uniformly distributed within the cytoplasm, based on the endosomal localization of the intracellular PSMA-radiotherapeutic complex (14).

Each prostate cancer cell was modeled as a sphere that contains a concentric, spherical nucleus (Figure 1B) (15). The cellular and nuclear diameters of 14 and 10 μm were used, respectively, based on the previously published cultured human prostate cancer cell measurements (16). For multicellular dosimetry, prostate cancer cells were considered densely packed in a 3-dimensional face-centered cubic structure with maximal packing efficiency, where each cell was in contact with 12 adjacent cells as previously illustrated (17). The distance between a given cell and each shell of neighboring cells was calculated up to the desired tumor size using a sub-lattice approach (18).

Subcellular Dosimetry

The physical decay data of the ^{225}Ac and ^{177}Lu were obtained from the MIRD Radionuclide Data and Decay Schemes (19). MIRDcell v2.1 (Newark, NJ) was used to obtain the self and cross-dose S values for the decay of ^{225}Ac and ^{177}Lu, including the daughter isotopes of ^{225}Ac (15). The contribution from every cell in the tumor model was considered for cross-dose calculation. The radiation dose to the cell nucleus at the center of the tumor was used to estimate the cytotoxic efficacy for one decay event in each tumor cell. The conversion from absorbed dose to equivalent dose was made using the value of 5 for the relative biological effectiveness (RBE) of alpha particles (11,20).

The equivalent dose per decay was first scaled by the physical half-lives of the radionuclides to account for the

difference in residence time to compare the equivalent dose per administered activity. The difference in the tumor cell uptake per administered activity was estimated by the relative tumor uptake level between ^{225}Ac-PSMA-617 and ^{177}Lu-PSMA-617. The tumor uptake levels were based on the recently published *ex vivo* biodistribution work in the RM-1 mouse model of prostate cancer with 100% PSMA expression (21).

Subcellular dosimetry was first performed in a single cell to compare the relative efficacy of ^{225}Ac-PSMA-617 and ^{177}Lu-PSMA-617 in circulating tumor cells. Then, micrometastatic disease was modeled up to 100 μm diameter. Finally, in a macroscopic tumor (>2 mm radius), the results of subcellular dosimetry were compared against conventional macroscopic dosimetry based on uniform distribution of activity within a spherical volume (Figure 1B).

The study did not involve any statistical analysis.

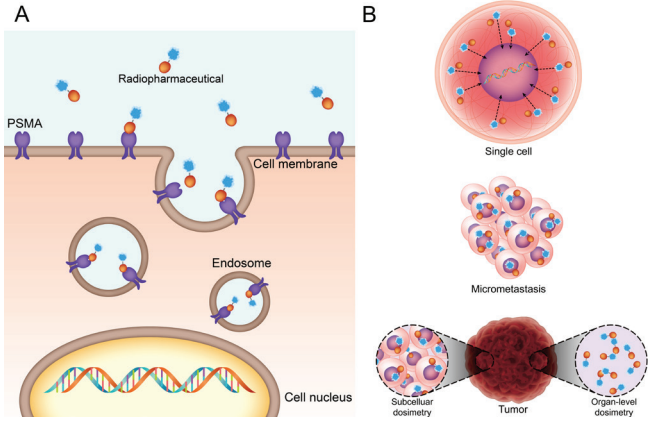

Figure 1. A) A diagram illustrating the uptake of PSMA-targeting radiopharmaceuticals into the cytoplasmic endosomes. B) A densely packed 3-dimensional model of prostate cancer for subcellular dosimetry of PSMA-targeted radionuclide therapy in a single cell, micrometastasis, and macroscopic tumor, with comparison to the conventional organ-level dosimetry in the macroscopic tumor

PSMA: Prostate-specific membrane antigen

Results

Single-cell Dosimetry

For each decay event, ^{225}Ac-PSMA-617 deposited 0.129 Gy in the nucleus resulting in a 464-fold higher absorbed dose compared to ^{177}Lu-PSMA-617, which deposited 2.78×10^{-4} Gy. The equivalent dose per decay was 2,320-fold higher in favor of ^{225}Ac-PSMA-617 taking into account the RBE of 5.

Micrometastasis

As the size of the micrometastasis increased, the absorbed dose from ^{225}Ac-PSMA-617 initially linearly increased up to approximately 50 μm in radius (R^2: 0.99), and then reached an asymptote at approximately 85 μm to reach 2.06 Gy per decay in each tumor cell (Figure 2A). In comparison, the absorbed dose from ^{177}Lu-PSMA-617 continued to increase linearly (R^2: 0.99) with the tumor size and reached 3.55×10^{-3} Gy per decay at 100 μm radius (Figure 2B). In relative scale, the equivalent dose per decay was over 4,000-fold higher for ^{225}Ac-PSMA-617 compared to ^{177}Lu-PSMA-617 up to 60 μm radius (Figure 2C). As the tumor size increased, the relative dose difference between the

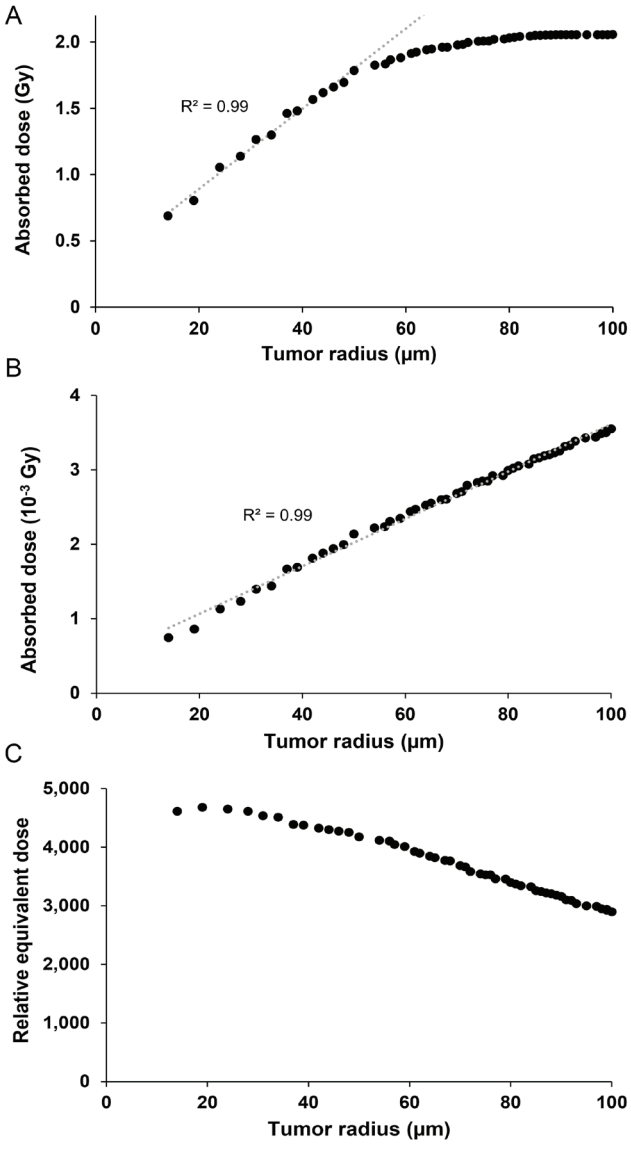

Figure 2. Radiation dose deposition per decay/cell in micrometastases of various sizes by ^{225}Ac-PSMA-617 (A) and ^{177}Lu-PSMA-617 (B), with relative equivalent dose comparison (^{225}Ac: ^{177}Lu) (C)

PSMA: Prostate-specific membrane antigen

two radiopharmaceuticals gradually decreased, reaching a 2,900-fold difference at 100 μm tumor radius.

Macroscopic Tumor

The absorbed dose per decay in each tumor cell was 165-fold higher for ^{225}Ac-PSMA-617 (2.06 Gy) compared to ^{177}Lu-PSMA-617 (1.25×10^{-2} Gy), which translated to an 823-fold difference in equivalent dose with RBE of 5, based on subcellular dosimetry. Using the conventional dosimetry, ^{225}Ac-PSMA-617 and ^{177}Lu-PSMA-617 deposited 2.25 Gy and 1.26×10^{-2} Gy per decay, resulting in a 178-fold and 892-fold difference in the absorbed and equivalent doses, respectively.

Relative Equivalent Dose Per Administered Activity

The longer physical half-life of ^{225}Ac conferred 50% longer residence time to ^{225}Ac-PSMA-617 compared to ^{177}Lu-PSMA-617. After scaling using this factor, the relative differences in equivalent dose per administered activity (^{225}Ac-PSMA-617 vs. ^{177}Lu-PSMA-617) were 3,480-fold, 4,350-fold, and 1,230-fold for a single cell, 100 μm-radius micrometastasis, and macroscopic tumor, respectively. Then, using 3.4 times higher uptake per administered activity for ^{225}Ac-PSMA-617 (4.66% injected dose/g of tumor) compared to ^{177}Lu-PSMA-617 (1.36% injected dose/g of tumor) (21), the relative differences in equivalent dose per administered activity (^{225}Ac-PSMA-617 vs. ^{177}Lu-PSMA-617) were 11,800-fold, 14,900-fold, and 4,200-fold for a single cell, 100 μm-radius micrometastasis, and macroscopic tumor, respectively.

Discussion

Dosimetry using imaging-based measurements of ^{225}Ac-PSMA-617 uptake is challenging due to the low administered activity and unfavorable physical decay characteristics of ^{225}Ac with low gamma emission probability and the competing Bremsstrahlung radiation (11). Therefore, previous dosimetry on ^{225}Ac-PSMA-617 and ^{225}Ac-PSMA-I&T extrapolated the uptake of respective ^{177}Lu-labeled analogs on imaging (11,12,22). Alternatively, extrapolation of ^{68}Ga-PSMA-617 uptake on positron emission tomography was previously used for dosimetry of ^{213}Bi-PSMA-617 (20). However, recent studies have shown that the degree of radiolabeled PSMA-617 uptake differs based on the radionuclide (23,24), which suggests that independent characterization of ^{225}Ac-PSMA-617 uptake will improve its dosimetry. At present, the only study that examined the tumor uptake of ^{225}Ac-PSMA-617 and ^{177}Lu-PSMA-617 is the pre-clinical study by Current et al. (21), where *ex vivo* activity measurements were used for accurate uptake estimation. The study was based on a mouse model without human validations, thus we considered the 3.4-fold higher ^{225}Ac-PSMA-617 uptake only as a possibility and interpreted the unscaled results as the lower bound of the relative efficacy of ^{225}Ac-PSMA-617.

Conventional organ-level dosimetry fails to take into consideration the subcellular distribution of the radiopharmaceutical even if accurate tumor uptake measurements could be obtained. It leads to radiation dose overestimation for an alpha emitter with cytoplasmic localization, such as ^{225}Ac-PSMA-617, and underestimation for an alpha emitter with nuclear localization. In addition, organ-level dosimetry cannot be applied to microscopic tumor deposits that are smaller than the range of alpha or beta particles. In contrast, the dosimetry model used in the present study incorporates the subcellular location of a radiopharmaceutical for accurate estimation of alpha and beta radiation dose at all tumor sizes of interest.

Two observations of interest were made in a macroscopic tumor. First, ^{225}Ac-PSMA-617 delivered at least 1,230-fold higher and possibly 4,200-fold higher equivalent dose per administered activity compared to ^{177}Lu-PSMA-617, which may explain the better efficacy of ^{225}Ac-PSMA-617 when 1,000-fold lower activity was administered in the clinical setting and even with subsequent de-escalation to 4 MBq doses (8,25). Second, conventional macroscopic dosimetry calculation resulted in no difference for ^{177}Lu-PSMA-617 and overestimation by 9% for ^{225}Ac-PSMA-617 compared to the subcellular dosimetry estimates of the radiation dose to the cell nuclei. The cross-fire effect of beta particles resulted in normalization of radiation dose within the tumor regardless of the subcellular source location for ^{177}Lu-PSMA-617, whereas the subcellular dose estimation for ^{225}Ac-PSMA-617 was slightly lower due to the absence of alpha emission from the cell nucleus. For both ^{225}Ac-PSMA-617 and ^{177}Lu-PSMA-617 therapy, conventional organ-level dosimetry yields acceptable dose estimates in measurable tumors.

In micrometastatic disease and circulating tumor cells, the alpha particles from ^{225}Ac-PSMA-617 were far more potent than beta particles from ^{177}Lu-PSMA-617, resulting in at least 3,000-4,000 times and possibly 10^4 times higher efficacy per administered activity. The findings are in keeping with the recognized advantage of alpha radiation in killing single cells and micrometastatic clusters (7). Therefore, at currently used doses, ^{225}Ac-PSMA-617 likely exerts a stronger cytotoxic effect on radiologically occult metastases, which will otherwise survive ^{177}Lu-PSMA-617 treatment due to insufficient cross-fire effect. While the therapeutic effect on micrometastatic disease may not produce a large decline in PSA, it potentially contributes

to the overall survival and progression-free survival benefits that are seen in ^{225}Ac-PSMA-617 therapy (8,9).

The calculated relative efficacy values can be applied to estimate the dose contribution from each radionuclide in the setting of tandem therapy with ^{225}Ac-PSMA-617/^{177}Lu-PSMA-617. For example, in a previously used treatment regimen that involves the median activities of 5.3 MBq ^{225}Ac-PSMA-617 and 6.9 GBq ^{177}Lu-PSMA-617, the dose contribution of ^{225}Ac-PSMA-617 relative to ^{177}Lu-PSMA-617 would be at least 94% for a macroscopic tumor. The contribution would increase to at least 270% and 330% for a single cell and micrometastatic cluster, respectively. The present study focused on radiolabeled PSMA-617 due to the larger body of available literature, but the results can be applied to dosimetry of PSMA-targeted radionuclide therapy using other molecules such as ^{225}Ac/^{177}Lu-PSMA-I&T.

The present study used physical dose estimates for comparison of theoretical efficacy, but its translation to clinical efficacy would be affected by differences in the radiobiological effects of alpha and beta particles. For example, untargeted effects, such as bystander or abscopal effect, may modify the dose-efficacy relationship by different degrees for alpha and beta particles (26). Direct DNA damage due to high-LET alpha particles does not require the presence of oxygen, whereas hypoxia has a high impact on low-LET radiation, which relies on reactive oxygen species formation for cytotoxicity (27,28). In addition, cytotoxicity due to high-LET radiation was previously shown to be independent of dose rate, likely due to the difficulty in repairing complex double-strand DNA breaks (29). Proliferating cells are more susceptible to ionizing radiation in general, but the cell cycle status of target cells affects the efficacy of low- and high-LET radiation to different extents (30). Beyond radiobiological considerations, increased tumor cell death may not necessarily produce a meaningfully better disease response or survival benefit on a patient level. Therefore, much remains to be known about the downstream consequences beyond radiation dose deposition in radionuclide therapy of prostate cancer.

Study Limitations

In addition to the difficulty in tumor ^{225}Ac-PSMA-617 uptake estimation, our study has several limitations. Mainly, the assumptions made in the simplified dosimetry model may be challenged. Intra-tumor heterogeneity in PSMA expression has been reported (31), and variable non-spherical shapes of prostate cancer cells were previously described (16). When ^{225}Ac decays before the internalization into endosomes, the daughter isotopes are no longer linked to PSMA-617 due to the recoil energy of alpha decay, which results in reduced dose deposition to the target cell (32). Radiation dose deposition outside the cell nucleus can also result in cytotoxicity by indirect effects (33). The RBE of 5 for alpha radiation is commonly employed (11,20) and is an oversimplification as discussed above, lacking validation in the setting of ^{225}Ac-based therapy in prostate cancer. Finally, the study does not address the toxicity that is associated with PSMA-targeted radionuclide therapy, which is not necessarily PSMA-mediated (34).

Conclusion

The equivalent radiation dose deposited by alpha-emitting ^{225}Ac-PSMA-617 is higher in measurable disease and especially higher in microscopic disease compared to beta-emitting ^{177}Lu-PSMA-617 at commonly administered doses based on subcellular dosimetry. Possible differences in tumor uptake based on the labeled radionuclide can lead to further amplification of the relative efficacy of ^{225}Ac-PSMA-617. Additional research is needed for tumor ^{225}Ac-PSMA-617 uptake characterization on both macroscopic and microscopic levels, as well as for an improved understanding of the biological effectiveness of alpha radiation in prostate cancer.

Ethics

Ethics Committee Approval: Not applicable.

Informed Consent: Not applicable.

Peer-review: Externally and internally peer-reviewed.

Financial Disclosure: The author declared that this study has received no financial support.

References

1. Mohler JL, Antonarakis ES, Armstrong AJ, D'Amico AV, Davis BJ, Dorff T, Eastham JA, Enke CA, Farrington TA, Higano CS, Horwitz EM, Hurwitz M, Ippolito JE, Kane CJ, Kuettel MR, Lang JM, McKenney J, Netto G, Penson DF, Plimack ER, Pow-Sang JM, Pugh TJ, Richey S, Roach M, Rosenfeld S, Schaeffer E, Shabsigh A, Small EJ, Spratt DE, Srinivas S, Tward J, Shead DA, Freedman-Cass DA. Prostate cancer, version 2.2019, NCCN clinical practice guidelines in oncology. J Natl Compr Canc Netw 2019;17:479-505.
2. Sadaghiani MS, Sheikhbahaei S, Werner RA, Pienta KJ, Pomper MG, Solnes LB, Gorin MA, Wang NY, Rowe SP. A systematic review and meta-analysis of the effectiveness and toxicities of lutetium-177-labeled Prostate-specific membrane antigen-targeted radioligand therapy in metastatic castration-resistant prostate cancer. Eur Urol 2021;80:82-94.
3. Hofman MS, Hicks RJ, Maurer T, Eiber M. Prostate-specific membrane antigen PET: clinical utility in prostate cancer, normal patterns, pearls, and pitfalls. Radiographics 2018;38:200-217.
4. Sartor O, de Bono J, Chi KN, Fizazi K, Herrmann K, Rahbar K, Tagawa ST, Nordquist LT, Vaishampayan N, El-Haddad G, Park CH, Beer TM, Armour A, Pérez-Contreras WJ, DeSilvio M, Kpamegan E, Gericke G, Messmann

RA, Morris MJ, Krause BJ. Lutetium-177-PSMA-617 for Metastatic Castration-Resistant Prostate Cancer. N Engl J Med 2021;385:1091-1103.

5. Hosono M, Ikebuchi H, Nakamura Y, Nakamura N, Yamada T, Yanagida S, Kitaoka A, Kojima K, Sugano H, Kinuya S, Inoue T, Hatazawa J. Manual on the proper use of lutetium-177-labeled somatostatin analogue (Lu-177-DOTA-TATE) injectable in radionuclide therapy (2nd ed.). Ann Nucl Med 2018;32:217-235.
6. Juzeniene A, Stenberg VY, Bruland ØS, Larsen RH. Preclinical and clinical status of PSMA-targeted alpha therapy for metastatic castration-resistant prostate cancer. Cancers (Basel) 2021;13:779.
7. Makvandi M, Lee H, Puentes LN, Reilly SW, Rathi KS, Weng CC, Chan HS, Hou C, Raman P, Martinez D, Xu K, Carlin SD, Greenberg RA, Pawel BR, Mach RH, Maris JM, Pryma DA. Targeting PARP-1 with alpha-particles is potently cytotoxic to human neuroblastoma in preclinical models. Mol Cancer Ther 2019;18:1195-1204.
8. Sathekge M, Bruchertseifer F, Vorster M, Lawal IO, Knoesen O, Mahapane J, Davis C, Reyneke F, Maes A, Kratochwil C, Lengana T, Giesel FL, Van de Wiele C, Morgenstern A. Predictors of overall and disease-free survival in metastatic castration-resistant prostate cancer patients receiving 225Ac-PSMA-617 radioligand therapy. J Nucl Med 2020;61:62-69.
9. Feuerecker B, Tauber R, Knorr K, Heck M, Beheshti A, Seidl C, Bruchertseifer F, Pickhard A, Gafita A, Kratochwil C, Retz M, Gschwend JE, Weber WA, D'Alessandria C, Morgenstern A, Eiber M. Activity and adverse events of actinium-225-PSMA-617 in advanced metastatic castration-resistant prostate cancer after failure of lutetium-177-PSMA. Eur Urol 2021;79:343-350.
10. von Eyben FE, Roviello G, Kiljunen T, Uprimny C, Virgolini I, Kairemo K, Joensuu T. Third-line treatment and 177Lu-PSMA radioligand therapy of metastatic castration-resistant prostate cancer: a systematic review. Eur J Nucl Med Mol Imaging 2018;45:496-508.
11. Kratochwil C, Bruchertseifer F, Rathke H, Bronzel M, Apostolidis C, Weichert W, Haberkorn U, Giesel FL, Morgenstern A. Targeted α-therapy of metastatic castration-resistant prostate cancer with 225Ac-PSMA-617: dosimetry estimate and empiric dose finding. J Nucl Med 2017;58:1624-1631.
12. Belli ML, Sarnelli A, Mezzenga E, Cesarini F, Caroli P, Di Iorio V, Strigari L, Cremonesi M, Romeo A, Nicolini S, Matteucci F, Severi S, Paganelli G. Targeted alpha therapy in mCRPC (metastatic castration-resistant prostate cancer) patients: predictive dosimetry and toxicity modeling of 225Ac-PSMA (prostate-specific membrane antigen). Front Oncol 2020;10:531660.
13. Kratochwil C, Bruchertseifer F, Giesel FL, Weis M, Verburg FA, Mottaghy F, Kopka K, Apostolidis C, Haberkorn U, Morgenstern A. 225Ac-PSMA-617 for PSMA-targeted α-radiation therapy of metastatic castration-resistant prostate cancer. J Nucl Med 2016;57:1941-1944.
14. Bavelaar BM, Lee BQ, Gill MR, Falzone N, Vallis KA. Subcellular targeting of theranostic radionuclides. Front Pharmacol 2018;9:996.
15. Vaziri B, Wu H, Dhawan AP, Du P, Howell RW; SNMMI MIRD Committee. MIRD pamphlet No. 25: MIRDcell V2.0 software tool for dosimetric analysis of biologic response of multicellular populations. J Nucl Med 2014;55:1557-1564.
16. Park S, Ang RR, Duffy SP, Bazov J, Chi KN, Black PC, Ma H. Morphological differences between circulating tumor cells from prostate cancer patients and cultured prostate cancer cells. PLoS One 2014;9:e85264.
17. Lee H, Riad A, Martorano P, Mansfield A, Samanta M, Batra V, Mach RH, Maris JM, Pryma DA, Makvandi M. PARP-1-targeted auger emitters display high-LET cytotoxic properties in vitro but show limited therapeutic utility in solid tumor models of human neuroblastoma. J Nucl Med 2020;61:850-856.
18. Wiley JD, Seman JA. The enumeration of neighbors on cubic and hexagonal-based lattices. Bell Syst Tech J 1970;49:355-378.
19. Eckerman K, Endo A. MIRD: radionuclide data and decay schemes 2nd edn (Reston, VA: Society for Nuclear Medicine). Published online 2008.
20. Kratochwil C, Schmidt K, Afshar-Oromieh A, Bruchertseifer F, Rathke H, Morgenstern A, Haberkorn U, Giesel FL. Targeted alpha therapy of mCRPC: dosimetry estimate of (213)Bismuth-PSMA-617. Eur J Nucl Med Mol Imaging 2018;45:31-37.
21. Current K, Meyer C, Magyar CE, Mona CE, Almajano J, Slavik R, Stuparu AD, Cheng C, Dawson DW, Radu CG, Czernin J, Lueckerath K. Investigating PSMA-targeted radioligand therapy efficacy as a function of cellular PSMA levels and intratumoral PSMA heterogeneity. Clin Cancer Res 2020;26:2946-2955.
22. Gosewisch A, Schleske M, Gildehaus FJ, Berg I, Kaiser L, Brosch J, Bartenstein P, Todica A, Ilhan H, Böning G. Image-based dosimetry for (225)Ac-PSMA-I&T therapy using quantitative SPECT. Eur J Nucl Med Mol Imaging 2021;48:1260-1261.
23. Sinnes JP, Bauder-Wüst U, Schäfer M, Moon ES, Kopka K, Rösch F. (68)Ga, (44)Sc and (177)Lu-labeled AAZTA(5)-PSMA-617: synthesis, radiolabeling, stability and cell binding compared to DOTA-PSMA-617 analogues. EJNMMI Radiopharm Chem 2020;5:28.
24. Umbricht CA, Benešová M, Schmid RM, Türler A, Schibli R, van der Meulen NP, Müller C. (44)Sc-PSMA-617 for radiotheragnostics in tandem with (177)Lu-PSMA-617-preclinical investigations in comparison with (68)Ga-PSMA-11 and (68)Ga-PSMA-617. EJNMMI Res 2017;7:9.
25. Sathekge M, Bruchertseifer F, Knoesen O, Reyneke F, Lawal I, Lengana T, Davis C, Mahapane J, Corbett C, Vorster M, Morgenstern A. (225)Ac-PSMA-617 in chemotherapy-naive patients with advanced prostate cancer: a pilot study. Eur J Nucl Med Mol Imaging 2019;46:129-138.
26. Boyd M, Ross SC, Dorrens J, Fullerton NE, Tan KW, Zalutsky MR, Mairs RJ. Radiation-induced biologic bystander effect elicited in vitro by targeted radiopharmaceuticals labeled with alpha-, beta-, and auger electron-emitting radionuclides. J Nucl Med 2006;47:1007-1015.
27. Barendsen GW, Koot CJ, Van Kersen GR, Bewley DK, Field SB, Parnell CJ. The effect of oxygen on impairment of the proliferative capacity of human cells in culture by ionizing radiations of different LET. Int J Radiat Biol Relat Stud Phys Chem Med 1966;10:317-327.
28. Wenzl T, Wilkens JJ. Theoretical analysis of the dose dependence of the oxygen enhancement ratio and its relevance for clinical applications. Radiat Oncol 2011;6:171.
29. Wozny AS, Alphonse G, Battiston-Montagne P, Simonet S, Poncet D, Testa E, Guy JB, Rancoule C, Magné N, Beuve M, Rodriguez-Lafrasse C. Influence of dose rate on the cellular response to low- and High-LET radiations. Front Oncol 2016;6:58.
30. Lyckesvärd MN, Delle U, Kahu H, Lindegren S, Jensen H, Bäck T, Swanpalmer J, Elmroth K. Alpha particle induced DNA damage and repair in normal cultured thyrocytes of different proliferation status. Mutat Res 2014;765:48-56.
31. Brady L, Kriner M, Coleman I, Morrissey C, Roudier M, True LD, Gulati R, Plymate SR, Zhou Z, Birditt B, Meredith R, Geiss G, Hoang M, Beechem J, Nelson PS. Inter- and intra-tumor heterogeneity of metastatic prostate cancer determined by digital spatial gene expression profiling. Nat Commun 2021;12:1426.
32. Kruijff RM, Raavé R, Kip A, Molkenboer-Kuenen J, Morgenstern A, Bruchertseifer F, Heskamp S, Denkova AG. The in vivo fate of (225)Ac daughter nuclides using polymersomes as a model carrier. Sci Rep 2019;9:11671.
33. Ku A, Facca VJ, Cai Z, Reilly RM. Auger electrons for cancer therapy - a review. EJNMMI Radiopharm Chem 2019;4:27.
34. Rupp NJ, Umbricht CA, Pizzuto DA, Lenggenhager D, Töpfer A, Müller J, Muehlematter UJ, Ferraro DA, Messerli M, Morand GB, Huber GF, Eberli D, Schibli R, Müller C, Burger IA. First clinicopathologic evidence of a non-PSMA-related uptake mechanism for (68)Ga-PSMA-11 in salivary Glands. J Nucl Med 2019;60:1270-1276.

Original Article
Mol Imaging Radionucl Ther 2022;31:7-15 DOI:10.4274/mirt.galenos.2021.17363

Deconvolution of Tc-99m-Mercaptoacetyltriglycine Renograms with the Concomitant Use of a Sparse Legendre Polynomial Representation and the Moore-Penrose Pseudo-inverse

Tc-99m-Merkaptoasetiltriglisin Renogramlarının Seyrek Legendre Polinom Gösterimi ve Psödo-İnvers Moore-Penrose Yöntemlerinin Birlikte Kullanılmasıyla Dekonvolüsyonu

Michel Destine[1], *François-Xavier Hanin*[1], *Isabelle Mathieu*[1], *Bernard Willemart*[1], *Alain Seret*[2]

[1]*CHU UCLouvain Namur Hospital, Department of Nuclear Medicine, Namur, Belgium*
[2]*GIGA Cyclotron Research Centre, University of Liège, Liège, Belgium*

Abstract

Objectives: This study aimed to introduce an improved deconvolution technique for Tc-99m-mercaptoacetyltriglycine renograms based on the combination of a sparse Legendre polynomial representation and the Moore-Penrose inversion matrix (LG). This method reduces the effect of noise on the measurement of renal retention function transit time (TT).

Methods: The stability and accuracy of the proposed method were tested using a renal database containing Monte Carlo-simulated studies and real adult patient data. Two clinical parameters, namely, split function (SF) and mean TT (meanTT), obtained with LG were compared with values calculated with the established method that combines matrix deconvolution and a three-point linear smoothing (F121) as recommended by the 2008 International Scientific Committee of Radionuclides in Nephrourology consensus on renal TT measurements.

Results: For simulated data, the root mean square error (RMSE) between the theoretical non-noisy renal retention curve (RRC) and the results of the deconvolution methods applied to the noisy RRC were up to two times lower with LG ($p<0.001$). The RMSE of the reconvoluted renogram and the theoretical one was also lower for LG ($p<0.001$) and showed better preservation of the original signal. The SF was neither improved nor degraded by the proposed method. For patient data, no statistically significant difference was found between the SF for the LG method compared with the database values, and the meanTT better agreed with the physician's diagnosis than the matrix or clinical software (Hermes) outputs. A visual improvement of the RRC was also observed.

Conclusion: By combining the sparse Legendre representation of the renogram curves and the Moore-Penrose matrix inverse techniques, we obtained improved noise reduction in the deconvoluted data, leading to better elimination of non-physiological signals -as negative values- and the avoidance of the smear effect of conventional smoothing on the vascular peak, which both influenced the meanTT measurement.

Keywords: MAG3, Legendre polynomials, Moore-Penrose, deconvolution, renal transit time, denoising

Öz

Amaç: Bu çalışma, seyrek Legendre polinom gösterimi ve Moore-Penrose inversiyon matrisinin (LG) kombinasyonuna dayanan Tc-99m merkaptoasetiltriglisin renogramları için geliştirilmiş bir dekonvolüsyon tekniğini tanıtmayı amaçlamaktadır. Bu yöntem, gürültünün renal retansiyon fonksiyonu geçiş süresinin (TT) ölçümü üzerindeki etkisini azaltır.

Yöntem: LG ile elde edilen iki klinik parametre olan bölünmüş fonksiyon (SF) ve ortalama TT (ortalamaTT), 2008'de renal TT ölçümleri üzerine Uluslararası Nefroüroloji Radyonüklidleri Bilimsel Komitesi'nin ortak görüşünde önerilen matriks dekonvolüsyonu ve 3-noktalı doğrusal yumuşatmayı (F121) birleştiren yerleşik yöntemle karşılaştırıldı.

Address for Correspondence: Michel Destine MSc, CHU UCLouvain Namur Hospital, Department of Nuclear Medicine, Namur, Belgium
Phone: +3281720544 **E-mail:** michel.destine@uclouvain.be ORCID ID: orcid.org/0000-0002-0594-7741
Received: 08.03.2021 **Accepted:** 19.07.2021

Bulgular: Simüle edilmiş veriler için, teorik gürültülü olmayan renal retansiyon eğrisi (RRC) ile gürültülü RRC'ye uygulanan dekonvolüsyon yöntemlerinin sonuçları arasındaki kök ortalama kare hatası (RMSE) LG ile iki kat daha düşüktü (p<0,001). Kıvrımlı renogramın ve teorik renogramın RMSE'si de LG için daha düşüktü (p<0,001) ve orijinal sinyalin daha iyi korunduğunu gösterdi. Bölme işlevi (SF), önerilen yöntemle ne iyileştirildi ne de bozuldu. Hasta verileri için, LG yöntemi için SF ile veri tabanı değerlerine kıyasla anlamlı bir fark bulunmadı ve ortalamaTT, doktorun teşhisi ile matris veya klinik yazılım (Hermes) çıktılarından daha uyumluydu. RRC'de görsel bir iyileşme de gözlendi.

Sonuç: Renogram eğrilerinin seyrek Legendre gösterimi ve Moore-Penrose matrisi ters tekniklerini birleştirerek dekonvolüsyon verilerinde daha iyi bir gürültü azaltımı elde edilmiş ve bu da fizyolojik olmayan sinyallerin -negatif değerler olarak- daha başarılı bir şekilde yok edilmesine ve vasküler tepe üzerindeki alışılagelmiş yumuşatmanın yayma etkisinin önlenmesine yol açarak ortalamaTT ölçümünü etkilemiştir.

Anahtar kelimeler: MAG3, Legendre polinomları, Moore-Penrose, dekonvolüsyon, renal geçiş süresi, gürültü giderme

Introduction

Deconvolution methods were initially applied in the early 1940s (1) to blood flow measurements and later to gastroenterology kinetic tracers (2). The first quantitative renogram analysis by deconvolution was proposed in the early 1970s (3). Various renography tracers have been developed since then. Tc-99m-mercaptoacetyltriglycine (MAG3), which is the focus of present research, has become the radiopharmaceutical of choice in various clinical contexts (4) and has been routinely used for years. Furthermore, increased interest in renography is expected following the recent development of novel PET radiotracers (5) that open the door to three-dimensional renography, while scintigraphy remains limited to two-dimensional renograms.

Deconvolution is a mathematical process that can be viewed as an imitation of the renal retention curve (RRC), which could be obtained if the radiotracer activity was instantly and directly injected into the renal artery. The RRC provides information about the quantity of radiotracer retained in the kidney over time. It is possible to extract information that relates to the spread of tubular transit times (TTs) and has physiological significance. For example, urinary tract obstruction can lengthen the TT of the radiotracer through the kidney. The renal system can be described as a series of pathways with different lengths and therefore with different TTs. The parameters with the highest clinical relevance are the mean TT (meanTT) and the left-to-right ratio or split function (SF). SF has been proven (6) to be proportional to the plateau height of the individual RRC. After removing the early vascular phase by back extrapolation of the plateau, the meanTT is computed as the integral of the RRC divided by the plateau height. For MAG3, typical normal values ranged from 2 to 4 min for the whole kidney meanTT (4,7) and are between 45% and 55% for SF.

Mathematically, deconvolution can be seen as the solution of the integral equation:

$$R(t)= \int_0^t H(t-\tau)*B(\tau)d\,\tau \qquad (1)$$

where R (t) is the renogram obtained in the clinical routine, B (t) the input function (blood input), and H (t) the unknown RRC. Different methods have been intensively investigated to solve this equation, such as Laplace transform, matrix systems or constrained least square in the time domain and fourier deconvolution in the frequency domain (7). A study revealed that these deconvolution techniques performed differently in clinical cases (7). For example, the constrained least square was more reliable in assessing the meanTT in the presence of very noisy data. Conversely, the matrix method performs better when noise is very low (7).

Unfortunately, the deconvolution process is one of the mathematical inverse problems that are classified as ill-posed. This means that small errors or variations in the input data lead to large errors in the output, i.e., the deconvoluted curve. On some occasions, the process can lead to a solution RRC, which has no clinical meaning, while the RRC that is reconvoluted with the input function still gives the correct initial renogram. None of the previously mentioned deconvolution methods are exempted to this problem. Moreover, they are all very sensitive to small variations in the inputs, renogram, and blood input curve and are therefore very sensitive to data noise. For the matrix method, which is the most frequently implemented method, the initial signal value is crucial. This value determines not only whether the matrix can be inverted, but any slight change or error in this value will propagate throughout the deconvolution process (7).

Given the presence of a high level of noise in the majority of scintigraphy data, it is not possible to obtain an RRC by deconvolution without a reduction in these statistical fluctuations. Without appropriate noise reduction, large oscillations are often present in the solution, sometimes with negative values that have no physiological meaning. Simple filtering of the input data, a common method of noise reduction, is not very effective. Excessive filtering may modify the characteristics of the underlying physiological

information present in the curves. On the contrary, applying a minimum filtering value will still result in an unstable and inaccurate output. Previous studies have shown that the accuracy of the RRC depends not only on the degree but also on the type of filtering (8). Moreover, filtering must be applied before (and sometimes also on) the output of the deconvolution process, mainly to remove negative values. The RRC contains a mix of renal and non-renal phases. It follows the idea that the initial shape of the RRC should be cautiously considered since the first time points (vascular stage) are higher than those that follow. One of the drawbacks of excessive filtering is a spread of the vascular component in addition to a greater difficulty in determining the end of the RRC plateau. A general conclusion from the literature, as summarized in the ISCORN consensus (4,7), is that linear filtering with a 1-2-1 kernel and with a variable number of passes, as proposed by Fleming (9,10), is the recommended option.

This study was conducted to determine whether sparse Legendre polynomials (LP) can be used to create a representation of time-activity curves (TACs) as a Poisson noise removal tool, as was recently shown to be effective for standard renography processing (11), which in combination with an adapted deconvolution technique could be suitable for improving nuclear renogram analysis by deconvolution in routine practice.

Materials and Methods

Representation of LP and the Pseudo-inverse Method

This study relied on the representation of a noisy TAC by sparse Legendre expansion (11,12). The description of the noisy TAC f (t) can be written as a limited sequence of the LP of K_{max} +1 terms giving a denoized curve f_L(t):

$$f_L(t) = \sum_{k=0}^{Kmax} L(k)\, P_k(t) \qquad (2)$$

where P_k(t) is the LP of order k and the Legendre coefficients L (k) are computed from:

$$L(k) = \frac{2k+1}{N} \sum_{t=-1}^{t=1} f(t)\, P_k(t) \qquad (3)$$

The $\frac{2k+1}{N}$ term is a normalization factor linked to the LP.

As the tracer is injected into the blood, the renogram function R (t) (which is the TAC of the kidney obtained from scintigraphy images) is the mathematical convolution of the plasma or impulse function B (t) and the kidney impulse response function H (t). The relationship between these functions is given by the following equation:

$$R(t) = H(t) \circ B(t) \qquad (4)$$

where o denotes the convolution operator. This process is schematically represented in Figure 1. B (t) is usually

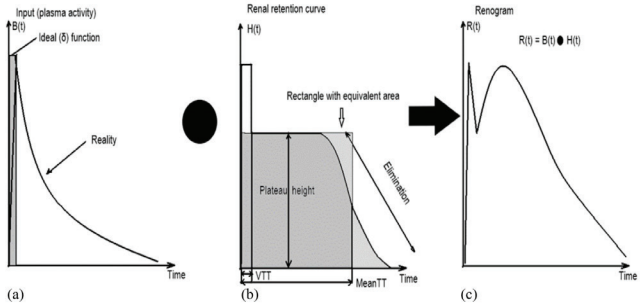

Figure 1. Schematic representation of the convolution process. (a) The impulse function is represented as an ideal (δ) or intra-arterial injection (gray) and as a real plasma curve and (b) is the unknown response function of the kidney or renal retention function with relevant kidney dynamic parameters. The meanTT may be calculated by integrating the area under the H (t) divided by the plateau height. This is related to the equivalent area (light gray) and (c) represents the convolution product of H (t) and B (t) in a real case with an overemphasis of the plasma peak
meanTT: Mean transit time

obtained from a region of interest (ROI) over the heart. H (t) describes the TAC that would be obtained if the tracer was injected in bolus (δ mathematical function) directly into the kidney artery and is also called the impulse response function. H (t) does not depend on the shape of the blood input function and truly characterizes the fundamental behavior of the kidney.

In the first step, we applied the finite Legendre transform to the raw blood input B (t) and renogram R (t) curves to perform noise removal.

$$B(t) = \sum_{j=0}^{KBmax} L_j^B P_j^B \qquad (5)$$

$$B(t) = \sum_{\iota=0}^{KRmax} L_\iota^R P_\iota^R \qquad (6)$$

where L_j^B and L_ι^R are component vectors of dimension j and ι and KB_{max}, KR_{max} are the individual number of Legendre coefficients for each curve. P_j^B and P_ι^R are LP components of a $P^B \in \mathbb{R}^{j \times m}$ and a $P^R \in \mathbb{R}^{J \times m}$ matrix, respectively, where m had the dimension of the number of time points in the renogram.

In a second step, the unknown function H (t) was also developed as a Legendre expansion:

$$H(t) = \sum_{i=0}^{q} L_i^H P_i^H \qquad (7)$$

where the P_i^H are the LPs of a $P^H \in \mathbb{R}^{q \times m}$ matrix and L_i^H are the unknown Legendre coefficients of the renal retention function of dimension q. In our previous publication (11), the maximum number of Legendre coefficients for L_i^B and L_ι^R was $2*\sqrt{m}$. Here, we found the limit for q to be $4*\sqrt{m}$.

Substituting equation (7) in (4) gave the following equation:

$$R(t) = \left(\sum_{i=0}^{q} L_i^H P_i^H\right) \circ B(t) \qquad (8)$$

Convolution of B (t) with the P_i^H gave the matrix equation:

$$R(t) = (P_B^T(t))\, L \qquad (9)$$

where (P_B^T (t)) is the transposed convoluted matrix and L contains the unknown coefficients of the RRC.

To solve this system, we needed the inverse of the non-square matrix P_B^T (t). This was performed using the Moore-Penrose inverse. This generalized inverse is calculated using its singular-value decomposition and is noted (P_B^{T+}). The solution of equation (7) was obtained by the calculation of the Legendre coefficient vector L'.

$$L' = (P_B^{T+}(t))R(t) \quad (10)$$

L' could be different from L due to the Moore-Penrose inversion process, which acts as a least square minimizer (13).

From the L', we obtained the filtered response function H' (t) as a sparse Legendre expansion with q terms:

$$H' = \sum_{i=1}^{q} L_i' P_i^H(t) \quad (11)$$

Kidney Database

For this study, we used a freely accessible online kidney database (www.dynamicrenalstudy.org) that contains Monte Carlo (MC) (14)-simulated studies and real adult patient data. The pharmacokinetics of the MC database is driven by a multi-compartmental model for Tc-99m-MAG3 and based on the first-order differential equation:

$$\frac{dC_i(t)}{dt} = \frac{1}{v_i}\sum_{j=1}^{N}(r_{j\to i}\, C_j(t) - r_{i\to j} C_i(t)) \quad (12)$$

where $C_i(t)$ is the tracer concentration in compartment i at time t, V_i the volume of the ith compartment, and $r_{j\to i}$ the transfer rate constant from compartment *j* to *i*. The simulation incorporated up to 69 phantom structures to provide a realistic patient representation in terms of anatomical and pharmacokinetic characteristics. The renal cortex and medulla were modeled by delay functions to generate time distributions close to real patient TTs. The MC dataset comprised six studies based on the same phantom with two clearances and a total of 30 simulations. Each study represented a specific SF, and simulations were available for two levels of simulated injected activity (50 and 100 MBq), anterior and posterior views, and a reference study (RS) posterior view. RS was a simulation without any physical image-degrading effect such as noise, tissue background, attenuation, and scattering in both phantom and camera, giving the actual time variant tracer distribution (ground truth). Each study was based on the characteristics of its RS, and a difference in the kidney-to-skin distance was taken into account. Each simulated dataset consisted of a dynamic renogram acquisition of 120 frames of 10 s and 128×128 pixels. A summary of the MC study characteristics is presented in Table 1. For each study, we extracted the RRC from the RS to obtain a perfect theoretical noise-free shaped retention curve. The noise-free RCC and input function (B) from an ROI over the heart of the RS were convoluted to obtain the theoretical renogram (R).

Renogram Processing

Original ROIs were drawn on studies with the Hermes renogram analysis (Hermes Medical Solutions AB, Stockholm Sweden) and were copied onto our software (11). The kidney background ROIs were drawn from the lateral direction, going from the lower to the upper pole to avoid the pelvi-ureteric activity. An ROI was drawn over the left ventricle to obtain the input function and another between the heart and kidneys for input function background subtraction.

For the LG and matrix deconvolution (15), we always applied the same method for the starting point of the input curve and the determination of the plateau of the RRC. The input curve peak time was taken as the zero time (7). The plateau of the retention function was calculated from the mean value (P_{Mean}) of the RRC curve between 1.2 and 2.0 min. This PMean replaced all the values from zero to the time point where the RRC fell below 85% of the PMean (16).

For the matrix method and theoretical data, we combined pre- and post-filtration (MPPF) using the F121 with a progressively rising number of passes up to 12 for pre-filtering to cover the range of passes determined by Fleming's formula (9,10). Post-filtering was applied up to six passes, for each pre-filtering value, starting at the third point of the deconvoluted curve to avoid the influence of the vascular part. For the simulated data, we only considered F121 pre-filtering using the number of passes as determined by Fleming's formula and an F121 post-filtering with one pass, again excluding the first three points. This method is denoted MFF. The blood input function was

Table 1. Summary of the characteristics of the Monte Carlo-simulated studies for the LRF and clearance. Each study contains five series with one reference study in posterior, two posterior, and anterior with 100 MBq or 50 MBq of injected activity

Study	LRF (%)	Clearance (mL/min)
1	50	260
2	20	
3	70	
4	50	130
5	20	
6	70	

LRF: Left relative function

filtered by F121 with a variable number of passes.

We applied the LP on the input function and on the noisy renogram before LG. We used a method based on an autocorrelation of the Legendre coefficients (11) to determine the optimum number of coefficients to be used. We also varied the number of Legendre coefficients to check if there was no other best solution.

For the first part of this study, the theoretical renogram R and input function B were added with different Poisson noise realizations to obtain noisy curves R' and B'. Using R' and B', the two deconvolution processes (LG and Matrix) were applied to obtain RRC'. In the first step, to obtain a global estimate of the accuracy of the deconvolution methods, the root mean square error (RMSE) between the results of the two deconvolution processes (matrix and LG) on the noisy curves RRC' and the theoretical RRC was calculated. A convolution of the computed RRC' with the filtered input function was used to calculate the RMSE with the theoretical noise-free renogram R to assess the preservation of the original signal. In a second step, the SF and whole kidney meanTT were computed from the RRC' obtained by both deconvolution methods.

The second part of the study used the MC-simulated studies with the presence of all physical-degrading effects and with respect to the different noise levels. The SF and TTs obtained from the RRC with both deconvolution methods were compared. Thus, it was not possible to determine the best F121, and only Fleming's formula was used with one F121 post-filtration (MFF).

The last part of this study was the confrontation of the outputs of the two deconvolution methods (LG and MFF), to which we added the outputs of the Hermes kidney analysis clinical software, applied to 31 patient studies from the database. These studies consist of MAG3 renograms recorded in a single acquisition (30 min) of 180 frames of 10 s in 128×128 pixels. The selection of 31 studies from the database was based on the clinical diagnostics and aimed to have a ratio close to 50% between normal and pathological kidneys. The clinical data, SF, and diagnosis were available from the database. The SF provided in the database was compared with the values obtained with the deconvolution and analysis methods used in this work. Three specialists for nuclear medicine (BW, IM, and FH) performed a blind test analysis of the patient studies with the Hermes renogram analysis program to establish if the whole kidney meanTT was pathological or not, and the results were compared with the outputs of the LG method and MFF to determine if a correlation exists between the clinical diagnostic and calculated meanTT. A bias was noted in the Hermes results of the meanTT that was discovered at the beginning of the study with the help of the MC-simulated studies. It was confirmed by the Hermes support team that the system starts the analysis at 20 s. Moreover, the Hermes software does pre- and post-linear filtering (F121) and an apodization of the results to avoid negative values. Other details of the matrix deconvolution process in Hermes were unavailable. The determination of the plateau was computed in Hermes using the first and second derivatives. While the 20-s difference for the starting point is not significant for diagnosis, it has an influence on the matrix deconvolution output. For patient data, we considered this difference when classifying the kidney TT as pathological or normal. This feature of the Hermes software was part of the motivation for developing our own matrix deconvolution software.

CHU UCLouvain Namur Site De Sainte-Elisabeth Hospital Ethics Comitte approval (number: 08/21) was obtained, and the requirement to obtain informed consent was waived for this study because of its retrospective design.

Statistical Analysis

Data were divided into three subsets (RS, noisy MC, real patient data), and two parameters were analyzed (SF and whole kidney meanTT). The RMSE was used to measure the deviation between observed and theoretical values. The mean and standard deviation (SD) were used to describe the spread of measurements. The slope, intercept, and coefficient of determination were obtained from linear regression for a pairwise comparison of the outcomes of the processing methods. A Bland-Altman plot was used to compare pairwise methods, including the 95% confidence interval for the limits of agreement. Statistical t-tests were performed at a 5% level of significance ($p<0.05$) using XLStat (version 2019.1.3, France).

Results

Theoretical Renogram and Input Function Added with Poisson Noise

Considering the matrix-deconvoluted theoretical noisy RRC', the composite number of pre- and post-filtering passes for F121 that led to the lowest RMSE between the deconvoluted RRC' and the non-noisy theoretical RRC was considered optimal. This was consistent with previous findings (8). This optimal composite number of pre- and post-filtering F121 passes was selected for all further comparison with the LG method. The RMSE between theoretical and computed values for the retention function and renogram curves are presented in Table 2. The LG method showed an RMSE up to two times lower than the MPPF for the RRC' ($p<0.001$). In addition, the

reconvolution error was the lowest for LG (p=0.001). The MFF was slightly worse in both cases but nevertheless close to the lowest MPPF RMSE. The better performance of the LG can be visualized in Figure 2a, where the MPPF method still had ripples and negative values, which have no physiological interpretation. The LG method preserved most of the original RRC. In particular, the vascular peak and subsequent points were smeared out when MPPF was applied, a phenomenon that gradually was increasingly present as the number of F121 passes increased in pre-filtering (Figure 2b).

For the simulated data, SF values are given in the database, and the meanTT was computed from non-noisy RRC by Riemann integration of the curve. An excellent agreement was noted between the database SF values, and the results computed from the three methods (Table 3) with no significant difference (p>0.30).

The meanTT calculated from the non-noisy RRC curves and the results from the RRC' obtained with LG and the matrix method -with MPPF or MFF- were compared using Bland-Altman plots (Figure 3a, b, c). LG resulted in a bias closest to zero and the smallest SD, while the MPPF with the lowest RMSE and the MFF performed very similarly.

Table 2. RMSE between the theoretical RRC and deconvoluted noisy RRC' and RMSE between the theoretical renogram R and reconvoluted renogram R' from RRC'

	Theory RRC-RRC'		Theory R-R'	
Method	**RMSE**	**SD**	**RMSE**	**SD**
LG	0.0017	0.0008	32.23	11.66
MPPF	0.0030	0.0008	41.55	10.63
MFF	0.0036	0.0011	43.77	11.60

RMSE: Root mean square error, RRC: Renal retention curve, LG: Legendre generalized, MPPF: Matrix pre and post filtering, MFF: Matrix Flemings' filtering, SD: Standard deviation

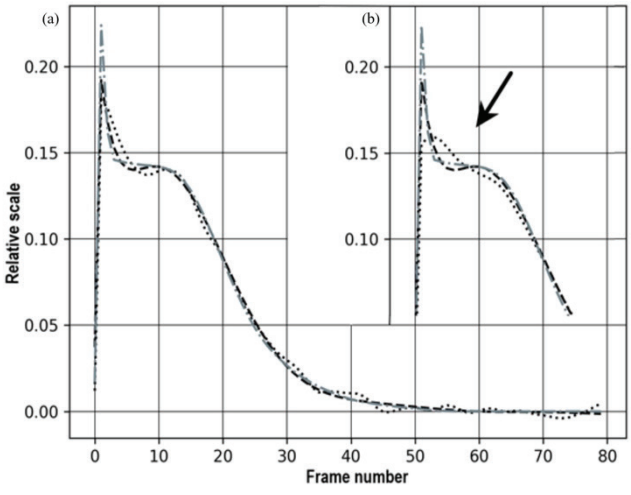

Figure 2. (a) Comparison between the theoretical (light gray dotted dashed line) non-noisy RRC, the matrix MPPF (dotted line) with three passes for pre-filtering and one post-filtering, and LG (dashed line) deconvolution of the corresponding noisy renogram. (b) Increasing the number of smooths for MPPF (six passes for pre-filtering and one for post-filtering) smeared out the vascular peak

RRC: Renal retention curve, LG: Legendre generalized, MPPF: Matrix pre and post filtering

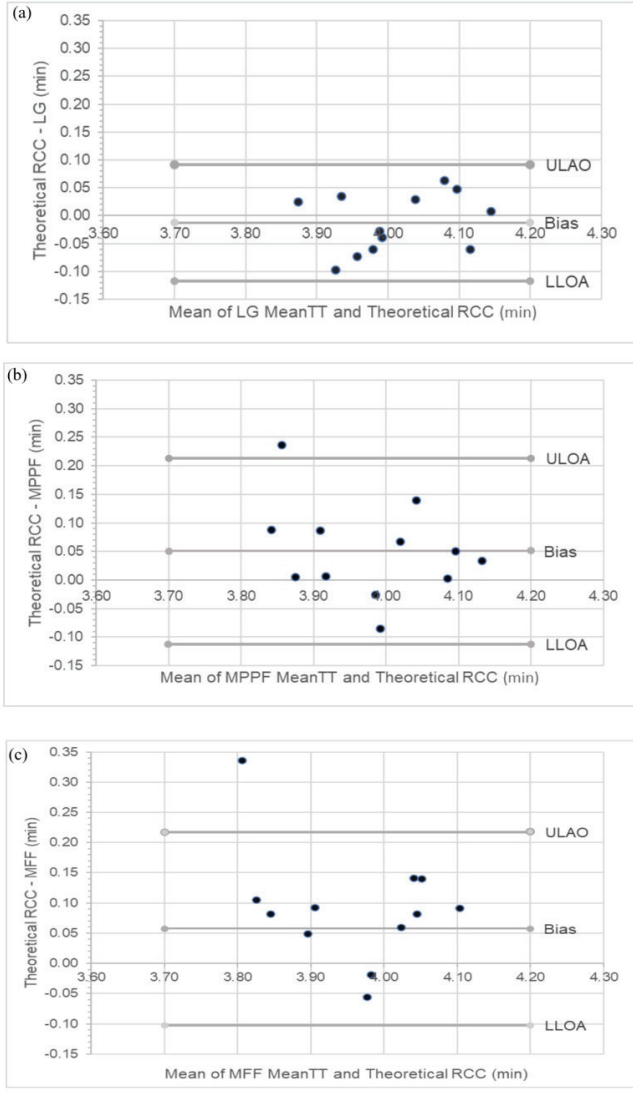

Figure 3. Bland-Altman plot agreement between the meanTT obtained on RS without noise and RS with Poisson noise added for (a) LG, (b) MPPF with lowest RMSE, and (c) MFF. U and LLOA show two SD

meanTT: Mean transit time, RS: Reference study, LG: Legendre generalized, MPPF: Matrix pre and post filtering, RMSE: Root mean square error, MFF: Matrix Flemings' filtering, U: Upper, LLOA: Lower levels of agreement, SD: Standard deviation

MC-simulated Studies

For the MC-simulated studies, we only considered the MFF for the matrix deconvolution. For each study, the simulated data were created with the same kinetic parameters (SF and meanTT) based on their respective RS. For the SF, we did not find any significant difference in the mean between the LG and MFF methods when compared with the expected values (p=0.63). The average value of the meanTT extracted from the RS used as reference was 4.0 min for the left kidney and 3.9 min for the right kidney. When comparing the mean of the meanTT for all posterior studies and all anterior studies (Table 4), a difference was observed between the two methods. This is illustrated in Figure 4a, b. LG was always higher and closer to the expected meanTT value than MFF. Considering the same view and same kidney, the value dispersion was also reduced with LG. In Figure 4, the posterior and anterior studies were separated to take into account the difference in the patient configuration, in the background subtraction for the kidney and the input function, and to highlight the signal-to-noise ratio worsening in anterior images.

Table 3. Summary statistics of linear regression on noisy reference study for the split function

Method	Slope	R^2	Intercept (%)
LG	1.00	0.99	0.002
MPPF	0.981	0.99	0.008
MFF	0.961	0.99	0.02

LG: Legendre generalized, MPPF: Matrix pre and post filtering, MFF: Matrix Flemings' filtering

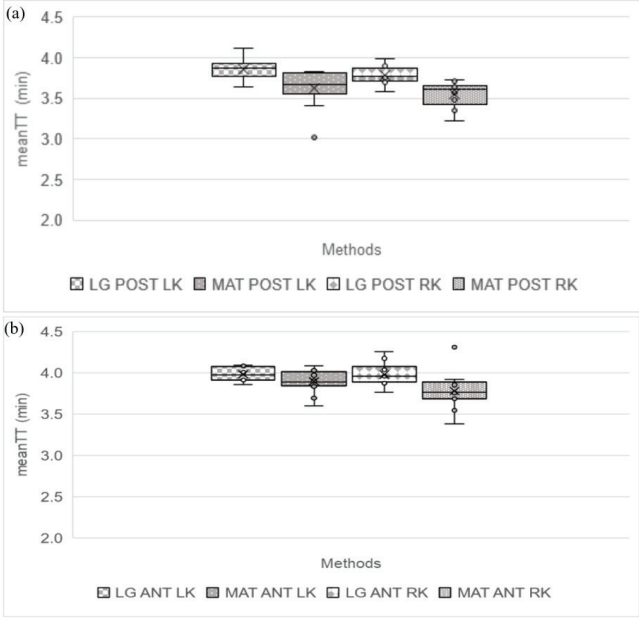

Figure 4. Box plot of the meanTT with the LG and MFF methods for (a) posterior and (b) anterior left (LK) and right (RK) kidney MC-simulated data

meanTT: Mean transit time, LG: Legendre generalized, MFF: Matrix Flemings' filtering

Patient Studies

For the SF, no significant difference was found between LG and the database values (p=0.48). A comparison of the whole kidney meanTT was performed between the Hermes clinical software, LG, and MFF (Figure 5a, b, c). A general good agreement was noted in the normal range of meanTT (3.5±1 min for hydrated patients following ISCORN), while discrepancies between methods were more frequently observed for kidneys with meanTT outside this normal range. A systematic bias was observed between LG and Hermes (bias: 1.1, SD: 1.4). The LG meanTT values were higher than that in Hermes (p<0.001). The same trend was observed between MFF and Hermes (bias: 0.6, SD: 1.1, p<0.0001). The difference between LG and MFF was less marked (bias: 0.1, SD: 0.7, p=0.18).

The blind test realized by the three physicians gave a discordant diagnosis on 4 of 62 kidneys for the determination of an abnormal TT. The discordance appeared for patients with results in the "gray zone" where the final diagnosis remains physician dependent (17). For the remaining 58 kidneys, we obtained discrepancies for only 10.3% with LG, 12.1% with MFF, but 24.1% with the Hermes system between diagnosis based on prolongated TT values and physician diagnosis.

Discussion

A common result for all the data -theoretical, MC-simulated, and patient- is the absence of significant differences between the LG and database values for the determination of the SF, a clinically important parameter.

On the theoretical data, the LG showed better preservation of the original information in the renogram and a better recovery of the theoretical RRC (Figure 2). For MC simulations, the meanTT was closer to the expected values with a smaller dispersion (Table 4).

Table 4. Results of meanTT for MC-simulated studies for posterior and anterior images

Method	LG		MFF		
	Mean	SD	Mean	SD	p from t-test
Post	3.82	0.13	3.59	0.20	p<0.001
Ant	3.98	0.11	3.84	0.19	p<0.001

LG: Legendre generalized, MFF: Matrix Flemings' filtering, Post: Posterior, Ant: Anterior, SD: Standard deviation

The patient database does not contain any information about TT contrary to simulated data where the ground truth is known. This was part of the motivation to include the blinded physician diagnoses in the study, although the diagnosis does not always give evidence of a slowed TT or obstruction, and it remains difficult to define since no gold standard exists (18,19). The results obtained with patients had the same trend as the simulation data, suggesting that real-world data processing with LG behaves in the same manner. Moreover, the diagnoses were more in agreement with the values obtained with LG. The display of the RRC curve was also visually improved by the LG (Figure 6) method when reconvolution of the RRC with the input function is used as a quality control process, this is an interesting property.

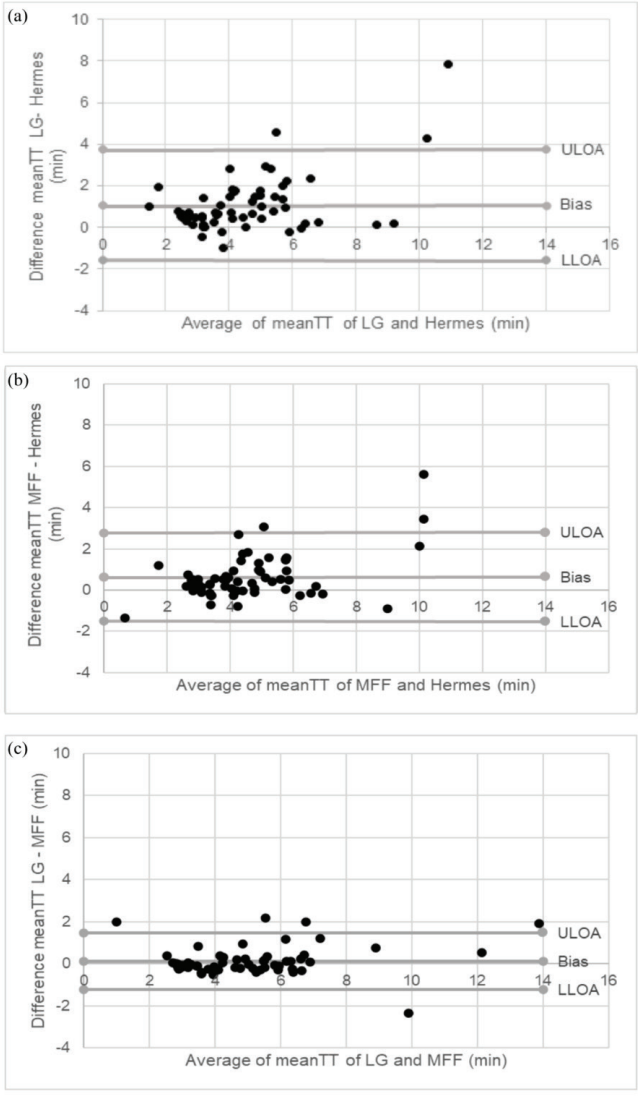

Figure 5. Bland-Altman plot of agreement between the whole kidney meanTT obtained between (a) LG and Hermes, (b) MFF and Hermes, and (c) LG and MFF. U and LLOA show two SD

meanTT: Mean transit time, LG: Legendre generalized, MFF: Matrix Flemings' filtering, U: Upper, LLOA: Lower levels of agreement, SD: Standard deviation

The filtration of the input curve and renogram by the LP instead of F121 before the matrix deconvolution was also investigated (data not shown). This globally resulted in an improvement of the deconvolution over F121 filtering. Nonetheless, the LG method used in this study presents even more improvements in the results due to the Moore–Penrose inversion matrix, which acts as a least square fit. Even if the matrix method is dependent on the first point, the filtration of the curves remains crucial (7). As pointed out by previous studies (9), F121 is not the best technique, but still remains the most used. Moreover, there is no assumption in the LG method on the form of the input function in contrast to some methods where the input function is modeled by mathematical functions (20). This LG method should not be seen as limited to kidney deconvolution but should be also applied to other types of dynamic study (work in progress) in nuclear medicine.

The LG method can be automated and has no extra computation needs compared with the matrix method.

In summary, the LP-based deconvolution appears to be a clinically feasible alternative to the classic matrix deconvolution for renogram analysis.

Study Limitations

The two main limitations of the study are the low number of variable parameters (SF and clearances) in the MC simulations and the lack of independently determined TT in the patient database. However, the results showed a similar trend in both simulated and real data to the benefit of our method.

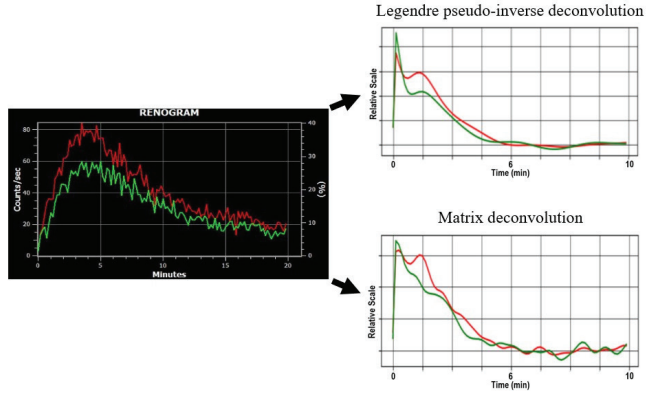

Figure 6. Example of the visual and stability improvement of the Legendre method compared with the matrix deconvolution technique on noisy renogram study for the right (green) and left (red) kidneys

Conclusion

The study demonstrates that the LG method is more stable on simulated data and further preserves the original information than the use of a traditional linear filter, like the usual and ISCORN-recommended 1-2-1 filter, combined with the matrix deconvolution. LG gave the best and a near-perfect correlation with the expected values for the SF determination of simulated and real patient data. With LG, the kidney meanTT was less influenced by the noise in simulated data. For patient data, we observed a better correlation between the medical diagnosis and the values obtained by the LG and a better visual rendering of the RRC curve.

Ethics

Ethics Committee Approval: CHU UCLouvain Namur Site De Sainte-Elisabeth Hospital Ethics Comitte (approval number: 08/21).

Informed Consent: The requirement to obtain informed consent was waived for this study because of its retrospective design.

Peer-review: Externally and internally peer-reviewed.

Authorship Contributions

Surgical and Medical Practices: F.X.H., I.M., B.W., Concept: M.D., Design: M.D., Data Collection or Processing: M.D., Analysis or Interpretation: M.D., A.S., Literature Search: M.D., A.S., Writing: M.D., A.S.

Conflict of Interest: No conflict of interest was declared by the authors.

Financial Disclosure: The authors declared that this study has received no financial support.

References

1. Bundinger TF, Jones T. History of nuclear medicine and molecular imaging. Comprehensive Biomedical Physics 2014;1-37.
2. Segre G. Compartmental models in the analysis of intestinal absorption. Protoplasma 1967;63:328-335.
3. Diffey BL, Hall FM, Corfield JR. The 99mTc-DTPA dynamic renal scan with deconvolution analysis. J Nucl Med 1976;17:352-355.
4. Prigent A, Cosgriff P, Gates GF, Granerus G, Fine EJ, Itoh K, Peters M, Piepsz A, Rehling M, Rutland M, Taylor A Jr. Consensus report on quality control of quantitative measurements of renal function obtained from the renogram: International Consensus Committee from the Scientific Committee of Radionuclides in Nephrourology. Semin Nucl Med 1999;29:146-159.
5. Werner RA, Chen X, Lapa C, Koshino K, Rowe SP, Pomper MG, Javadi MS, Higuchi T. The next era of renal radionuclide imaging: novel PET radiotracers. Eur J Nucl Med Mol Imaging 2019;46:1773-1786.
6. Fleming JS, Kemp PM. A comparison of deconvolution and the Patlak-Rutland plot in renography analysis. J Nucl Med 1999;40:1503-1507.
7. Durand E, Blaufox MD, Britton KE, Carlsen O, Cosgriff P, Fine E, Fleming J, Nimmon C, Piepsz A, Prigent A, Samal M; International Scientific Committee of Radionuclides in Nephrourology (ISCORN). International Scientific Committee of Radionuclides in Nephrourology (ISCORN) consensus on renal transit time measurements. Semin Nucl Med 2008;38:82-102.
8. Puchal R, Pavía J, González A, Ros D. Optimal filtering values in renogram deconvolution. Phys Med Biol 1988;33:831-845.
9. Fleming JS, Kenny RW. A comparison of techniques for the filtering of noise in the renogram. Phys Med Biol 1977;22:359-364.
10. Fleming JS. A technique for analysis of geometric mean renography. Nucl Med Commun 2006;27:701-708.
11. Destine M, Seret A. Legendre Polynomials: A fully automatic method for noise reduction in ^{99m}Tc-mercaptoacetyltriglycine renogram analysis. J Nucl Med Technol 2020;48:346-353.
12. Mendez-Perez JMR, Miquel Morales G. The finite Legendre transformation of generalized functions. Rocky Mt J Math 1998;28:1371-1389.
13. Penrose R. On best approximate solutions of linear matrix equations. Math Proc Cambridge Philos Soc 1956;52:17-19.
14. Brolin G, Gleisner KS, Ljungberg M. Dynamic (99m)Tc-MAG3 renography: images for quality control obtained by combining pharmacokinetic modelling, an anthropomorphic computer phantom and Monte Carlo simulated scintillation camera imaging. Phys Med Biol 2013;58:3145-3161.
15. Kempi V. A FORTRAN program for deconvolution analysis using the matrix algorithm method with special reference to renography. Comput Methods Programs Biomed 1987;24:107-116.
16. Fleming JS. Functional radionuclide imaging of renal mean transit time and glomerular filtration rate. Nucl Med Commun 1988;9:85-96.
17. Houston AS, Whalley DR, Skrypniuk JV, Jarritt PH, Fleming JS, Cosgriff PS. UK audit and analysis of quantitative parameters obtained from gamma camera renography. Nucl Med Commun 2001;22:559-566.
18. Nimmon C, Fleming JS, Šámal M. Probable range for whole kidney mean transit time values determined by reexamination of UK audit studies. Nucl Med Com 2008;9:1006-1014.
19. Taylor AT, Brandon DC, de Palma D, Blaufox MD, Durand E, Erbas B, Grant SF, Hilson AJW, Morsing A. SNMMI Procedure Standard/EANM Practice Guideline for Diuretic Renal Scintigraphy in Adults With Suspected Upper Urinary Tract Obstruction 1.0. Semin Nucl Med 2018;48:377-390.
20. Fleming JS, Goddard BA. A technique for the deconvolution of the renogram. Phys Med Biol 1974;19:546-549.

Original Article
Mol Imaging Radionucl Ther 2022;31:16-22 DOI:10.4274/mirt.galenos.2021.33154

The Evaluation of Preoperative ^{18}F-FDG PET/CT in Patients with Endometrial Cancer and the Correlation Between PET Parameters and Postoperative Pathology Results

Endometriyum Kanserli Hastalarda Preoperatif ^{18}F-FDG PET/BT'nin Değerlendirilmesi ve PET Parametreleri ile Postoperatif Patoloji Sonuçları Arasındaki Korelasyon

Özge Vural Topuz[1], Ayşegül Aksu[2], Sadife Rüya Erinç[1], Nedim Tokgözoğlu[3], Müge Öner Tamam[1]

[1]*University of Health Sciences Turkey, Prof. Dr. Cemil Taşçıoğlu City Hospital, Clinic of Nuclear Medicine, İstanbul, Turkey*
[2]*University of Health Sciences Turkey, Başakşehir Çam and Sakura City Hospital, Clinic of Nuclear Medicine, İstanbul, Turkey*
[3]*University of Health Sciences Turkey, Prof. Dr. Cemil Taşçıoğlu City Hospital, Clinic of Gynecology and Obstetrics, İstanbul, Turkey*

Abstract

Objectives: Endometrial cancer (EC) is the most common gynecological malignancy. The ^{18}fluorine-fluorodeoxyglucose (^{18}F-FDG) positron emission tomography/computed tomography (PET/CT) is used for initial staging, evaluating treatment response, and detecting recurrence. This study aimed to investigate the diagnostic value of preoperative PET/CT in EC staging and determine the volumetric PET parameters that are accurate predictors of histopathological tumor characteristics.

Methods: Preoperative PET/CT data of 66 patients with EC were retrospectively analyzed. Patients were divided into low and high-risk groups according to the European Society for Medical Oncology criteria. The maximum standardized uptake value (SUV_{max}), SUV_{mean}, metabolic tumor volume (MTV), and total lesion glycolysis (TLG) of the primary lesion and pathological lymph nodes were noted. The International Federation of Gynecology and Obstetrics (FIGO) classifications, histopathology, the depth of myometrial invasion (MI), lymph node metastasis (LNM), cervical stromal invasion (CSI), and tumor sizes were noted.

Results: The SUV_{max}, TLG, and MTV values of high and low-risk groups were significantly different. TLG was the most useful parameter in differentiating risk groups. PET/CT had 90% sensitivity, 96.3% specificity, 81.8% positive predictive value, 98.1% negative predictive value, and 95.45% accuracy in assessing LNM. MTV and TLG values in patients with non-endometrioid pathology were higher than those with endometrioid. The SUV_{max}, MTV, and TLG of patients with deep MI were higher than those with superficial MI. TLG values of patients with CSI were higher than those without CSI. Patients with LNM had higher MTV and TLG values than those without LNM. A significant difference was found in TLG, MTV, and SUV_{max} values between patients with FIGO stage I-II and patients with FIGO stage III and above.

Conclusion: SUV and volumetric parameters obtained from PET/CT, especially TLG, are strong predictors of tumor characteristics, such as MI and CSI, FIGO stages, and LNM, and are useful in noninvasively defining the risk groups in the preoperative period.

Keywords: Endometrial cancer, ^{18}F-FDG PET/CT, SUV_{max}, volumetric parameters

Öz

Amaç: Endometriyum kanserleri (EK) en sık görülen kadın genital sistemi malignitesidir. ^{18}Flor-florodeoksiglukoz (^{18}F-FDG) ile işaretli pozitron emisyon tomografisi/bilgisayarlı tomografi (PET/BT), EK'lerinde evreleme, tedavi yanıtının değerlendirilmesi ve nüks hastalığın belirlenmesi amacıyla sıkça kullanılmaktadır. Çalışmamızın amacı EK'lerinde preoperatif dönemde evreleme amaçlı yapılan PET/BT parametreleri ile postoperatif patoloji sonuçları arasındaki korelasyonun araştırılmasıdır.

Address for Correspondence: Özge Vural Topuz MD, University of Health Sciences Turkey, Prof. Dr. Cemil Taşçıoğlu City Hospital, Clinic of Nuclear Medicine, İstanbul, Turkey **Phone:** +90 212 314 55 55 **E-mail:** ozgevuraltopuz@gmail.com ORCID ID: orcid.org/0000-0001-7197-5866
Received: 16.05.2021 **Accepted:** 05.09.2021

Yöntem: Preoperatif evreleme amaçlı PET/BT çekimi yapılan 66 EK tanılı hasta çalışmaya dahil edildi. ^{18}F-FDG PET/BT çalışmalarında primer lezyonların ve patolojik lenf nodlarının maksimum standardize alım değeri (SUV_{maks}), SUV_{mean}, metabolik tümör hacmi (MTV) ve toplam lezyon glikoliz (TLG) değerleri ölçüldü. Postoperatif patoloji sonuçlarından Uluslararası Jinekoloji ve Obstetrik Federasyonu (FIGO) sınıflandırmaları, tümörlerin histolojik tipleri, myometrial invazyon derinlikleri (Mİ), maksimum tümör çapları, servikal stromal invazyonları ve lenf nodu metastaz bulguları kaydedildi.

Bulgular: Yüksek ve düşük riskli hasta grupları arasında TLG, MTV ve SUV_{maks} değerlerinde istatistiksel olarak anlamlı farklılık izlenirken, SUV_{mean}'de anlamlı fark mevcut değildi. Risk gruplarını ayırt etme gücü en yüksek olan parametre TLG olarak belirlendi. ^{18}F-FDG PET/BT'nin lenf nodu saptamada duyarlılığı %90; özgüllüğü %96,43, pozitif prediktif değeri %81,81, negatif prediktif değeri %98,18 ve doğruluğu %95,45 olarak hesaplandı. Non-endometrioid tümör tanılı hastalarda MTV ve TLG değerleri endometrioid tipe göre anlamlı yüksek saptandı. Mİ >1/2 olan hastalarda primer tümör SUV_{maks}, MTV ve TLG değerleri Mİ <1/2 olan gruba göre anlamlı düzeyde yüksekti. Servikal stromal invazyon izlenen hastalarda TLG değerleri, invazyon izlenmeyen gruba göre anlamlı düzeyde yüksekti. Histopatolojik olarak lenf nodu metastazı olan hastalarda primer tümörden elde edilen MTV ve TLG değerleri, lenf nodu metastazı olmayan hastalara göre daha yüksek düzeydeydi. FIGO I-II olan hastalar ile FIGO III ve üstü olan hastalar arasında TLG, MTV ve SUVmaks değerlerinde anlamlı farklılık izlendi.

Sonuç: ^{18}F-FDG PET/BT; TLG başta olmak üzere SUV ve volumetrik parametreleri sayesinde preoperatif dönemde tümöre ait myometrial invazyon, servikal stromal invazyon, FIGO evresi, lenf nodu metastazları gibi histopatolojik özellikleri ön görebilmeyi ve bu dönemde risk gruplarının da belirlenmesini sağlayabilecek önemli bir noninvaziv yöntemdir.

Anahtar kelimeler: Endometriyum kanseri, evreleme, ^{18}F-FDG PET/BT, SUV_{maks}, volumetrik parametreler

Introduction

Endometrial cancer (EC) is the fifth most common cancer among females worldwide and is the most common gynecological malignancy in developed countries. The most important prognostic factors used for EC are staging, grading, tumor histopathology, depth of myometrial invasion (MI), tumor size, cervical stromal invasion (CSI), and lymph node metastases (LNM) (1).

EC is surgicopathologically staged according to the International Federation of Gynecology and Obstetrics (FIGO) system. The current 2010 FIGO recommendation for the surgical staging of EC includes hysterectomy, bilateral salpingo-oophorectomy, pelvic and paraaortic lymphadenectomy, and biopsy of any suspicious lesions (2). Stage I reflects EC that is confined to the uterine corpus and is further divided into stage IA (none or <50% MI) and IB (equal to or >50% MI). Tumors that invade cervical stromal but do not extend beyond the uterus are defined as stage II. Stage III represents a tumor that has spread beyond the uterus but not outside the true pelvis and is further divided into stage IIIA (uterine serosa and/or adnexa invasion), stage IIIB (parametrium and/or vaginal involvement), stage IIIC1 (positive pelvic nodes), and IIIC2 (positive paraaortic lymph nodes). Stage IVA includes tumors with bladder or bowel metastases and stage IVB with distant metastases (3).

Several prognostic factors for EC were identified, including an advanced FIGO surgical stage, non-endometrioid histological subtype, poorly differentiated histology, more than half MI, a larger tumor size, lymphovascular space involvement (LVSI), CSI, ovarian metastasis, and pelvic/paraaortic LNM (4,5).

The maximum standardized uptake value (SUV_{max}), a semiquantitative parameter determined by positron emission tomography (PET), is described as the highest ^{18}fluorine-fluorodeoxyglucose (^{18}F-FDG) uptake of a single-pixel within a region of interest that is manually drawn over a hypermetabolic lesion. SUV_{max} represents the measurement from only one voxel of the most hypermetabolic area of a tumor lesion and only shows the highest intensity of ^{18}F-FDG uptake, thus it cannot reflect the whole tumor metabolic burden and can be affected by various patient characteristics and imaging parameters. The SUV_{max} has some limitations and it cannot be used to assess the overall glucose metabolic activity of a tumor mass, thus other useful PET parameters are used, which can better reflect metabolic tumor burden than SUV_{max}, such as metabolic tumor volume (MTV) to measure the overall glucose metabolic activity of a tumor lesion and total lesion glycolysis (TLG) that combines the information of metabolic activity and tumor volume (6,7).

This study aimed to investigate the diagnostic value of the preoperative ^{18}F-FDG PET/computed tomography (CT) for EC staging and determine the volumetric ^{18}F-FDG PET/CT parameters that are accurate predictors of histopathological tumor characteristics.

Materials and Methods

Patient Characteristics

From January 2016 to November 2017, data from patients with histologically confirmed EC who had undergone a preoperative PET/CT scan before total abdominal hysterectomy and bilateral salpingo-oophorectomy with and without pelvic and/or paraaortic lymphadenectomy

were retrospectively analyzed. All patients had PET/CT scans in 6 weeks leading up to their surgery.

Patients with any of the following criteria were excluded from the study: Another malignant disease, tumors with no ^{18}F-FDG avidity, uncontrolled diabetes mellitus, neoadjuvant chemotherapy or preoperative radiotherapy, and inoperable tumor.

Diagnoses were confirmed by preoperative endometrial biopsy and are surgically staged following the FIGO criteria.

Histology, tumor grade, maximum tumor diameter, MI, CSI, and LNM were noted. All patients were divided into low-risk and high-risk groups according to the European Society for Medical Oncology criteria. Patients with endometrioid histology, histological grades 1 or 2, and MI of <1/2 were classified as the low-risk group, whereas those with histological grade 2/3 (G2/3), positive LVSI, or MI of ≥1/2 were the high-risk group (8).

Image Analysis

Whole-body PET/CT imaging was performed on a biograph (Siemens Biograph 6, Chicago, IL, USA) using a full-ring HI-REZ LSO PET and a six-slice CT scanner.

All patients fasted for at least 5 h before the PET/CT imaging. The serum glucose levels measured at the time of ^{18}F-FDG injections were <150 mg/dL in all patients. Approximately, 50 min later, an initial low-dose non-enhanced CT scan was performed with the following parameters: 40-60 mAs, 140 kV, and 5-mm section thickness. Positron emission scanning with 3 min per bed position was then acquired on the identical transverse field of view in the caudocranial direction. The total scanning time was approximately 25 min per patient. CT transmission images were used for attenuation correction, and all images were reconstructed and stored in axial, coronal, and sagittal slices.

Image analysis and interpretation were performed on a dedicated workstation (Esoft). A semi-automatic ellipsoid-shaped volume of interest (VOI) around the primary uterine tumors that included the entire lesion in the axial, sagittal, and coronal planes was drawn. SUV_{max}, SUV_{mean}, and MTV of the primary uterine tumors that were automatically generated by the software on the workstation were recorded. Voxels greater than the set threshold of 41% of SUV_{max} in the VOI were used for MTV and SUV_{mean} measurement. After the MTV measurement, TLG was also calculated using the following equation: $TLG = SUV_{mean} \times MTV$.

Ethical Approval

University of Health Sciences Turkey, Okmeydani Training and Research Hospital Ethics Committee approval was obtained (number: 48670771-514.10) and all patients signed written informed consent.

Statistical Analysis

Number Cruncher Statistical System (Kaysville, Utah, USA) was used for statistical analysis. P values of <0.05 were considered statistically significant. Normally distributed data were presented as mean ± standard deviation, whereas non-normal distributed data were given as median (range). Data with abnormal distribution were analyzed using the Mann-Whitney U test. The Mc Nemar test was used to compare dependent categorical data. Spearman's correlation analysis was used to evaluate the relationship between variables. The area under the receiver operating characteristic (ROC) curve (AUC) was presented as a measure of discrimination. Cut-off values were identified from the ROC curves using the Youden index. The percentages of sensitivity and specificity were determined at these cut-off values.

Results

Patients and tumor characteristics are listed in Table 1.

This study included 66 patients with an age range of 41 to 84 years (mean age: 63.56±10.11), of whom 87.9% (58/66) were postmenopausal.

Table 1. Patients and tumor characteristics

		n	%
Menopausal status	Premenopausal	8	12.1
	Postmenopausal	58	87.9
Pathology	Endometrioid	48	72.7
	Non-endometrioid	18	27.3
FIGO stage	IA	25	37.9
	IB	21	31.8
	II	2	3.0
	IIIA	1	1.5
	IIIC1	7	10.6
	IIIC2	8	12.1
	IVB	2	3.0
Myometrial invasion	<1/2	27	40.9
	>1/2	39	59.1
Cervical stromal invasion	No	54	81.8
	Yes	12	18.2
Lymph node metastases (pathological)	No	56	84.8
	Yes	10	15.2
Lymph node metastases (PET/CT)	No	55	83.3
	Yes	11	16.7

FIGO: International Federation of Gynecology and Obstetrics, PET: Positron emission tomography, CT: Computed tomography

The median SUV_{max}, MTV, and TLG of 66 primary uterine tumors were 16.8 (range: 3.5-41.1), 27.81 mL (range: 0.1-251), and 225.19 g (range: 0.2-2347.3), respectively.

Of the 66 patients, 54 (81.8%) were postoperatively diagnosed with high-risk carcinoma and 12 (18.2%) with low-risk carcinoma. Patients with high-risk carcinoma showed significantly higher SUV_{max}, TLG, and MTV than those with low-risk carcinoma. The mean SUV_{max} value of patients in the low-risk and high-risk groups was 11.6±5.5 and 17.9±8.4, respectively (p=0.018). The mean TLG value of patients in the low-risk and high-risk groups was 28.3±25.7 g and 268.9±439.8 g, respectively (p<0.001). The mean MTV value of patients in the low-risk and high-risk groups was 5.9±6.5 mL and 32.6±50 mL, respectively (p=0.002). The SUV_{mean} did not show a significant difference between the two groups (p=0.14).

The TLG had the highest AUCs for predicting the high-risk group (p<0.001, AUC: 0.852, 95% confidence interval: 0.753-0.951). ROC curve analysis was performed to determine the cut-off value of TLG for distinguishing high-risk and low-risk disease groups. The optimal TLG cut-off value of 52.7 g that was determined by ROC analysis showed 74.1% sensitivity and 91.7% specificity for risk stratification.

TLG, MTV, and SUV_{max} values of patients with FIGO IB (n=20) were significantly higher than those with FIGO IA (n=26) (p<0.001, p=0.004, and p=0.025, respectively). Tumor sizes obtained from postoperative pathology results of these two groups were also considerably different (p<0.001).

A statistically significant difference was found in the TLG, MTV, and SUV_{max} values in patients with tumors that are limited to the uterus (FIGO I and II) (n=48) compared to those with FIGO 3 criteria and above (p<0.001, p<0.001, and p=0.045, respectively). According to ROC curve analysis results for the differentiation of FIGO stage I or II from stage III and above, the cut-off value of SUV_{max} was 16 with 72.2% sensitivity and 64.6% specificity, whereas the MTV was 23.35 mL with 66.7% sensitivity and 81.2% specificity and 173.45 g for TLG with 66.7% sensitivity and 83.3% specificity. A substantial difference was also detected in tumor sizes obtained from postoperative pathology results between these two groups. The mean tumor size of patients with FIGO stages I and II was 3.52±1.95 cm, whereas the mean tumor size was 6.06±2.68 cm in patients with higher FIGO stages (p<0.001).

Patients with non-endometrioid pathology (n=18) had significantly higher MTV and TLG parameters compared to patients with endometrioid adenocarcinoma (p=0.008 vs. 0.019, respectively). When ROC curve analysis was performed to determine the cut-off value of MTV and TLG to differentiate non-endometrioid adenocarcinoma from endometrioid, the optimal cut-off value of MTV was 28.7 mL with 55.6% sensitivity and 81.2% specificity. The optimal cut-off value of TLG was 255 g with 50% sensitivity and 87.5% specificity. ROC curve analysis did not show a significant SUV_{max} cut-off value for histopathologic types. Tumor sizes showed a significant difference in the non-endometrioid subtype of EC compared with the endometrioid subtype (p=0.001). Additionally, the rate of LNM was higher (38.9%) in patients with non-endometrioid pathology than in patients with endometrioid adenocarcinoma (6.3%) (p=0.001).

The mean maximum primary tumor diameter on final pathology was 4.2±2.4 cm (range: 0.5-12.5 cm).

A moderate correlation between the TLG and MTV values that are obtained in the preoperative period and the postoperative tumor diameter (p<0.001, rho: 0.661; p<0.001, rho: 0.557, respectively). The correlation of tumor sizes with SUV_{max} values was weaker (p=0.001, rho: 0.388).

The SUV_{max}, MTV, and TLG values of patients with a maximum tumor size of ≥4 cm were higher than those with <4 cm (p=0.028, p<0.001, p<0.001, respectively).

Of the patients, 16.7% had LNM in the preoperative PET scan and 15.2% had LNM in the postoperative pathological results. No significant difference was found between the preoperative PET scan and postoperative pathological results (p>0.05). PET/CT identified LNM in 9 out of 10 patients with LNM at final pathology, sensitivity, specificity, positive predictive value, negative predictive value, and accuracy of 90%, 96.43%, 81.81%, 98.18%, and 95.45%, respectively (Table 2).

The MTV and TLG values were significantly higher in tumors with LNM compared to those without LNM (p=0.024 and p=0.035, respectively). However, no difference was observed in SUV_{max} values. Pathologically proven LNM showed a weak correlation with tumor diameter (p=0.011, rho: 0.311), MTV (p=0.022, rho: 0.281), TLG (p=0.034, rho: 0.262), MI (p=0.004, rho: 0.352), and CSI (p=0.004, rho: 0.349).

The SUV_{max}, MTV, and TLG values of the primary lesion in patients with deep MI (MI ≥1/2) (n=39) (59.1%) were significantly higher than those with superficial MI (MI <1/2) (p<0.05). SUV_{mean} value did not differ between these two groups (p>0.05) (Table 3).

Patients with CSI had higher TLG values than those without (p<0.05). No statistically significant difference was found in MTV, SUV_{max}, and SUV_{mean} values between these two groups (Table 3).

Table 2. Metastatic lymph node status according to preoperative PET/CT data and postoperative pathology results								
		Pathology						p
	Positive		Negative		Total			
	n	%	n	%	n	%		
PET/CT	Positive	9	13.6	2	3.0	11	16.7	1.000
	Negative	1	1.5	54	81.8	55	83.3	
	Total	10	15.2	56	84.8	66	100	
Sensitivity			90.00					
Specificity			96.43					
Positive predictive value			81.81					
Negative predictive value			98.18					

*p<0.05 Mc Nemar test, PET: Positron emission tomography, CT: Computed tomography

Table 3. Association between metabolic parameters and surgicopathological findings in endometrial cancer patients						
	Myometrial invasion		p	Cervical stromal invasion		p value
	<1/2	>1/2		Yes	No	
Tumor SUV_{max} Median (range)	13 (3.5-29)	16.2 (5.3-41.1)	0.019*	15.4 (5.3-41.1)	15.4 (3.5-31.9)	0.954
Tumor SUV_{mean} Median (range)	5.7 (3.1-18.8)	7.6 (3.4-24.8)	0.098	7.3 (3.1-20.7)	7.6 (3.7-24.8)	0.746
Tumor MTV Median (range)	3.3 (0.1-34.5)	22 (1.1-251)	**0.001***	10.5 (0.1-251)	20.6 (4.7-106.6)	0.090
Tumor TLG Median (range)	41.6 (0.2-588.9)	168.1 (15.6-2347.3)	0.001*	67.8 (0.2-2347.3)	145.3 (17.2-900.7)	0.049*

*p<0.05 Mann-Whitney U test, SUV_{max}: Maximum standardized uptake value, SUV_{mean}: Mean standardized uptake value

The SUV_{max}, SUV_{mean}, MTV, and TLG values of the primary tumor did not differ with the pre or postmenopausal conditions (p>0.05).

Discussion

Preoperative identification of some prognostic factors, such as patients with deep MI, LNM, histology, and differentiating high-risk from those with low-risk may be critical in planning the surgical procedure or treatment approach in patients with EC. SUV_{max}, MTV, and TLG are PET/CT parameters commonly used in the preoperative assessment of EC. SUV_{max} and volumetric parameters that are obtained from ^{18}F-FDG PET/CT differ in high- and low-risk patient groups and FIGO stages. Therefore, ^{18}F-FDG PET/CT allows us to access this information in the preoperative period.

Our results showed that MTV and TLG are superior to SUV_{max} as preoperative predictors of clinicopathologic characteristics. SUV_{max} focuses on a single-pixel with the highest ^{18}F-FDG uptake within the tumor, thus it cannot be used to evaluate the overall metabolic state of the tumor. Mean tumor volume measures the volume of a tumor bulk that is metabolically active. Thus, it reflects the overall metabolic state of the tumor.

Liu et al. (9) determined the cut-off value for TLG as 51.7 g and revealed a sensitivity of 84.2% and a specificity of 77.3% for TLG in distinguishing high-risk and low-risk diseases (AUC: 0.778). Similarly, our study revealed significantly higher TLG and MTV values in the high-risk group, whereas no difference in SUV_{max} values. The ROC curve analysis was performed to determine the most useful metabolic primary tumor parameter in differentiating high-risk and low-risk EC, and our series revealed that TLG had the highest AUCs for predicting the high-risk group. A TLG cut-off of 52.7 g determined by ROC analysis showed 74.1% sensitivity and 91.7% specificity for risk stratification. Similar to our study, Kitajima et al. (5) revealed AUCs for distinguishing high-risk from low-risk carcinoma as 0.797 for TLG. The optimal determined TLG cut-off value of 70.2 g by ROC analysis was found to have 72.0% sensitivity and 74.2% specificity for risk stratification (5).

Our study revealed higher MTV and TLG values in patients with non-endometrioid subtype compared to those with endometrioid subtype, but without significant difference in

SUV_{max} values. Moreover, tumor diameter from pathology samples in the non-endometrioid subtype was also significantly higher (p=0.001). The obtained volumetric data from ^{18}F-FDG PET/CT was also supported by postoperative pathology results. Few studies have analyzed SUV and volumetric PET parameters between these two pathological subtypes. Mapelli et al. (10) included 57 patients in their study and found that SUV_{max} and SUV_{mean} were the only parameters that distinguish endometrioid from non-endometrioid subtype. They did not observe any difference between the MTV and TLG values of these two groups. Other studies revealed no significant difference in ^{18}F-FDG PET/CT parameters regarding these two pathological subtypes. Husby et al. (11) included 129 patients and Kitajima et al. (5) with 56 patients noted no difference between the endometrioid and non-endometrioid histological types in the SUV_{max}, MTV, and TLG values. The reason for the discrepancy between the studies may have been due to the differences in patient datasets. Our study group revealed endometrioid pathology in 72.7% of patients and non-endometrioid pathology in 27.3%, whereas Kitajima et al. (5) revealed only 5 (9%) patients with non-endometrioid pathology. The number of patients with non-endometrioid adenocarcinoma is very low, thus a significant difference could not be determined between the SUV_{max}, MTV, and TLG values of the two groups.

The difference in SUV_{max} values of the primary tumor according to nodal metastasis was not statistically significant; however, the MTV and TLG values of the primary tumors were significantly higher in patients with nodal metastasis. This was compatible with previous studies (5,9). These findings also show the superiority of MTV and TLG to SUV_{max}. In the literature, the relationship between the SUV_{max} values of the primary tumor and presence of LNM is unclear. Husby et al. (11) detected a considerable difference between the SUV_{max} values of these two groups, whereas Stewart et al. (12) found no differences in primary tumor characteristics on PET/CT imaging between patients with positive and negative lymph nodes.

Our study revealed significantly higher TLG values of patients with CSI. The study of Kitajima et al. (5) revealed a significantly higher MTV and TLG in patients with CSI, whereas other studies revealed a significant difference only in MTV values (11,13). The discrepancy among these studies may have been due to patient numbers. However, these results suggest that volumetric ^{18}F-FDG PET/CT parameters are more successful than SUV_{max} in predicting CSI.

Similar to other studies in the literature [Kitajima et al. (5), Husby et al. (11), and Fasmer et al. (13)], SUV_{max}, MTV, and TLG were found to be reliable predictors of deep MI in our study. Data that are obtained from PET/CT in the preoperative period may be helpful in non-invasively predicting the depth of MI.

Study Limitations

Our study had several limitations. First, it was retrospectively designed. Moreover, non-parametric tests, which are usually less powerful than corresponding parametric tests, were used due to insufficient normal distribution.

Conclusion

Obtained volumetric parameters from ^{18}F-FDG PET/CT, especially TLG, can predict tumor characteristics, such as FIGO stages, LNM, MI, and cervical CSI, in the preoperative period. Furthermore, these parameters may alter the type of operation and the approach of treatment by providing more accurate risk classification.

Ethics

Ethics Committee Approval University of Health Sciences Turkey, Okmeydani Training and Research Hospital Ethics Committee approval was obtained (number: 48670771-514.10).

Informed Consent: All patients signed written informed consent.

Peer-review: Externally peer-reviewed.

Authorship Contributions

Surgical and Medical Practices: N.T., Concept: Ö.V.T., A.A., S.R.E., M.Ö.T., Design: Ö.V.T., A.A., Data Collection or Processing: Ö.V.T., A.A., Analysis or Interpretation: A.A., Literature Search: Ö.V.T., A.A., Writing: Ö.V.T., A.A., S.R.E.

Conflict of Interest: No conflict of interest was declared by the authors.

Financial Disclosure: The author declared that this study has received no financial support.

References

1. Berretta R, Patrelli TS, Migliavacca C, Rolla M, Franchi L, Monica M, Modena AB, Gizzo S. Assessment of tumor size as a useful marker for the surgical staging of endometrial cancer. Oncol Rep 2014;31:2407-2412.
2. Edge SB, Compton CC. The American Joint Committee on Cancer: the 7th edition of the AJCC cancer staging manual and the future of TNM. Ann Surg Oncol 2010;17:1471-1474.
3. Creasman W. Revised FIGO staging for carcinoma of the endometrium. Int J Gynaecol Obstet 2009;105:109.
4. Wright JD, Barrena Medel NI, Sehouli J, Fujiwara K, Herzog TJ. Contemporary management of endometrial cancer. Lancet 2012;379:1352-1360.
5. Kitajima K, Suenaga Y, Ueno Y, Maeda T, Ebina Y, Yamada H, Okunaga T, Kubo K, Sofue K, Kanda T, Tamaki Y, Sugimura K. Preoperative risk

stratification using metabolic parameters of (18)F-FDG PET/CT in patients with endometrial cancer. Eur J Nucl Med Mol Imaging 2015;42:1268-1275.

6. Shim SH, Kim DY, Lee DY, Lee SW, Park JY, Lee JJ, Kim JH, Kim YM, Kim YT, Nam JH. Metabolic tumour volume and total lesion glycolysis, measured using preoperative 18F-FDG PET/CT, predict the recurrence of endometrial cancer. BJOG 2014;121:1097-1106; discussion 1106.
7. Liu DD, Li J, Li X, Xie L, Qin L, Peng F, Cheng MH. Prognostic value of metabolic tumor volume and total lesion glycolysis from ^{18}F-FDG PET/CT in lymph node metastases and risk stratification of endometrial carcinoma. J Gynecol Oncol 2019;30:e89.
8. Bendifallah S, Canlorbe G, Raimond E, Hudry D, Coutant C, Graesslin O, Touboul C, Huguet F, Cortez A, Daraï E, Ballester M. A clue towards improving the European Society of Medical Oncology risk group classification in apparent early stage endometrial cancer? Impact of lymphovascular space invasion. Br J Cancer 2014;110:2640-2646.
9. Liu DD, Li J, Li X, Xie L, Qin L, Peng F, Cheng MH. Prognostic value of metabolic tumor volume and total lesion glycolysis from ^{18}F-FDG PET/CT in lymph node metastases and risk stratification of endometrial carcinoma. J Gynecol Oncol 2019;30:e89.
10. Mapelli P, Bergamini A, Fallanca F, Rancoita PMV, Cioffi R, Incerti E, Rabaiotti E, Petrone M, Mangili G, Candiani M, Gianolli L, Picchio M. Prognostic role of FDG PET-derived parameters in preoperative staging of endometrial cancer. Rev Esp Med Nucl Imagen Mol (Engl Ed) 2019;38:3-9.
11. Husby JA, Reitan BC, Biermann M, Trovik J, Bjørge L, Magnussen IJ, Salvesen ØO, Salvesen HB, Haldorsen IS. Metabolic tumor volume on 18F-FDG PET/CT improves preoperative identification of high-risk endometrial carcinoma patients. J Nucl Med 2015;56:1191-1198.
12. Stewart KI, Chasen B, Erwin W, Fleming N, Westin SN, Dioun S, Frumovitz M, Ramirez PT, Lu KH, Wong F, Aloia TA, Soliman PT. Preoperative PET/CT does not accurately detect extrauterine disease in patients with newly diagnosed high-risk endometrial cancer: A prospective study. Cancer 2019;125:3347-3353.
13. Fasmer KE, Gulati A, Dybvik JA, Ytre-Hauge S, Salvesen Ø, Trovik J, Krakstad C, Haldorsen IS. Preoperative 18F-FDG PET/CT tumor markers outperform MRI-based markers for the prediction of lymph node metastases in primary endometrial cancer. Eur Radiol 2020;30:2443-2453.

Original Article
Mol Imaging Radionucl Ther 2022;31:23-32 DOI:10.4274/mirt.galenos.2021.48343

Investigation of Added Value of Imaging Performed in a Prone Position to Standard ^{18}F-Fluorodeoxyglucose Positron Emission Tomography/Computed Tomography Imaging for Staging in Patients with Breast Cancer

Meme Kanserli Hastalarda Evreleme için Yapılan Standart ^{18}F-Florodeoksiglukoz Pozitron Emisyon Tomografi/Bilgisayarlı Tomografi Görüntülemesine Yüzüstü Pozisyonda Yapılan Görüntülemenin Katkısının Araştırılması

Ezgi Başak Erdoğan, Mehmet Aydın

Bezmialem Vakıf University Faculty of Medicine, Department of Nuclear Medicine, İstanbul, Turkey

Abstract

Objectives: To investigate whether additional imaging in a prone position has any value to the supine whole-body ^{18}fluorine-fluorodeoxyglucose positron emission tomography/computed tomography (PET/CT) images by comparing the visual and quantitative data about a local disease in the breast and axilla for the initial staging of breast cancer (BC).

Methods: In this study, a total of 91 female patients with the BC were studied. Both the supine and prone images were examined based on the axial diameter, number and location of the primary tumor, local invasion signs of the tumor, the number of axillary lymph nodes with a suspected metastasis, metabolic parameters of the primary tumor and axillary lymph nodes, and registration artifacts of the PET and CT images were evaluated individually. These findings were compared with the histopathological data obtained after a surgery.

Results: In the evaluation of a supine and prone imaging, tumor diameter and metabolic tumor volume (MTV) values of the breast lesions were greater in the supine position than in the prone position. However, there was no significant difference found between the other metabolic parameters of a primary tumor and axilla in both positions. In the supine and prone images, accuracy for skin involvement was 84% and 91.3%, respectively.

Conclusion: In our study, we observed that, obtaining additional images in the prone position does not significantly benefit the evaluation of a local disease. The average values of the primary tumor diameter and MTV in the prone position appear to be smaller than the one in the supine position. However, the prone imaging in the patients with a newly diagnosed BC may be beneficial in selected patients and may contribute to preventing the false-positive results especially in patients with a suspected skin involvement.

Keywords: Breast cancer, positron emission tomography/computed tomography (PET/CT), ^{18}F-fluorodeoxyglucose (^{18}F-FDG), prone position

Öz

Amaç: Meme kanserinin ilk evrelendirmesi için yapılan görüntülemede, meme ve aksilladaki lokal hastalık hakkındaki görsel ve niceliksel verileri karşılaştırarak, pron pozisyonda bölgesel görüntülemenin, standart tüm vücut ^{18}flor-florodeoksiglukoz pozitron emisyon tomografisi/bilgisayarlı tomografi (PET/BT) görüntülerine ek katkısının olup olmadığını araştırmak.

Yöntem: Doksan bir meme kanserli kadın hasta incelendi. Hem supin hem de pron görüntüler; aksiyal çap, primer tümörün sayısı ve yeri, tümörün lokal invazyon bulguları, metastaz şüpheli aksiller lenf nodu sayısı, primer tümör ve aksillar lenf nodlarının metabolik parametreleri ile, PET ve BT görüntülerinin füzyon artefaktları ayrı ayrı değerlendirildi. Bu bulgular ameliyat sonrası elde edilen histopatolojik verilerle karşılaştırıldı.

Address for Correspondence: Ezgi Başak Erdoğan MD, Bezmialem Vakif University Faculty of Medicine, Department of Nuclear Medicine, İstanbul, Turkey
Phone: +90 212 533 48 95 **E-mail:** erdogan_ezgi@yahoo.com.tr ORCID ID: orcid.org/0000-0002-6636-9324
Received: 30.04.2021 **Accepted:** 05.09.2021

Bulgular: Meme lezyonlarının tümör çapı ve metabolik tümör hacmi (MTV) değerleri supin pozisyonda, pron pozisyona göre daha yüksekti. Bununla birlikte, her iki pozisyonda alınan görüntülerde primer tümör ve aksillanın diğer metabolik parametreleri arasında önemli bir fark yoktu. Supin ve pron görüntülerde deri tutulumunun doğruluğu sırasıyla %84 ve %91,3 idi.

Sonuç: Çalışmamızda, pron pozisyonda ek görüntü almanın, lokal hastalık değerlendirmesine anlamlı fayda sağlamadığını gözlemledik. Pron pozisyonda primer tümör çapı ve MTV'nin ortalama değerleri, sırtüstü pozisyondakinden daha küçük bulundu. Bununla birlikte, yeni tanı almış meme kanseri hastalarında, pron görüntüleme, seçilmiş hastalarda faydalı olabilir ve özellikle cilt tutulumu şüphesi olan hastalarda yanlış pozitif sonuçların önlenmesine katkıda bulunabilir.

Anahtar kelimeler: Meme kanseri, pozitron emisyon tomografisi/bilgisayarlı tomografi (PET/BT), ^{18}F-florodeoksiglukoz (^{18}F-FDG), pron pozisyonu

Introduction

^{18}Fluorine-fluorodeoxyglucose (^{18}F-FDG) positron emission tomography/computed tomography (PET/CT), which is widely used in the several malignancies due to various indications, it has a limited contribution to the primary tumor staging, its role in a nodal staging and detection of the distant metastases has been proven (1,2). Although the role of ^{18}F-FDG PET/CT in the evaluation of a primary tumor and axillary lymph node in staging of breast cancer (BC) is still limited compared with the radiological imaging methods such as: Magnetic resonance imaging (MRI) and ultrasonography, this field is open to developments because of the imaging modalities such as: Positron emission mammography and hybrid PET/MRI systems. Several articles have stated that the ^{18}F-FDG PET/CT imaging in a prone position is more suitable for fusion with a MRI and helps to increase the specificity of the breast MRI (3,4). The standard acquisition protocol in the ^{18}F-FDG PET/CT scan is imaging the area between a vertex and upper thigh in the supine position. It has been speculated that imaging of the breast and axillary region in a prone position in patients with a BC will provide a better diagnostic information because of better differentiation of deep breast tissue structures from the axilla and the chest wall; however, data regarding whether the additional images acquired in a prone position significantly adds value to the evaluation of a local disease in these patients are limited. There are relatively limited number of studies that suggest that the additional imaging in a prone position demonstrates more axillary lymph node involvement (5) and provide evidence that the imaging in a prone position is more successful in both the visualizing metastatic axillary lymph nodes and detecting MF (6,7). Further, ^{18}F-FDG PET/CT does not have a major role for the purpose of local staging such as: MF of the primary tumor, axillary node staging, skin, and nipple invasion, and it is speculated that it may have a decisive role in this field, particularly with a introduction of the hybrid PET/MRI systems (8). Therefore, if additional local imaging in a prone position may provide an important additional diagnostic information in the evaluation of the primary tumor and axillary lymph node, including prone imaging to the ^{18}F-FDG PET/CT protocol for staging in patients with BC will be possible.

Materials and Methods

Patients

The institutional review board approved this retrospective study, and the need for a written informed consent was waived. Ethical permission for the study was given by the Ethics Committee of Bezmialem Vakif University Faculty of Medicine with a letter dated 16 April, 2019, numbered 08/131. The medical records of the patients who underwent ^{18}F-FDG PET/CT imaging for the staging purposes at our clinic between the year 2012 and 2018 were retrospectively reviewed. Ninety-six female patients over the age of 18 years with a histopathologically proven diagnosis of the BC underwent PET/CT after a histopathological diagnosis and before the neoadjuvant chemotherapy, and had an additional image acquired in a prone position along with the standard supine imaging. Five patients with a low ^{18}F-FDG affinity were excluded from the study group, and 91 patients were included in this study. However, because bilateral BC was detected in three of the 91 patients, 94 breast tumors and axilla were evaluated.

^{18}F-FDG PET/CT Image Acquisition

All the patients underwent a ^{18}F-FDG PET/CT imaging using a high-resolution PET scanner fitted with an integrated 16-slice multidetector CT (Biograph 16 PET/CT, Siemens, Chicago, IL, USA). Prior to the ^{18}F-FDG injection, blood glucose levels were measured in the well-hydrated patients who had fasted for at least 4 hrs prior to their scheduled PET/CT sessions. ^{18}F-FDG (296-555 MBq) was intravenously administered to the patients whose blood sugar glucose levels were <200 mg/dL. After the injection, patients were allowed to rest in a quiet comfortable room for 45-60 min to allow a complete ^{18}F-FDG biodistribution. Subsequently, each patient emptied their urinary bladder and was instructed to lie in a supine position on the PET/CT scanner bed. For attenuation correction, and the anatomical

localization, low-mAs CT scans from the top of the head to the upper thigh were obtained accordingly. Immediately after the completion of CT scans, PET images of the region from the vertex to the upper thigh were acquired for about 3 min per bed position. Attenuation-corrected PET images were reconstructed using an ordered-subset expectation maximization iterative reconstruction algorithm (18 subsets, 2 iterations). After imaging of the whole-body in a standard supine position, local imaging was performed in the prone position, including both the breast tissue and axilla, immediately after in six patients and as a late imaging for 85 patients (105-120 min after the injection). A custom-made polystyrene breast support device was used during the imaging in a prone position.

Visual and Semi-quantitative Image Analysis

All the images were evaluated by the two experienced nuclear medicine specialists. For all the patients, the diameter of the primary tumor in the axial plane of the breast tissue, the number and distribution of the tumor [unifocality (UF), multifocality (MF), multicentricity (MC)], malignant skin involvement, nipple invasion, pectoral muscle invasion, the number of the potential metastatic lymph nodes in the axilla, presence or absence of the distant metastasis, PET/CT fusion misregistration due to a respiratory or motion artifacts, and the metabolic activity of the primary tumor and axillary lymph nodes were noted in both the supine and prone position images. Metabolic activities of a primary tumor and axillary lymph nodes were evaluated visually by comparison with the background activity as well as by the semi-quantitative measurement [maximum standardized uptake value (SUV_{max})]. If multiple primary tumors were in the breast, the size and metabolic activity of the dominant lesion were evaluated. In addition, among the axillary lymph nodes, the SUV_{max} of the lymph node with a highest metabolic activity was also measured. LIFEx software was used to obtain the metabolic tumor volume (MTV) and total lesion glycolysis [(TLG): MTV × SUV_{mean}], and SUV_{mean} of the primary tumor and axillary lymph nodes (Figure 1) (9). We obtained the MTV and TLG values in both positions using threshold values of SUV_{max} 2.5 for the primary tumor and SUV_{max} of 1.5 for the axilla. Ultimately, we obtained the SUV_{max}, SUV_{mean}, MTV, and TLG values of 92 cases for primary tumor, since remaining two cases were excluded because of their very low ^{18}F-FDG uptake. In addition, 24 axilla were excluded because of a very low or no ^{18}F-FDG uptake in some axillary lymph nodes.

Statistical Analysis

SPSS version 20.0 was used for the statistical analysis. Paired samples t-test was used to evaluate the difference between the mean primary tumor and axilla SUV_{max}, SUV_{mean}, MTV, and TLG values, and the primary tumor size on images obtained in the supine and prone positions, if there was a normal distribution, or the Wilcoxon signed ranked test was used if there was no normal distribution observed. For both the positions, accuracy, sensitivity, specificity, positive predictive value and negative predictive values for the nipple involvement, skin involvement, and pectoral muscle involvement were calculated accordingly. Mann-Whitney U test was used to compare the independent groups with a non-parametric distribution. Pearson correlation analysis was used to evaluate the correlation between Ki-67 proliferation index and the SUV_{max} of a primary tumor and axillary lymph nodes. Variables with the normal distribution were expressed as mean ± standard deviation, and those without a normal distribution were expressed as median (minimum-maximum) values.

Results

The mean age of the 91 female patients with a biopsy-proven BC was 49.6 years (27-80 years). Three patients were diagnosed with a bilateral BC. Accordingly, the total number of the breasts and axilla evaluated were 94. Based on the histopathological evaluation, it was reported that 46 of all the tumors were invasive ductal carcinoma, four were invasive lobular carcinoma, two were invasive papillary carcinoma, one was malignant phyllodes tumor, one was metaplastic invasive breast carcinoma, one was mixed invasive tumor, and the remaining 39 tumors were reported as moderate or highly invasive breast carcinoma without an identified specific histological characteristic. Extra-axillary metastasis was detected in the 19 (20.8%) patients based on the ^{18}F-FDG PET/CT imaging. The distribution of the metastases was as follows: An internal mammary lymph node metastasis in three patients, mediastinal mass in one patient, supraclavicular lymph node metastasis in three patients, liver metastases in two patients, bone metastases in 11 patients, and lung metastases in two patients, and both the bone and soft tissue metastases in four patients.

The mean size of the primary lesions located in the breast was about 30 mm in the supine position, whereas it was 29 mm in the prone position. There was a significant difference in the diameter of the primary tumor (p=0.029); however, there was no patient whose clinical stage changed because of this. The mean SUV_{max}, SUV_{mean}, MTV, and TLG values for the primary tumor and the axillary lymph nodes in a supine and prone position are summarized in the Table 1. A significant difference was found between the MTV values of the primary tumor measured in two different positions (p=0.037). However, there was no significant difference between the MTV value and SUV_{mean} and TLG values of a

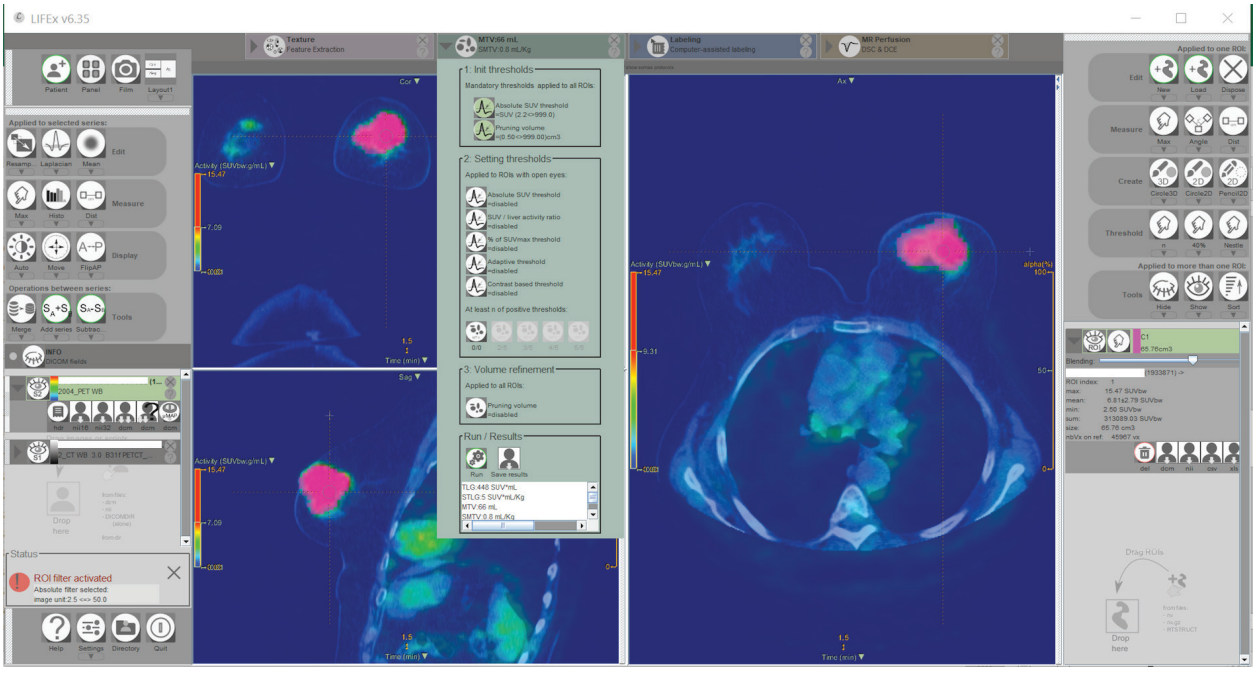

Figure 1. LIFEx software was used to obtain metabolic tumor volume and total lesion glycolysis and SUV average of primary tumor and axillary lymph nodes
SUV: Standardized uptake value

primary tumor and axilla in the both positions.

Primary tumor lesions were grouped based on their distribution like unifocal, multifocal, and multicentric. Accordingly, there was no difference in the tumor localization, and the number between the images acquired in the supine and prone positions. Sixty-three of the tumors were UF, 13 were MF, and 18 were MC.

Lymph nodes with a suspected metastasis on the ^{18}F-FDG PET/CT imaging were classified numerically (1, 2, 3, and multiple). Accordingly, there was no difference in the number of lymph nodes in the 91 axilla (96.8%), except three axillary fossa (3%). One of these patients had four lymph nodes with a suspected metastasis in the supine position, whereas three lymph nodes were observed in the prone images; however, no metastatic lymph node was detected in the axillary dissection performed after the neoadjuvant chemotherapy. Another patient had one lymph node with a suspected metastasis in the supine position and two lymph nodes with a suspected metastasis in the prone position; furthermore, metastasis was detected in three lymph nodes based on the pathological evaluation. The last patient had three lymph nodes in the supine position and one lymph node in the prone position with a suspected metastasis. However, histopathological evaluation did not show any metastatic lymph node.

In the 15 (15.9%) patients, pathological findings in the nipple were identified in at least one of the images in the two different positions. However, in terms of comparison with a histopathological examination, only patients who underwent surgery in their follow-up after PET scan were evaluated. Accordingly, a total of 69 (73%) breast tumors with the available postoperative pathology reports were evaluated in terms of the nipple invasion. Based on this,

Table 1. Primary tumor and axillary lymph node characteristics

		Supine	Prone	p value
Primary tumor	SUV_{max}	8.9±5.1	8.7±5.4	>0.05
	SUV_{mean}	4.3±1.7	4.4±2.1	>0.05
	MTV	24.7±46.8	18.9±42.9	0.037*
	TLG	153.2±439.5	137.3±488.1	>0.05
	Mean diameter (mm)	29.98±14.55	29.04±14.66	0.029*
Axillary lymph node	SUV_{max}	7.3±5.5	7.1±5.4	>0.05
	SUV_{mean}	3.6±1.8	3.5±1.9	>0.05
	MTV	11±18	9.7±15.9	>0.05
	TLG	62±133.2	54.5±122	>0.05

Variables with normal distribution are expressed as mean ± standard deviation. *The significance level is 0.05. SUV_{max}: Maximum standard uptake value, SUV_{mean}: Mean standart uptake value, MTV: Metabolic tumor volume, TLG: Total lesion glycolysis

in the ^{18}F-FDG PET/CT images, nipple involvement was reported as positive in the eight patients in the supine position and in ten patients in the prone position. In the subsequent histopathological evaluation, it was determined that a total of nine patients had the nipple malignancies. Nipple involvement was confirmed histopathologically in six out of eight patients in the supine position and in seven out of ten patients in the prone position. As a result, false positivity was detected in two patients images obtained in the supine position, and in three patients in the prone position. In addition, in two of nine patients with a histopathologically proven nipple involvement, no involvement was observed in either the supine or prone images, and there was a nipple involvement only in the prone position in one patient, but not in the supine position (Figure 2). Thus, the two patients were considered as false negative in both the positions, and one patient was considered false negative only in the supine position. In a patient with the proven nipple involvement and reported involvement in both the positions, the involvement was more pronounced in the image acquired in the prone position. These results are summarized in the Table 2.

Skin involvement of the primary malignancy was detected in 10 of 69 tumors following a surgery. Skin involvement of the primary malignancy was interpreted based on the presence of thickening, irregularity, and increased ^{18}F-FDG uptake in the skin tissue in the ^{18}F-FDG PET/CT examination.

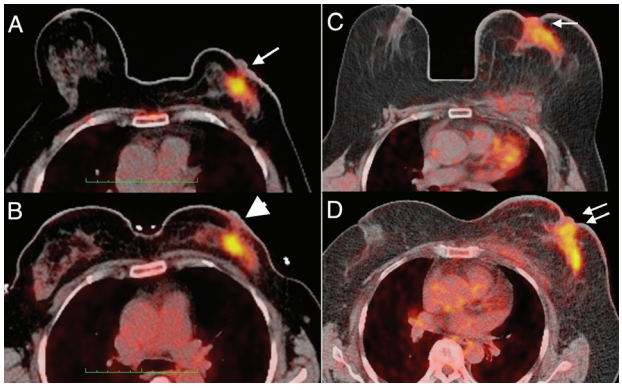

Figure 2. In a 58-year-old patient who underwent ^{18}fluorine-fluorodeoxyglucose positron emission tomography/computed tomography imaging for staging purposes for the diagnosis of unifocal invasive ductal breast carcinoma in the left breast, the nipple retraction in the left breast was more prominent in the prone position (white arrow, A. axial fusion image in prone position) than the images acquired in the supine position (white arrowhead, B. axial fusion image in supine position). However, in another 63-year-old patient, nipple involvement in the left breast was evident in both positions (white arrow, C. axial fusion in prone position and double white arrows, D. axial fusion image in supine position). Malignant tumoral infiltration was detected in the nipple based on the histopathological evaluation performed after surgery in both patients

Accordingly, the skin involvement was identified in the 11 breasts in both positions, and involvement was histopathologically confirmed in seven of them (63%) in both the positions. In addition, suspected skin involvement was identified in the six breasts images obtained in the supine position, whereas skin involvement was ruled out in five of these tumors in the prone position, and only one was considered suspicious, and the skin involvement was confirmed histopathologically in this case (Figure 3). No postoperative involvement was observed in the other five breast tumors with a suspected skin involvement in the supine position. In the two patients whose skin involvement was considered positive in both the positions, the involvement was found to be more pronounced in the prone images. In the two patients with a histopathologically reported skin involvement, no involvement was observed in either of the positions. The patients interpreted as suspicious in terms of the skin involvement in the supine and prone position were also accepted as positive, and the evaluation of the imaging results based on a histopathological data is summarized in the Table 2.

Tumoral invasion signs in the pectoral muscle identified in one patient were not confirmed histopathologically in the ^{18}F-FDG PET/CT images obtained in both the prone and supine positions. In addition, there was suspected tumoral invasion in the two patients in a supine position and in five patients with a prone position, and this involvement was confirmed histopathologically in the two patients classified as suspicious in both the positions. Furthermore, there was no involvement in the images captured in both the positions in two patients whose pectoral muscle invasion was proven after a surgery. Accordingly, results suspected to be positive for pectoral muscle invasion in the supine and prone position were accepted as positive, and the evaluation of the imaging results based on histopathological data is summarized in the Table 2.

When PET/CT fusion images were evaluated in terms of the PET and CT misregistration due to a respiratory or motion artifacts, 12 patients had fusion disagreement only in the prone images and particularly in the axilla, whereas five patients had PET/CT fusion disagreement only in the supine position. Four patients had PET/CT fusion disagreement in both the positions.

There was no significant relationship between the primary tumor SUV_{max}, axillary lymph node SUV_{max}, and primary tumor size values in the supine and prone positions in patients with and without the extra-axillary metastasis,

Table 2. Nipple, skin and pectoral muscle involvement of breast cancer in supine versus prone imaging

		TP	TN	FP	FN	Accuracy (95% CI)	Sensitivity (95% CI)	Specificity (95% CI)	PPV (95% CI)	NPV (95% CI)	PLR (95% CI)	NLR (95% CI)
Nipple invasion	Supine	6	57	2	3	92.6% (83.7-97.6)	66.7% (29.9-92.5)	96.6% (88.3-99.6)	75% (41.6-92.7)	95% (88.3-97.9)	19.7 (4.7-82.9)	0.35 (0.1-0.8)
	Prone	7	56	3	2	92.6% (83.7-97.6)	77.8% (39.9-97.2)	94.9% (85.8-98.9)	70% (42.3-88.1)	965% (89.2-98.9)	15.3 (4.8-48.6)	0.2 (0.1-0.78)
Skin invasion	Supine	8	50	9	2	84% (73.3-91.7)	80% (44.4-97.5)	84.7% (73.0-92.8)	47% (31.1-63.6)	96.1% (87.8-98.8)	5.2 (2.6-10.3)	0.2 (0.1-0.8)
	Prone	8	55	4	2	91.3% (82-96.7)	80% (44.7-97.5)	93.2% (83.5-98.1)	66.7% (42.5-84.4)	96.5% (88.8-98.9)	11.8 (4.3-31.9)	0.2 (0.1-0.7)
Pectoral muscle invasion	Supine	2	62	1	2	95.5% (87.4-93.2)	50% (6.7-93.2)	98.4% (41.4-99.9)	66.6% (18.4-94.6)	96.8% (92.1-98.8)	31.5 (3.5-277.9)	0.51 (0.2-1.4)
	Prone	2	59	4	2	91% (81.5-96.6)	50% (6.7-93.2)	93.6% (84.5-98.2)	33,3% (11.3-66.1)	96,7% (91.7-98.7)	7.8 (2-30.8)	0.5 (0.2-1.42)

CI: Confidence interval, TP: True positive, TN: True negative, FP: False positive, FN: False negative, PPV: Positive predictive value, NPV: Negative predictive value, PLR: Positive likelihood ratio, NLR: Negative likelihood ratio

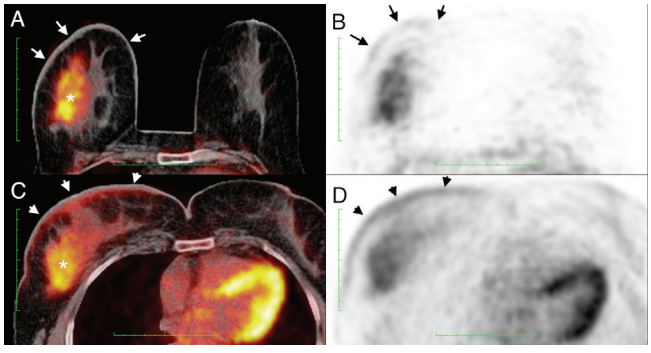

Figure 3. In a 51-year-old female patient with multifocal invasive ductal carcinoma of the right breast, increased thickness with increased ^{18}fluorine-fluorodeoxyglucose uptake in the right breast skin in the supine position (white and black arrowheads, C, D) was decreased in the images taken in the prone position (white and black arrows, A, B). Histopathological examination did not reveal any signs of malignancy in the skin tissue

skin involvement, pectoral muscle invasion, and nipple involvement (p>0.05). The results are summarized in the Table 3.

Based on the correlation analysis between the Ki-67 proliferation index and imaging results, there was a positive correlation between the Ki-67 proliferation index and primary tumor SUV_{max} value in the prone images (p<0.001, r=0.487). However, there was no significant relationship between the primary tumor SUV_{max} value in the supine images. Furthermore, there was a positive correlation between the Ki-67 proliferation index and axillary lymph node SUV_{max} values in both the supine and prone images (p=0.016, r=0.307 vs. p=0.037, r=0.267). There was no significant correlation between the other parameters (Figure 4a, b, c).

Discussion

Khalkhali et al. (10) reported that in technetium-99m scintimammography, imaging in the prone position was a better of a choice than in the supine position because of the differentiation of the deep breast structures in the left breast from the myocardium, and the right breast from the liver and the relaxation of the pectoral muscles. Subsequently, Yutani et al. (11) reported higher SUV_{max} values in the cancerous tissue in the PET imaging performed in the prone position. In the subsequent years, a relatively limited number of the studies showed that additional imaging in the prone position provides more diagnostic information than the images acquired in the supine position (5,6,7).

When axillary lymph nodes were evaluated in the ^{18}F-FDG PET/CT imaging in both the supine and prone positions, there was no difference in the number of the pathological lymph nodes in majority of the patients (96.8%). However, it was predicted that the three lymph nodes with a suspected metastasis in the supine images in three patients may be benign based on the prone imaging, which was subsequently confirmed by the histopathological evaluation, and no metastasis was detected in these lymph nodes. As prone imaging was performed in the late phase rather than immediately after the complete body imaging in these patients, it was believed that the increased ^{18}F-FDG accumulation over a time in the malignant tissue and decreased ^{18}F-FDG accumulation over a time in the benign tissue may have had this dual-phase effect (12). However, Sasada et al. (13) determined that the standard and late SUV_{max} values were equivalent in terms of the diagnostic accuracy in detecting the axillary lymph node metastasis. In addition, Abramson et al. (5) reported that the supine

Table 3. Comparison of SUV_{max} and axial diameter of primary tumor, and SUV_{max} of axillary lymph node measurements derived from supine and prone images with histopathological local involvement results

	Primary tumor SUV_{max}		Axillary lymph node SUV_{max}		Primary tumor size (mm)		
	Supine	**Prone**	**Supine**	**Prone**	**Supine**	**Prone**	
M-no	6.8 (2.3-19.8)	6.7 (1.6-17.2)	9.5 (3-12.6)	10 (1.7-13.7)	20 (13-47)	20 (15-50)	
M-yes	7.7 (3.5-103)	7.6 (2.4-17)	5.9 (1.3-27.4)	6.1 (0.0-28)	28 (8-48)	28 (8-46)	
S-no	7 (1.6-22)	6.8 (1-21.4)	6 (1.3-27.4)	5.75 (1-28)	27 (8-73)	25 (3.5-73)	
S-yes	6.9 (3.6-13.5)	6.2 (3.4-18.2)	6.2 (1.3-17)	5.4 (0-17.8)	30 (16-49)	29.5 (15-49)	p>0.05
P-no	7 (1.6-22)	6.8 (1-21.4)	6.7 (1.3-27.4)	6.2 (1-28)	27 (8-73)	25 (3.5-73)	
P-yes	6.7 (4.8-13.5)	5.8 (5.1-18.2)	2.5 (1.3-6.4)	2.55 (0-9.0)	36 (18-61)	38.5 (15-52)	
N-no	7 (1.6-22)	6.8 (1-21.4)	6.7 (1.3-27.4)	6.2 (1-28)	23 (3.5-73)	23 (3.5-73)	
N-yes	6.7 (3.6-13.5)	5.8 (3.4-18.2)	3.3 (1.3-17)	3.2 (0-17.8)	37 (15-52)	37 (15-52)	

Variables without normal distribution are expressed as median (minimum-maximum). SUV_{max}: Maximum standart uptake value, M-no: Group without metastasis, M-yes: Group with metastasis, S-no: Group without skin involvement, S-yes: Group with skin involvement, P-no: Group without pectoral muscle involvement, P-yes: Group with pectoral muscle involvement, N-no: Group without nipple involvement, N-yes: Group with nipple involvement

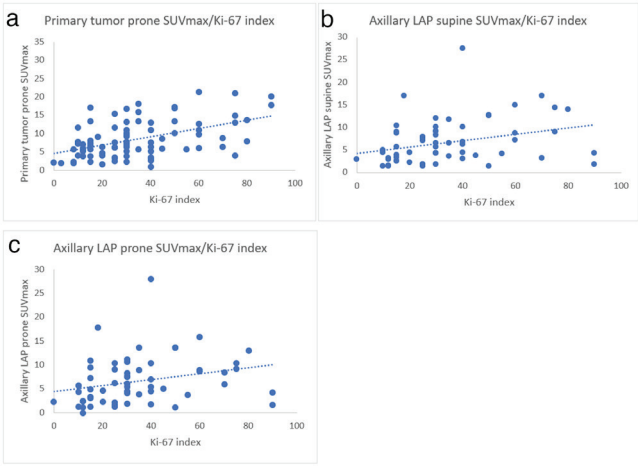

Figure 4. A. Primary tumor SUV_{max} value and Ki-67 proliferation index in the prone position. B. Axillary lymph node SUV_{max} value and Ki-67 proliferation index in the supine position. C. Axillary lymph node SUV_{max} value and Ki-67 proliferation index in the prone position
SUV_{max}: Maximum standardized uptake value

and prone imaging was performed consecutively (the dual-phase effect was negligible) in the evaluation of the axillary lymph nodes and that a higher number of positive lymph nodes was detected in four out of 16 patients in prone imaging. In addition, another study in which the imaging was performed in the prone position followed by the imaging in the supine position reported that a higher number of axillary lymph nodes were detected in the prone position (6).

In the comparison of primary tumor and axillary lymph node SUV_{max} values between the images obtained in the supine and prone positions, in the axillary lymph nodes, there was no significant difference in the SUV_{max} values between the images in the supine position and those in the prone position, whereas primary tumor SUV_{max} values were higher in the supine position than in the prone position. Although the reason for this is not precisely known, it was believed that it may have occurred due to the misregistration artifact or the partial volume effect. Partial volume is particularly affected by how compact the tumor is, as well as the size and shape of the tumor. Measurement results of the SUV_{max} may be higher in the less compact tumors as the tumor tissues in the prone position tend to extend to the edges (14,15). In a retrospective study of the 100 patients designed by Lee et al. (16), they performed prone imaging immediately after a supine position imaging and found higher SUV_{max} values in the supine position, consistent with those obtained in our study. In the same study, the authors also found a higher MTV and the TLG values on images in the supine position (16). In addition, it was presented in our study that there was a significant difference in the images taken in different positions in primary tumor diameters (p=0.029). In this study, in which measurements were made in the axial sections as a standard, it was believed that the reason for the lower tumor diameter in the prone position compared in the supine position was primarily because of the change in the configuration of the tumor. It was believed that the wider spread of the breast parenchyma in the prone position, the tumor mass may have expanded toward the inferior segment, and thus the measurement of its largest diameter may have been lower. In addition, there is a possibility that the tumor diameter may have been measured slightly larger in the supine position because of the surrounding normal breast parenchyma is in a more tightened position in the supine position, especially in the mass lesions with low-moderate ^{18}F-FDG metabolism, which may be one of the reasons why

the mean tumor diameter is higher in the supine imaging. Teixeira et al. (6) reported a larger primary tumor volume in a supine imaging, whereas Moon et al. (17) compared the supine ^{18}F-FDG PET/CT with the PET/CT mammography (mammo-PET/CT) in their study and found larger primary tumor size in the mammo-PET/CT in the prone position.

Various studies have shown that the MTV and TLG have a prognostic value in patients with a BC (18,19). In our study, MTV and TLG were also higher in the supine position. Similarly, Arslan et al. (20) found that the tumor size correlated with MTV and TLG. The authors found similar results for the axillary lymph nodes in this study having 139 patients (20). We found the metabolic parameters (SUV_{max}, TLG, MTV) compatible in both the primary tumor and the axilla. All the parameters were numerically higher in the supine position than in the prone position. However, only a significant difference was found in the MTV. Like our study, Lee et al. (16) found that SUV_{max}, MTV, and TLG values were lower in the prone position than in the supine position. They reported that the reason for this may be the partial volume effect. Therefore, they stated that the acquisition position may affect the quantitative PET/CT parameters and the clinical outcomes.

There was no difference between the diagnostic accuracy of both the positions in terms of nipple involvement (92.6%), and sensitivity was higher in the prone images compared with those obtained in the supine position (77.8% and 66.7%, respectively); however, the specificity was slightly higher in the supine images compared with those obtained in the prone position (96.6% and 94.9%, respectively). Positive predictive value for the nipple involvement was higher in the supine images compared with those acquired in the prone position (75% and 70%, respectively), whereas the negative predictive value was slightly higher in the prone images (96.5% and 95%, respectively) compared with those acquired in the supine position. The study by Yoo et al. (21) investigated the importance of the dual-phase prone PET images in terms of nipple-areolar complex involvement in the 21 patients and confirmed that the presence of an increase in the nipple SUV_{max} values in the late phase compared with those in the contralateral breast was an independent variable in terms of the nipple involvement. Although the study design and evaluation criteria were different, we believe that the late prone images were also useful in our study.

Because prone imaging was performed in the late phase, the ^{18}F-FDG uptake in the skin tissue decreased as increasing ^{18}F-FDG uptake in the primary tumor, which facilitated the determination of the patients as negative in terms of the skin involvement. We believed that the ^{18}F-FDG intensity in the skin tissue in a supine position developed secondary to inflammation and that combined evaluation of the images acquired in both the positions and especially dual-phase imaging may be useful. Accordingly, the sensitivity of the supine imaging in terms of a skin involvement was the same as that for the prone imaging (80%), whereas specificity (84.7% and 93.2%, respectively), accuracy (84% and 91.3%, respectively), and the positive predictive value (47.1% and 66.7%, respectively) were lower than those for a prone imaging. The negative predictive value was nearly the same (96%) in both positions. Although the studies have been performed using ^{18}F-FDG PET/CT, and cases showing that the skin involvement affects the prognosis negatively in the literature (22,23) are also available, we could not find a publication that compares the prone and supine images on this subject.

In ^{18}F-FDG PET/CT images acquired in the supine and prone position, one patient had an evidence of tumoral invasion in the pectoral muscle, but it was not confirmed histopathologically. This involvement was also identified in the MRI performed before the treatment, and it was believed that the involvement may not have been detected histopathologically caused by a neoadjuvant chemotherapy performed after the PET/CT scan. In addition, two patients had suspected an involvement in the supine position, and five patients had suspected an involvement in the prone position; involvement was histopathologically confirmed in two patients classified as suspicious in both the positions. In the other three patients who were suspected to be positive only in the prone position and whose histopathological evaluation did not show any signs of a pectoral muscle involvement, only the prone images showed an area of increased density between the malignant mass lesion and the pectoral muscle without the pathological ^{18}F-FDG uptake. This finding was also described in the MRI of the patients who was suspected to have a pectoral muscle invasion. Moreover, all the three patients had multiple fibrocystic structures. The area of increase in density in the prone images was believed to be associated with the fibrocystic-fibro glandular structures described in the last MRI. No involvement was observed in the images acquired in both the positions in two patients with a pectoral muscle invasion after the surgery. Because the breast tissue was very small in one of the patients, muscle invasion could not be differentiated in the images, and prone imaging thus did not enlighten to the differentiation of the tissues. In the other patient, there was no pathological finding in the pectoral muscle tissue, and its vicinity in either of the positions. Accordingly, the accuracy of the supine imaging in predicting the pectoral muscle involvement was slightly higher than that of a prone imaging (95.5% and 91%,

respectively), its sensitivity was equal (50%), its specificity was slightly higher than that of a prone imaging (98.4% and 93.6%, respectively), its positive predictive value was significantly higher than that of a prone imaging (66.7% and 33.3%, respectively), and its negative predictive value was nearly equal (96%). Considering that the pectoral muscle involvement does not change the tumor stage, it is believed that it affects the reporting, although it has no clinical significance. While there are studies in the literature regarding the distance of the primary tumor from the pectoral muscle, we were not able to identify a comparative study on a pectoral muscle invasion of the prone and supine imaging in the English literature.

When PET/CT fusion images were evaluated for PET and CT agreement, 12 patients had fusion disagreement only in the prone images especially in the axilla, whereas five patients had it only in the supine position. Four patients had disagreement in both the positions. Although it is known that the imaging in the prone position generally reduces a respiration and movement artifact due to the pressure applied on the chest compared to the supine position (7), in our study, it was suspected that the fusion disagreement in a prone position may be due to less patient comfort in the prone position which results in the higher number of the movement artifacts. It was believed that the arm movement could particularly be the main reason for the incompatibility observed in the axillary lymph nodes in the prone position. In their study on the 198 patients diagnosed with stage II/III BC, Teixeira et al. (6) found a higher disagreement rate in the PET and CT scans in the images acquired in a supine position. This may be due to that the comfort level of the breast positioning device used in a prone position was higher than that of the apparatus used in our study, and/or they performed prone imaging first and then whole-body supine imaging was done. Thus, it may be suggested that the patient compliance is better in the first imaging.

There was no significant relationship between the primary tumor SUV_{max}, axillary lymph node $SUV_{max,}$ and primary tumor size values in the supine and prone position in patients with and without the extra-axillary bone and soft tissue metastasis and patients with and without a skin involvement, pectoral muscle invasion and the nipple involvement ($p>0.05$). Primary tumor diameter was higher in both positions in the group with a skin involvement, pectoral muscle invasion, and the nipple involvement, whereas a primary tumor and axillary lymph node SUV_{max} values were lower. In addition, the primary tumor SUV_{max} and primary tumor diameter were higher in the group with an extra-axillary metastasis, while the average SUV_{max} in the axillary lymph nodes was lower.

When PET/CT fusion images are evaluated in terms of the PET and CT compatibility, In 12 patients, only prone images and especially axilla fusion mismatch was detected, whereas in five patients only the PET/CT fusion mismatch was observed in the supine position. In four patients, an incompatibility was observed in both the positions.

In the correlation analysis between the Ki-67 proliferation index determined in the histopathological examination performed after a surgery and the imaging results, there was a positive correlation between the Ki-67 proliferation index and a primary tumor SUV_{max} value in the prone images ($p<0.001$, $r=0.487$). However, there was no significant relationship between the Ki-67 proliferation index and a primary tumor SUV_{max} value in the supine images. Furthermore, there was a positive correlation between the Ki-67 proliferation index and axillary lymph node SUV_{max} values in both the images taken in the supine and prone positions ($p=0.016$, $r=0.307$ and $p=0.037$, $r=0.267$, respectively). There was no significant correlation between the other parameters.

Study Limitations

The following were the limitations in our retrospective analysis: (1) The imaging time between the positions was not standardized, (2) the results were likely affected by the dual-phase imaging procedure because prone imaging was done in the late phase in most of the patients, (3) the histopathological data did not have the desired standard because the neoadjuvant chemotherapy protocol was used in most of the patients, and (4) the number of the patients were relatively limited.

Conclusion

Although there are studies which recommend that an additional imaging in the prone position should be included in the evaluation of BC, the advantage of a prone breast PET/CT imaging over the standard supine whole-body imaging has not been clearly determined. The purpose of our study was to make this comparison; however, our result did not indicate any of the imaging positions was significantly more advantageous, and we think that an additional imaging in a prone position may be useful in the selected cases such as, suspicious skin involvement, in the evaluation of a local disease in patients with a BC. In addition, it should be kept in mind that it may change the metabolic and morphological numerical results in images obtained in the different positions.

Ethics

Ethics Committee Approval: Ethical permission for the study was given by the Ethics Committee of Bezmialem

Vakif University Faculty of Medicine with a letter dated 16 April, 2019, numbered 08/131.

Informed Consent: Informed consent was waived.

Peer-review: Externally peer-reviewed.

Authorship Contributions

Concept: E.B.E., M.A., Design: E.B.E., M.A., Data Collection or Processing: E.B.E., M.A., Analysis or Interpretation: E.B.E., M.A., Literature Search: E.B.E., M.A., Writing: E.B.E., M.A.

Conflict of Interest: No conflict of interest was declared by the authors.

Financial Disclosure: The authors declared that this study has received no financial support.

References

1. Reddy Akepati NK, Abubakar ZA, Bikkina P. Role of 18F-fluorodeoxyglucose positron-emission tomography/computed tomography scan in primary staging of breast cancer compared to conventional staging. Indian J Nucl Med 2018;33:190-193.
2. Paydary K, Seraj SM, Zadeh MZ, Emamzadehfard S, Shamchi SP, Gholami S, Werner TJ, Alavi A. The evolving role of FDG-PET/CT in the diagnosis, staging, and treatment of breast cancer. Mol Imaging Biol 2019;21:1-10.
3. Moy L, Ponzo F, Noz ME, Maguire GQ Jr, Murphy-Walcott AD, Deans AE, Kitazono MT, Travascio L, Kramer EL. Improving specificity of breast MRI using prone PET and fused MRI and PET 3D volume datasets. J Nucl Med 2007;48:528-537.
4. Bitencourt AG, Lima EN, Chojniak R, Marques EF, Souza JA, Andrade WP, Guimarães MD. Can 18F-FDG PET improve the evaluation of suspicious breast lesions on MRI? Eur J Radiol 2014;83:1381-1386.
5. Abramson RG, Lambert KF, Jones-Jackson LB, Arlinghaus LR, Williams J, Abramson VG, Chakravarthy AB, Yankeelov TE. Prone versus supine breast FDG-PET/CT for assessing locoregional disease distribution in locally advanced breast cancer. Acad Radiol 2015;22:853-859.
6. Teixeira SC, Koolen BB, Vogel WV, Wesseling J, Stokkel MP, Vrancken Peeters MJ, van der Noort V, Rutgers EJ, Valdés Olmos RA. Additional prone 18F-FDG PET/CT acquisition to improve the visualization of the primary tumor and regional lymph node metastases in stage II/III breast cancer. Clin Nucl Med 2016;41:e181-186.
7. Kaida H, Ishibashi M, Fuji T, Kurata S, Uchida M, Baba K, Miyagawa T, Kaibara H, Kawamura S, Ogo E, Hayabuchi N. Improved breast cancer detection of prone breast fluorodeoxyglucose-PET in 118 patients. Nucl Med Commun 2008;29:885-893.
8. Cho IH, Kong EJ. Potential clinical applications of 18F-fluorodeoxyglucose positron emission tomography/magnetic resonance mammography in breast cancer. Nucl Med Mol Imaging 2017;51:217-226.
9. Nioche C, Orlhac F, Boughdad S, Reuzé S, Goya-Outi J, Robert C, Pellot-Barakat C, Soussan M, Frouin F, Buvat I. LIFEx: A freeware for radiomic feature calculation in multimodality imaging to accelerate advances in the characterization of tumor heterogeneity. Cancer Res 2018;78:4786-4789.
10. Khalkhali I, Mena I, Diggles L. Review of imaging techniques for the diagnosis of breast cancer: a new role of prone scintimammography using technetium-99m sestamibi. Eur J Nucl Med 1994;21:357-362.
11. Yutani K, Tatsumi M, Uehara T, Nishimura T. Effect of patients' being prone during FDG PET for the diagnosis of breast cancer. AJR Am J Roentgenol 1999;173:1337-1339.
12. Caprio MG, Cangiano A, Imbriaco M, Soscia F, Di Martino G, Farina A, Avitabile G, Pace L, Forestieri P, Salvatore M. Dual-time-point [18F]-FDG PET/CT in the diagnostic evaluation of suspicious breast lesions. Radiol Med 2010;115:215-224.
13. Sasada S, Masumoto N, Kimura Y, Kajitani K, Emi A, Kadoya T, Okada M. Identification of axillary lymph node metastasis in patients with breast cancer using dual-phase FDG PET/CT. AJR Am J Roentgenol 2019;213:1129-1135.
14. Vidal-Sicart S, Aukema TS, Vogel WV, Hoefnagel CA, Valdés-Olmos RA. Valor añadido de la técnica en decúbito prono para el estudio con tomografía por emisión de positrones-tomografía computarizada en las pacientes con cáncer de mama [Added value of prone position technique for PET-TAC in breast cancer patients]. Rev Esp Med Nucl 2010;29:230-235.
15. Soret M, Bacharach SL, Buvat I. Partial-volume effect in PET tumor imaging. J Nucl Med 2007;48:932-945.
16. Lee JH, Jeon TJ, Ahn SG, Jeong J, Seok JW, Ryu YH. Variations in (18) F-FDG uptake in breast cancer depending on PET/CT acquisition position. Clin Radiol 2016;71:86-91.
17. Moon EH, Lim ST, Han YH, Jeong YJ, Kang YH, Jeong HJ, Sohn MH. The usefulness of F-18 FDG PET/CT-mammography for preoperative staging of breast cancer: comparison with conventional PET/CT and MR-mammography. Radiol Oncol 2013;47:390-397.
18. Pak K, Seok JW, Kim HY, Nguyen TL, Kim K, Kim SJ, Kim IJ, Hopper J. Prognostic value of metabolic tumor volume and total lesion glycolysis in breast cancer: a meta-analysis. Nucl Med Commun 2020;41:824-829.
19. Jiménez-Ballvé A, García García-Esquinas M, Salsidua-Arroyo O, Serrano-Palacio A, García-Sáenz JA, Ortega Candil A, Fuentes Ferrer ME, Rodríguez Rey C, Román-Santamaría JM, Moreno F, Carreras-Delgado JL. Prognostic value of metabolic tumour volume and total lesion glycolysis in 18F-FDG PET/CT scans in locally advanced breast cancer staging. Rev Esp Med Nucl Imagen Mol 2016;35:365-372.
20. Arslan E, Can Trabulus D, Mermut Ö, Şavlı TC, Çermik TF. Alternative volumetric PET pjmirometers for evaluation of breast cancer cases with 18F-FDG PET/CT imaging: metabolic tumour volume and total lesion glycolysis. J Med Imaging Radiat Oncol 2021;65:38-45.
21. Yoo J, Kim BS, Chung J, Yoon HJ. Clinical value of delayed 18F-FDG PET/CT for predicting nipple-areolar complex involvement in breast cancer: a comparison with clinical symptoms and breast MRI. PLoS One 2018;13:e0203649.
22. Young CR, Harigopal M, Pucar D. Rapid progression of carcinoma en cuirasse breast dermal metastases on 18F-fludeoxyglucose positron emission tomography-computed tomography. World J Nucl Med 2019;19:65-68.
23. Dave SR, Samuel TA, Pucar D, Savage N, Williams HT. FDG PET/CT in evaluation of unusual cutaneous manifestations of breast cancer. Clin Nucl Med 2015;40:e63-e67.

Original Article
Mol Imaging Radionucl Ther 2022;31:33-41 DOI:10.4274/mirt.galenos.2021.79037

The Role of Histogram-Based Textural Analysis of ^{18}F-FDG PET/CT in Evaluating Tumor Heterogeneity and Predicting the Prognosis of Invasive Lung Adenocarcinoma

İnvaziv Akciğer Adenokarsinomunda ^{18}F-FDG PET/CT Histograma Dayalı Doku Analizinin Tümör Heterojenitesinin Değerlendirilmesinde ve Prognoz Tayininde Rolü

Hasan Önner[1], Nazım Coşkun[2], Mustafa Erol[1], Meryem İlkay Eren Karanis[3]

[1]*University of Health Sciences Turkey, Konya City Hospital, Clinic of Nuclear Medicine, Konya, Turkey*
[2]*University of Health Sciences Turkey, Ankara City Hospital, Clinic of Nuclear Medicine, Ankara, Turkey*
[3]*University of Health Sciences Turkey, Konya City Hospital, Clinic of Pathology, Konya, Turkey*

Abstract

Objectives: This study aimed to investigate the contributory role of histogram-based textural features (HBTFs) extracted from ^{18}fluorine-fluorodeoxyglucose (^{18}F-FDG) positron emission tomography/computed tomography (PET/CT) in tumoral heterogeneity (TH) evaluation and invasive lung adenocarcinoma (ILA) prognosis prediction.

Methods: This retrospective study analyzed the data of 72 patients with ILA who underwent ^{18}F-FDG PET/CT followed by surgical resection. The maximum standardized uptake value (SUV_{max}), metabolic tumor volume, and total lesion glycolysis values were calculated for each tumor. Additionally, HBTFs were extracted from ^{18}F-FDG PET/CT images using the software program. ILA was classified into the following five histopathological subtypes according to the predominant pattern: Lepidic adenocarcinoma (LA), acinar adenocarcinoma, papillary adenocarcinoma, solid adenocarcinoma (SA), and micropapillary adenocarcinoma (MA). Differences between ^{18}F-FDG PET/CT parameters and histopathological subtypes were evaluated using non-parametric tests. The study endpoints include overall survival (OS) and progression-free survival (PFS). The prognostic values of clinicopathological factors and ^{18}F-FDG PET/CT parameters were evaluated using the Cox regression analyses.

Results: The median SUV_{max} and entropy values were significantly higher in SA-MA, whereas lower in LA. The median energy-uniformity value of the LA was significantly higher than the others. Among all parameters, only skewness and kurtosis were significantly associated with lymph node involvement status. The median values for follow-up time, PFS, and OS were 31.26, 16.07, and 20.87 months, respectively. The univariate Cox regression analysis showed that lymph node involvement was the only significant predictor for PFS. The multivariate Cox regression analysis revealed that higher SUV_{max} (≥11.69) and advanced stage (IIB-IIIA) were significantly associated with poorer OS [hazard ratio (HR): 3.580, p=0.024 and HR: 7.608, p=0.007, respectively].

Conclusion: HBTFs were tightly associated with clinicopathological factors causing TH. Among the ^{18}F-FDG PET/CT parameters, only skewness and kurtosis were associated with lymph node involvement, whereas SUV_{max} was the only independent predictor of OS. TH measurement with HBTFs may contribute to conventional metabolic parameters in guiding precision medicine for ILA.

Keywords: Lung adenocarcinoma, prognosis, fluorodeoxyglucose, textural analysis, radiomics

Öz

Amaç: Bu çalışmada, invaziv akciğer adenokarsinomunda (IAA) ^{18}flor-florodeoksiglukoz (^{18}F-FDG) pozitron emisyon tomografisi/bilgisayarlı tomografiden (PET/BT) elde edilen histogram tabanlı doku özelliklerinin (HTDÖ) tümör heterojenitesini (TH) ve prognozu değerlendirmedeki katkı rolü araştırılmıştır.

Address for Correspondence: Hasan Önner MD, University of Health Sciences Turkey, Konya City Hospital, Clinic of Nuclear Medicine, Konya, Turkey
Phone: +90 537 540 10 92 **E-mail:** hasanonner@gmail.com ORCID ID: orcid.org/0000-0003-1002-2097
Received: 13.06.2021 **Accepted:** 26.09.2021

Yöntem: Cerrahi tedavi öncesi ^{18}F-FDG PET/BT tetkiki uygulanan ve primer tümörü rezeke edilen 72 IAA'lı hastanın verileri geriye dönük olarak incelendi. Her primer tümör için maksimum standardize alım değeri (SUV_{maks}), metabolik tümör hacmi ve toplam lezyon glikoliz değerleri hesaplandı. Ayırca yazılım programı kullanılarak HTDÖ'ler edildi. IAA, baskın histopatolojik alttipe göre beş gruba ayrıldı: Lepidik adenokarsinom (LA), asiner adenokarsinom, papiller adenokarsinom, solid adenokarsinom (SA) ve mikropapiller adenokarsinom (MA). ^{18}F-FDG PET/BT parametreleri ve histopatolojik alt tipler arasındaki farklılıklar non-parametrik testler ile değerlendirildi. Çalışma sonlanım noktaları genel sağkalım (SK) ve progresyonsuz sağkalım (PSK) idi. Klinikopatolojik faktörlerin ve ^{18}F-FDG PET/BT parametrelerinin prognostik değerleri Cox regresyon analizi ile değerlendirildi.

Bulgular: Medyan SUV_{maks} ve medyan entropy değerleri SA-MA'da anlamlı olarak yüksek, LA'da daha düşük olarak bulundu. LA'nın medyan energy-uniformity değeri diğerlerinden anlamlı derecede yüksekti. Tüm parametreler arasında sadece skewness ve kurtosis, lenf nodu tutulumu durumu ile anlamlı olarak ilişkiliydi. Takip süresi, PSK ve SK için medyan değerler sırasıyla; 31,26, 16,07 ve 20,87 aydı. Tek değişkenli Cox regresyon analizi, lenf nodu tutulumunun PSK için tek anlamlı öngörücü olduğunu gösterdi. Çok değişkenli Cox regresyon analizi, yüksek SUV_{maks} (≥11,69) ve ileri evrenin (IIB-IIIA) daha kötü SK ile anlamlı şekilde ilişkili olduğunu ortaya koydu [sırasıyla; hazard ratio (HR): 3,580, p=0,024 ve HR: 7,608, p=0,007].

Sonuç: HDTÖ'ler, TH'ye neden olan klinikopatolojik faktörlerle yakından ilişkiydi. ^{18}F-FDG PET/BT parametrelerinden sadece skewness ve kurtosis lenf nodu tutulumu ile ilişkiliydi. SUV_{maks}, OS'nin bağımsız öngörücüsü olan tek ^{18}F-FDG PET/BT parametresiydi. TH'nin HBTF'lerle ölçümü, ILA için hassas tıbbın yönlendirilmesinde geleneksel metabolik parametrelere katkıda bulunabilir.

Anahtar kelimeler: Akciğer adenokarsinomu, prognoz, florodeoksiglukoz, doku analizi, radyomiks

Introduction

Lung cancer is the leading cause of cancer deaths worldwide (1). Surgical resection is a radical treatment for early-stage non-small cell lung cancer (NSCLC); however, ~40-60% of patients with early-stage NSCLC die within 5 years following curative resection. Approximately 85% of lung cancer consists of invasive lung adenocarcinoma (ILA), which is the most common histopathological subtype among NSCLC and has a poor prognosis (2). ILA consist of mixed patterns and exhibit highly heterogeneous behavior. The current histopathological classification of ILA fails to meet the advances in imaging, pathology, and tumor molecular biology (3). Additionally, this classification was inefficient for precision medicine development and prognosis prediction. Therefore, in the new classification, ILA is divided into the following five histopathological subtypes based on the dominant pattern: Lepidic adenocarcinoma (LA), acinar adenocarcinoma (AA), papillary adenocarcinoma (PA), solid adenocarcinoma (SA), and micropapillary adenocarcinoma (MA) (3).

Tumor heterogeneity (TH) is one of the important factors that affect treatment response (4). TH, as assessed by ^{18}fluorine-fluorodeoxyglucose (^{18}F-FDG) positron emission tomography/computed tomography (PET/CT), reflects intra-tumoral variabilities, such as cellularity, proliferation, and necrosis (5). Texture analysis is a set of quantitative parameters that reflect TH using computational processing techniques (6). This analysis shows that heterogeneity is quantitated in all tumor areas in ^{18}F-FDG uptake. With textural analysis, lots of studies have been conducted in various areas, such as benign-malignant distinction (7,8), tumor subtype differentiation (9), treatment response evaluation (10,11), and prognosis prediction (12,13).

Several studies have evaluated the association of histopathological patterns of ILA with conventional ^{18}F-FDG PET/CT parameters, such as maximum standardized uptake value (SUV_{max}), metabolic tumor volume (MTV), and total lesion glycolysis (TLG) (14,15,16). However, studies that investigated the relationship between histopathological patterns of resected ILA and histogram-based textural features (HBTFs) extracted from ^{18}F-FDG PET/CT are scarce.

Therefore, this study evaluated ^{18}F-FDG PET/CT parameters along with HBTFs to evaluate TH and identify independent predictors of progression-free survival (PFS) and overall survival (OS) of ILA. In light of our findings, different postoperative adjuvant treatments for precision medicine can be applied to patients with poor prognostic data.

Materials and Methods

Patients

The Local Ethics Committee of KTO Karatay University Faculty of Medicine approved this study under the decision number: 2021/010, number: E-41901325-050.99-2306. Patients who underwent an ^{18}F-FDG PET/CT scan before surgical resection with a diagnosis of ILA between August 2012 and September 2019 in our hospital were included in this study. Exclusion criteria were 1) neoadjuvant therapy before surgery, 2) tumor size of <10 mm (to eliminate partial volume effect on PET), (3) tumors with the SUV_{max} lower than the determined MTV threshold of 2.5, 4) mucinous lung adenocarcinoma, and 5) inappropriate condition for ^{18}F-FDG PET/CT (fasting blood glucose of >150 mg/dL). The flowchart of patient selection is shown in Figure 1.

Clinicopathological data included age, sex, histopathological subtypes, tumor diameter, lymph node metastasis status, stage, and ^{18}F-FDG PET/CT parameters. The tumor diameter,

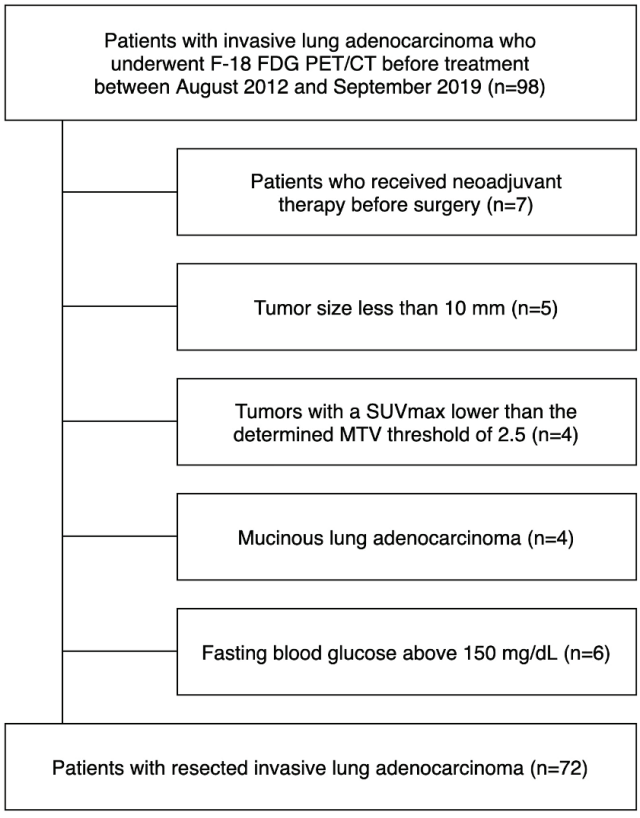

Figure 1. The flowchart of patient selection
^{18}F-FDG: ^{18}Fluorine-fluorodeoxyglucose, PET/CT: Positron emission tomography/computed tomography

nodal involvement, and metastasis (TNM) stage are based on the 8th edition of the American Joint Committee on Cancer TNM classification for lung cancer (17). The following five histopathological subtypes of ILA were determined according to the predominant pattern: LA, AA, PA, SA, and MA. Only two patients had MA patterns, thus they were merged under the SA-MA group, as both solid and micropapillary patterns are considered high-grade.

After the primary tumor resection, all patients underwent regular clinical follow-up, including physical examination and CT or scans every 3-6 months. In cases of abnormal findings on these follow-up examinations, additional imaging studies, including contrast-enhanced CT and ^{18}F-FDG PET/CT scans were performed to verify local, regional, or distant relapse. Therefore, PFS was defined as the time between the dates of pre-operative ^{18}F-FDG PET/CT scan and the date of relapse in patients with relapsed, whereas the time between the date of the ^{18}F-FDG PET/CT scan and the last visit to the hospital for ILA in patients with non-relapsed. The onset for OS was the date of the pre-operative ^{18}F-FDG PET/CT scan. Patient relatives were called by telephone. The telephone follow-up date for the survivors and the date of death for the non-survivors were considered the OS endpoint.

Imaging

Patients fasted for 6-8 hours, and ^{18}F-FDG (3.7 MBq/kg) was intravenously injected when their fasting blood glucose was <150 mg/dL. Patients were rested for 60 min after the injection and underwent PET/CT (Biograph LSO-16 PET/CT scanner, Siemens Medical Solutions, Chicago, IL) scan using ^{18}F-FDG. The scan was done from the base of the skull to the upper part of the thigh. CT scan parameters were 120 kV, 140 mAs, and slice thickness of 5 mm. PET acquisition method was 3 min/bed. Images were generated using the reconstruction method with PET and CT. PET/CT fusion images were obtained and transferred to the workstation.

Image Analysis

An experienced nuclear medicine physician has visually and semi-quantitatively analyzed ^{18}F-FDG PET/CT images. A region of interest (ROI) was drawn around the tumor to calculate SUV_{max} and mean SUV (SUV_{mean}) values. A volume of interest with an SUV threshold of 2.5 was used to determine the MTV using the software program (TRUE D, Siemens Medical Solutions). TLG was obtained by multiplying the MTV by the SUV_{mean}.

Textural Analysis

The ^{18}F-FDG PET images were evaluated by LIFEx v6.30 software, a semi-automatic program for three-dimensional histogram-based textural analysis (18). Figure 2 shows the extraction of tumor HBTFs from ^{18}F-FDG PET images. The SUV_{max} threshold of 2.5 was used for tumor segmentation, and the reproducibility of extracted TFs using this value was better compared to other threshold values (19). The TFs obtained from the primary tumor consisted of HBTFs (skewness, kurtosis, energy-uniformity, and entropy). Second- and higher-level TFs were extracted from lesions larger than 64 voxels. However, these parameters were not evaluated as a significant amount of tumors (30/72) in the study population below this level.

Statistical Analysis

Study variables were analyzed using Statistical Package for the Social Sciences v26 (IBM Corporation, Armonk, NY, USA). The data were not homogeneously distributed. Therefore, the data were expressed as medians. The Mann-Whitney U test was used for comparisons between paired groups, whereas the Kruskal-Wallis test was for multiple group comparisons. Significance values have been adjusted by the Bonferroni correction for multiple tests.

A Cox regression model including parameters with p values of <0.05 in the univariate analysis was used to

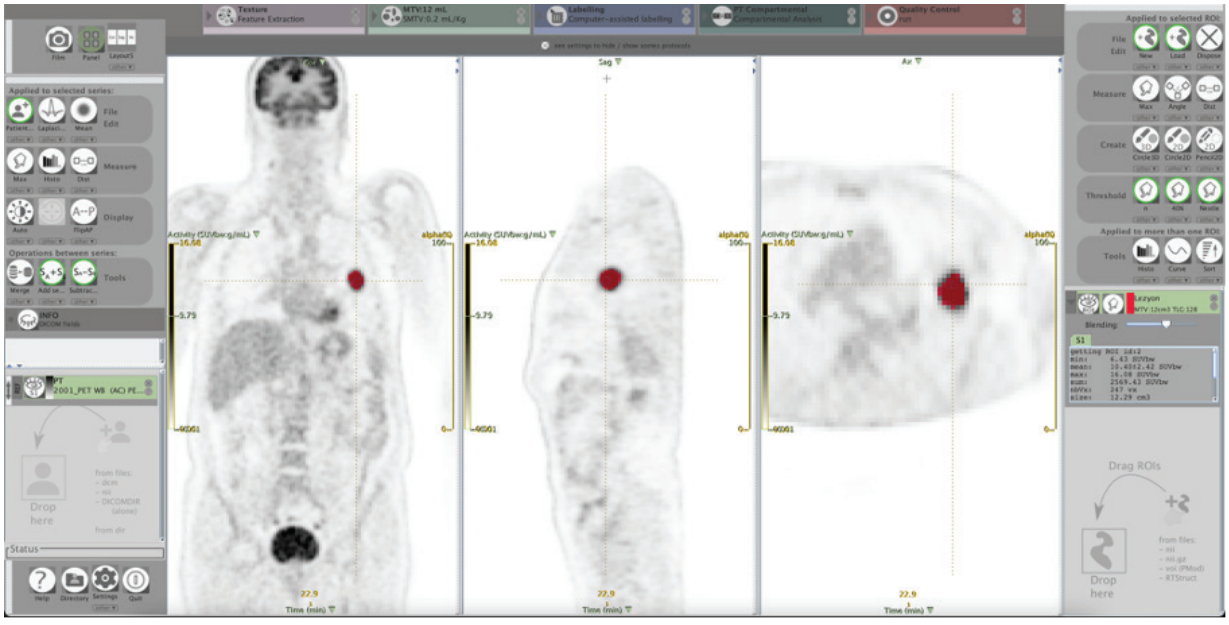

Figure 2. Demonstration of tumor HBTF extraction from ^{18}F-FDG PET image
HBTF: Histogram-based textural feature, ^{18}F-FDG: ^{18}Fluorine-fluorodeoxyglucose, PET: Positron emission tomography

determine covariates for the multivariate analyses. Using these covariates, multivariate Cox regression models were constructed. Hazard ratios (HR) and 95% confidence interval (CI) were calculated. Differences were considered statistically significant at a p value of <0.05.

Results

This study included 72 patients with ILA with a mean age of 63.8±9.7 years, of whom 21 (29.2%) were females and 51 (70.8%) were males. All participants underwent clinically selected appropriate surgical treatment [wedge resection (9), lobectomy (56), and pneumonectomy (7)] in a median duration of 19 (13-32) days after ^{18}F-FDG PET/CT scan. Of these patients, 35 (48.6%) received postoperative adjuvant treatments. The clinicopathological characteristics of patients are summarized in Table 1.

The histopathological subtypes were as follows: 43 (59.7%) AA, 15 (20.8%) SA, 7 (9.8%) LA, 5 (6.9%) PA, and 2 (2.8%) MA. The SUV_{max}, MTV, TLG, energy-uniformity, and entropy values significantly differed between the histopathological subtypes (p values: 0.003, 0.002, 0.003, 0.022, and 0.041, respectively). In post-hoc analyses, the median SUV_{max} and entropy values of the SA-MA were significantly higher, whereas significantly lower in LA. The median MTV and TLG values were significantly higher in PA and lower in LA. A significant difference was found between the LA and SA-MA in MTV. Additionally, significant differences were found in TLG between the LA and PA, and between the LA and SA-MA. The median energy-uniformity value was significantly higher in the LA and lower in the SA-MA. Table 2 demonstrates the comparison of ^{18}F-FDG PET/CT parameters between the subtype groups. Figure 3 shows the representative ^{18}F-FDG PET/CT images and hematoxylin-eosin-stained samples of two different histopathological ILA subtypes.

Tumor diameter was strongly correlated with MTV and TLG (r=0.742 and 0.709, respectively, both p=<0.001). SUV_{max} and entropy had weak positive correlations with tumor diameter (r=0.305 and p=0.009; r=0.412 and p=<0.001, respectively). Skewness, kurtosis, and energy-uniformity had weak and negative correlation with tumor diameter (r=-0.383, -0.406, and -0.445; p=0.001, <0.001, and 0.003, respectively). Lymph node involvement was observed in 21 (29.2%) patients. Among all parameters, only skewness and kurtosis significantly differed between patients with or without lymph node involvement. In those with lymph node involvement, the median skewness and kurtosis values of the tumor were significantly lower than those without lymph node involvement (median skewness: 2.46 and 1.76, respectively, p=0.009; median kurtosis: 8.78 and 5.29, respectively, p=0.008). Significant differences were found between the stage groups in terms of MTV, TLG, skewness, and kurtosis parameters (p=0.001, 0.001, 0.022, and 0.025, respectively). Higher median MTV and TLG values and lower median skewness and kurtosis values were seen in higher-stage tumors. In post-hoc analyses, differences were observed for MTV and TLG between stages 1A and 2A (p=0.003 and 0.005, respectively),

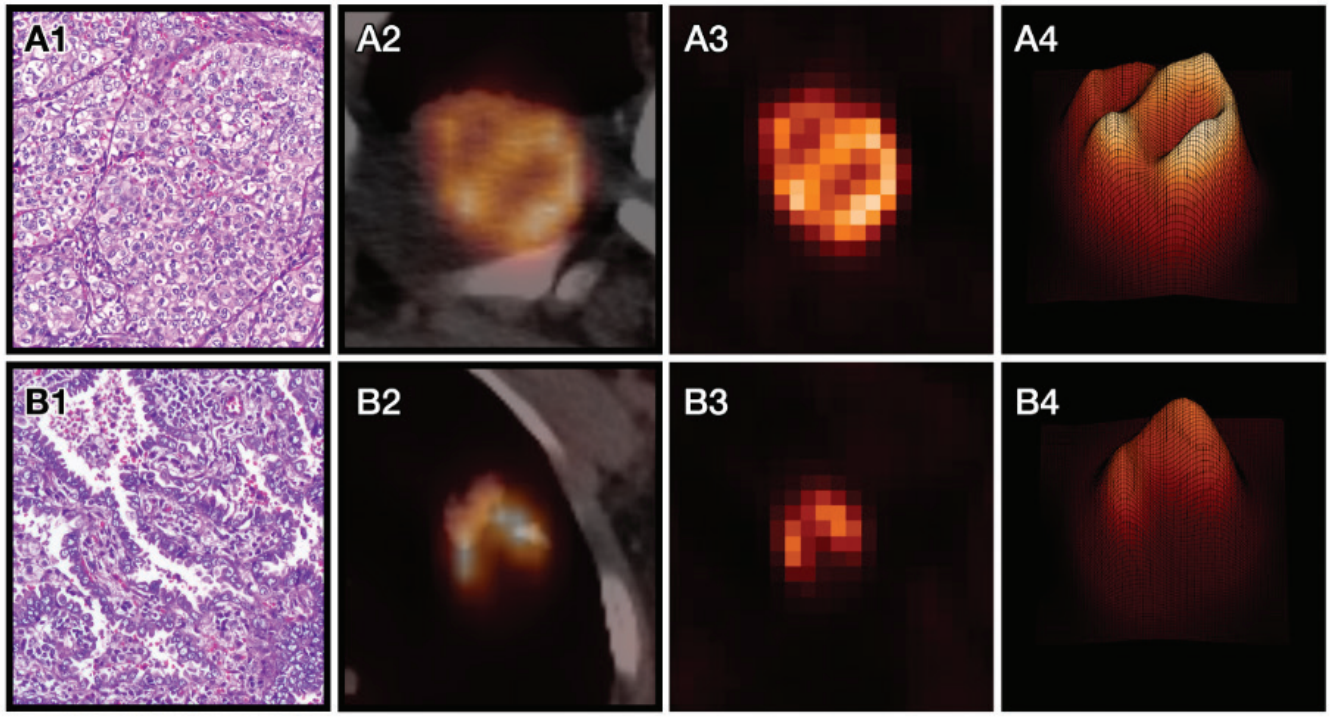

Figure 3. (A) Patient with invasive lung adenocarcinoma of the right upper lobe. Hematoxylin and eosin staining (H&E) (A1) demonstrates the histopathological subtype of lepidic adenocarcinoma (H&E × 100). Transaxial PET/CT image shows invasive lung adenocarcinoma of the right upper lobe with increased ^{18}F-FDG uptake (A2) and relatively lower intra-tumoral heterogeneity (A3 and A4). SUV_{max} of 8.42, the entropy of 1.1387, and energy-uniformity of 0.0848. (B) Patient with invasive lung adenocarcinoma of the left upper lobe. H&E staining (B1) demonstrates the histopathological subtype of solid adenocarcinoma (H&E × 100). Transaxial PET/CT image shows invasive lung adenocarcinoma of the left upper lobe with increased ^{18}F-FDG uptake (B2) and relatively higher intra-tumoral heterogeneity (B3 and B4). SUV_{max} of 47.70, the entropy of 1.7000, and energy-uniformity of 0.0200

SUV_{max}: Maximum standardized uptake value, ^{18}F-FDG: ^{18}Fluorine-fluorodeoxyglucose, PET/CT: Positron emission tomography/computed tomography

stages 1A and 2B (both p=0.001), and stages 1A and 3A (both p=0.002). Additionally, differences were observed for skewness and kurtosis between stages 1A and 3A (p=0.038 and 0.021, respectively).

The median values for follow-up time, PFS, and OS were 31.26, 16.07, and 20.87 months, respectively. During the follow-up time, 33 (45.8%) patients had a relapse and 20 (27.8%) patients died. The univariate Cox regression analyses showed that lymph node involvement was the only significant predictor factor for PFS (HR: 2.101, CI: 1.025-4.039, p=0.043) (Table 3). Univariate Cox regression analyses showed that high tumor diameter (≥3 cm), lymph node involvement, high stage (IIB-IIIA), high SUV_{max} (≥11.69), high MTV (≥9.02 cm^3), high TLG (≥48.38 g), low skewness (≤2.18), low kurtosis (≤7.16), low energy-uniformity (≤0.08), and high entropy (≥1.24) were risk factors that affect the OS (Table 4). The multivariate Cox regression analysis revealed that high SUV_{max} (≥11.69) and advanced stage (IIB-IIIA) was negative independent predictors of OS (Table 5).

Discussion

This study investigated the relationship of ^{18}F-FDG PET/CT parameters, including HBTFs, between clinicopathological factors that affect TH and ILA prognosis. Significant differences were found between the conventional parameters of ^{18}F-FDG PET/CT (SUV_{max}, MTV, and TLG), as well as HBTFs such as entropy and energy-uniformity, and histopathological ILA subtypes. The group consisting of SA and MA had high glycolytic activity and entropy, whereas LA had low glycolytic activity and entropy. Additionally, SA-MA had the lowest energy-uniformity, whereas LA had the highest. Among the ^{18}F-FDG PET/CT parameters, only skewness and kurtosis were associated with lymph node involvement.

TH is an important factor in disease progression and treatment response (20,21). A study that involve patients with advanced lung adenocarcinoma with epidermal growth factor receptor mutation who received tyrosine kinase inhibitor therapy revealed a shorter survival in patients with primary tumors with high entropy values. Additionally, they

Table 1. Patients characteristics		
	N	%
Age (years)		
<65	35	48.6
≥65	37	51.4
Sex		
Male	51	70.8
Female	21	29.2
Lymph node involvement		
Positive	21	29.2
Negative	51	70.8
Stage		
IA	30	41.6
IB	3	4.2
IIA	4	5.6
IIB	15	20.8
IIIA	20	27.8
Subtype		
Acinar	43	59,7
Solid	15	20.8
Lepidic	7	9,8
Papillary	5	6,9
Micropapillary	2	2,8
Operation type		
Wedge resection	9	12.5
Lobectomy	56	77.7
Pneumonectomy	7	9.8
Adjuvant therapy		
Yes	35	48.6
No	37	51.4

reported that entropy value is an independent predictor of treatment response and decreases after treatment (22). According to Hyun et al. (23) lower entropy was independently associated with longer survival in patients with pancreatic ductal adenocarcinoma. In their study on breast cancer, Aide et al. (13) reported that tumors with high entropy and low energy-uniformity have shorter event-free survival, but the log-rank tests reached almost statistical significance. The evidence is insufficient, but all these results suggest that precision medicine will improve with the use of TFs. Our study revealed entropy and energy-uniformity as predictors of OS, but they were not among the independent predictors for OS and PFS in multivariate Cox regression analysis. Higher SUV_{max} (≥11.69) and advanced stage (IIB-IIIA) was significantly associated with poorer OS in our study population.

Table 2. Comparison of the median values of ^{18}F-FDG PET/CT parameters in histopathological subtypes of invasive lung adenocarcinoma groups					
	AA	LA	PA	SA-MA	p value
SUV_{max}	12.07	6.82	10.68	14.89	0.003
MTV	9.11	1.00	63.27	10.08	0.002
TLG	48.82	4.08	275.17	56.87	0.003
Skewness	2.10	3.22	1.91	2.14	0.094
Kurtosis	7.97	12.78	5.06	6.14	0.081
Energy-uniformity	0.0714	0.1424	0.0776	0.0610	0.022
Entropy	1.1385	0.8865	1.1816	1.2539	0.041

Underline indicates statistical insignificance. ^{18}F-FDG: ^{18}Fluorine-fluorodeoxyglucose, PET/CT: Positron emission tomography/computed tomography, AA: Acinar adenocarcinoma, LA: Lepidic adenocarcinoma, PA: Papillary adenocarcinoma, SA-MA: Solid and micropapillary adenocarcinoma; SUV_{max}: Maximum standardized uptake value, MTV: metabolic tumor value, TLG: Total lesion glycolysis

Table 3. The univariate Cox regression analysis of progression-free survival in patients with invasive lung adenocarcinoma			
Variables	HRs	95% confidence intervals	p value
Age (≤65)	0.897	(0.452-1.780)	0.757
Sex (male)	0.940	(0.454-1.944)	0.867
Lymph node involvement (yes)	2.101	(1.025-4.309)	0.043
Stage (IIB-IIIA)	1.920	(0.957-3.855)	0.067
Diameter (≥3 cm)	1.365	(0.658-2.832)	0.403
SUV_{max} (≥11.69)	1.246	(0.625-2.482)	0.532
MTV (≥9.02 cm^3)	1.385	(0.695-2.760)	0.354
TLG (≥48.38 g)	1.104	(0.556-2.191)	0.778
Skewness (≤2.18)	1.267	(0.636-2.525)	0.501
Kurtosis (≤7.16)	1.229	(0.869-1.738)	0.243
Energy-uniformity (≤0.08)	1.486	(0.743-2.972)	0.262
Entropy (≥1.14)	1.763	(0.880-3.532)	0.110

HRs: Hazard ratios, SUV_{max}: Maximum standardized uptake value, MTV: Metabolic tumor value, TLG: Total lesion glycolysis

Entropy and energy-uniformity quantitatively characterize the TH from various perspectives. Entropy refers to the randomness of voxel intensity distribution within the ROI. Entropy increases as the intensities of pixels are chaotically distributed. Energy-uniformity measures the number of repeated pairs. Thus, it reflects the distribution uniformity. This parameter is expected to increase as the number of repeated pixel pairs increases (21). Our findings suggest that SA-MA subtypes have high TH and higher metabolism, whereas LA is more homogeneous with a lower metabolism. Previous study that examine the relationship between the

Table 4. The univariate Cox regression analysis of overall survival in patients with invasive lung adenocarcinoma

	Univariate Cox regression analysis		
Variables	**HRs**	**95% confidence intervals**	**p values**
Age (≤65)	1.200	(0.495-2.909)	0.687
Sex (male)	0.406	(0.134-1.235)	0.112
Lymph node involvement (yes)	2.512	(1.043-6.053)	0.040
Stage (IIB-IIIA)	8.871	(2.050-38.398)	0.004
Diameter (≥3 cm)	3.778	(1.474-9.681)	0.006
SUV_{max} (≥11.69)	4.329	(1.442-12.996)	0.009
MTV (≥9.02 cm^3)	4.495	(1.490-13.563)	0.008
TLG (≥48.38 g)	3.488	(1.253-9.709)	0.017
Skewness (≤2.18)	2.918	(1.056-8.067)	0.039
Kurtosis (≤7.16)	1.761	(1.060-2.929)	0.029
Energy-uniformity (≤0.08)	3.144	(1.137-8.693)	0.027
Entropy (≥1.14)	3.027	(1.097-8.352)	0.032

HRs: Hazard ratios, SUV_{max}: Maximum standardized uptake value, MTV: Metabolic tumor value, TLG: Total lesion glycolysis

Table 5. Independent predictors of overall survival in patients with invasive lung adenocarcinoma

Variables	**The multivariate Cox regression analysis**		
	HRs	**95% confidence intervals**	**p value**
High stage (IIB-IIIA)	7.608	(1.756-32.973)	0.007
High SUV_{max} (≥11.69)	3.580	(1.186-10.806)	0.024

SUV_{max}: Maximum standardized uptake value

histopathological subtypes of ILA and SUV_{max} report that SA had higher SUV_{max} than LA (24). The presence of the SA or MA subtype is a poor prognostic factor (25). According to these findings, the poor prognosis of the SA-MA group may be due to TH and higher metabolic activity.

Among all ^{18}F-FDG PET/CT parameters, only skewness and kurtosis were significantly different in lymph node involvement. These parameters show the distortion or disparity of the histogram that is relative to the normal distribution (18). A recent study described a machine learning-based TFs model as a reliable method for predicting axillary lymph node metastasis in invasive ductal breast cancer (26). Li et al. (27) found that skewness was the most ideal predictor for pelvic lymph node involvement in cervical squamous cell carcinoma. Our previous study revealed that a high-order TF showing the distribution of short homogeneous regions with low gray levels had an independent association with axillary lymph node metastasis unlike other parameters of ^{18}F-FDG PET/CT in invasive ductal breast cancer (28).

However, texture analysis still has a reproducibility barrier to overcome before its clinical practice implementation (14,29). Additionally, TFs that are the most reliable indicator of TH for different tumor types are unclear. HBTFs are based on the analysis of the SUV histogram within the entire tumor. These parameters may have higher chances of clinical applicability in the future because of their simplicity and accessibility compared to more complex higher-order TFs. Most of the TFs are affected by tumor segmentation methods. The present study used the threshold of SUV of 2.5 for the tumor segmentation since the reproducibility of extracted TFs using this threshold was better than that of other thresholds (19). Various tumor segmentation techniques, such as manual or threshold-based methods, are used in the studies; however, no consensus is available on the most appropriate method for ^{18}F-FDG PET/CT textural analysis.

Study Limitations

Limitations of the study include the retrospective design, small sample size, and single-institution experience. Additionally, we cannot extrapolate the findings to patients with advanced stage ILA.

Conclusion

High stage and high SUV_{max} were independent risk factors for OS in patients with ILA. The homogeneity of LA and the heterogeneity of SA-MA were quantified by HBTFs. Lymph node involvement was predicted by skewness and kurtosis. Therefore, HBTFs may improve the prognostic value of ^{18}F-FDG PET/CT by contributing to the quantification of TH. If confirmed by larger, prospective, and multi-center studies, extracted HBTFs from ^{18}F-FDG PET/CT could potentially become non-invasive prognostic imaging biomarkers to guide precision medicine.

Ethics

Committee Approval: The Local Ethics Committee of KTO Karatay University Faculty of Medicine approved this study under the decision number: 2021/010, number: E-41901325-050.99-2306.

Informed Consent: The informed consent form was obtained from the patients or their relatives who participated in the study.

Peer-review: Externally peer-reviewed.

Authorship Contributions

Surgical and Medical Practices: H.Ö., M.İ.E.K., Concept: H.Ö., M.İ.E.K., N.C., Design: H.Ö., N.C., Data Collection or Processing: H.Ö., N.C., Analysis or Interpretation: H.Ö., N.C., Literature Search: H.Ö., N.C., M.E., M.İ.E.K., Writing: H.Ö., N.C., M.E., M.İ.E.K.

Conflict of Interest: No conflict of interest was declared by the authors.

Financial Disclosure: The authors declared that this study has received no financial support.

References

1. Bray F, Ferlay J, Soerjomataram I, Siegel RL, Torre LA, Jemal A. Global cancer statistics 2018: GLOBOCAN estimates of incidence and mortality worldwide for 36 cancers in 185 countries. CA Cancer J Clin 2018;68:394-424. Erratum in: CA Cancer J Clin 2020;70:313.
2. Reck M, Popat S, Reinmuth N, De Ruysscher D, Kerr KM, Peters S; ESMO Guidelines Working Group. Metastatic non-small-cell lung cancer (NSCLC): ESMO Clinical Practice Guidelines for diagnosis, treatment and follow-up. Ann Oncol 2014;25 (Suppl 3):iii27-39.
3. Russell PA, Wainer Z, Wright GM, Daniels M, Conron M, Williams RA. Does lung adenocarcinoma subtype predict patient survival?: A clinicopathologic study based on the new International Association for the Study of Lung Cancer/American Thoracic Society/European Respiratory Society international multidisciplinary lung adenocarcinoma classification. J Thorac Oncol 2011;6:1496-1504.
4. Bedard PL, Hansen AR, Ratain MJ, Siu LL. Tumour heterogeneity in the clinic. Nature 2013;501:355-364.
5. Bashir U, Siddique MM, Mclean E, Goh V, Cook GJ. Imaging heterogeneity in lung cancer: techniques, applications, and challenges. AJR Am J Roentgenol 2016;207:534-543.
6. Chicklore S, Goh V, Siddique M, Roy A, Marsden PK, Cook GJ. Quantifying tumour heterogeneity in 18F-FDG PET/CT imaging by texture analysis. Eur J Nucl Med Mol Imaging 2013;40:133-140.
7. Zhang J, Ma G, Cheng J, Song S, Zhang Y, Shi LQ. Diagnostic classification of solitary pulmonary nodules using support vector machine model based on 2-[18F]fluoro-2-deoxy-D-glucose PET/computed tomography texture features. Nucl Med Commun 2020;41:560-566.
8. Nakajo M, Jinguji M, Aoki M, Tani A, Sato M, Yoshiura T. The clinical value of texture analysis of dual-time-point 18F-FDG-PET/CT imaging to differentiate between 18F-FDG-avid benign and malignant pulmonary lesions. Eur Radiol 2020;30:1759-1769.
9. Aydos U, Ünal ER, Özçelik M, Akdemir D, Ekinci Ö, Taştepe AI, Memiş L, Atay LÖ, Akdemir ÜÖ. Texture features of primary tumor on 18F-FDG PET images in non-small cell lung cancer: the relationship between imaging and histopathological parameters. Rev Esp Med Nucl Imagen Mol (Engl Ed) 2021;S2253-654X:30134-30137.
10. Önner H, Abdülrezzak Ü, Tutuş A. Could the skewness and kurtosis texture parameters of lesions obtained from pretreatment Ga-68 DOTA-TATE PET/CT images predict receptor radionuclide therapy response in patients with gastroenteropancreatic neuroendocrine tumors? Nucl Med Commun 2020;41:1034-1039.
11. Martin-Gonzalez P, de Mariscal EG, Martino ME, Gordaliza PM, Peligros I, Carreras JL, Calvo FA, Pascau J, Desco M, Muñoz-Barrutia A. Association of visual and quantitative heterogeneity of 18F-FDG PET images with treatment response in locally advanced rectal cancer: a feasibility study. PLoS One 2020;15:e0242597.
12. Kang J, Lee JH, Lee HS, Cho ES, Park EJ, Baik SH, Lee KY, Park C, Yeu Y, Clemenceau JR, Park S, Xu H, Hong C, Hwang TH. Radiomics features of 18f-fluorodeoxyglucose positron-emission tomography as a novel prognostic signature in colorectal cancer. Cancers (Basel) 2021;13:392.
13. Aide N, Elie N, Blanc-Fournier C, Levy C, Salomon T, Lasnon C. Hormonal receptor immunochemistry heterogeneity and 18F-FDG metabolic heterogeneity: preliminary results of their relationship and prognostic value in luminal non-metastatic breast cancers. Front Oncol 2021;10:599050.
14. Nyflot MJ, Yang F, Byrd D, Bowen SR, Sandison GA, Kinahan PE. Quantitative radiomics: impact of stochastic effects on textural feature analysis implies the need for standards. J Med Imaging (Bellingham) 2015;2:041002.
15. Ercelep O, Alan O, Telli TA, Tuylu TB, Arıkan R, Demircan NC, Simsek ET, Babacan NA, Kaya S, Dane F, Bozkurtlar E, Ones T, Lacin T, Yumuk PF. Differences in PET/CT standardized uptake values involvement and survival compared to histologic subtypes of lung adenocarcinoma. Tumori 2021;107:231-237.
16. Chiu CH, Yeh YC, Lin KH, Wu YC, Lee YC, Chou TY, Tsai CM. Histological subtypes of lung adenocarcinoma have differential ^{18}F-fluorodeoxyglucose uptakes on the positron emission tomography/computed tomography scan. J Thorac Oncol 2011;6:1697-1703.
17. Goldstraw P, Chansky K, Crowley J, Rami-Porta R, Asamura H, Eberhardt WE, Nicholson AG, Groome P, Mitchell A, Bolejack V; International Association for the Study of Lung Cancer Staging and Prognostic Factors Committee, Advisory Boards, and Participating Institutions; International Association for the Study of Lung Cancer Staging and Prognostic Factors Committee Advisory Boards and Participating Institutions. The IASLC lung cancer staging project: proposals for revision of the TNM stage groupings in the forthcoming (eighth) edition of the TNM classification for lung cancer. J Thorac Oncol 2016;11:39-51.
18. Nioche C, Orlhac F, Boughdad S, Reuzé S, Goya-Outi J, Robert C, Pellot-Barakat C, Soussan M, Frouin F, Buvat I. LIFEx: a freeware for radiomic feature calculation in multimodality imaging to accelerate advances in the characterization of tumor heterogeneity. Cancer Res 2018;78:4786-4789.
19. Konert T, Everitt S, La Fontaine MD, van de Kamer JB, MacManus MP, Vogel WV, Callahan J, Sonke JJ. Robust, independent and relevant prognostic 18F-fluorodeoxyglucose positron emission tomography radiomics features in non-small cell lung cancer: are there any? PLoS One 2020;15:e0228793.
20. Gerlinger M, Rowan AJ, Horswell S, Math M, Larkin J, Endesfelder D, Gronroos E, Martinez P, Matthews N, Stewart A, Tarpey P, Varela I, Phillimore B, Begum S, McDonald NQ, Butler A, Jones D, Raine K, Latimer C, Santos CR, Nohadani M, Eklund AC, Spencer-Dene B, Clark G, Pickering L, Stamp G, Gore M, Szallasi Z, Downward J, Futreal PA, Swanton C. Intratumor heterogeneity and branched evolution revealed by multiregion sequencing. N Engl J Med 2012;366:883-892. Erratum in: N Engl J Med 2012;367:976.
21. Lemarignier C, Martineau A, Teixeira L, Vercellino L, Espié M, Merlet P, Groheux D. Correlation between tumour characteristics, SUV measurements, metabolic tumour volume, TLG and textural features assessed with 18F-FDG PET in a large cohort of oestrogen receptor-positive breast cancer patients. Eur J Nucl Med Mol Imaging 2017;44:1145-1154.
22. Chen YH, Wang TF, Chu SC, Lin CB, Wang LY, Lue KH, Liu SH, Chan SC. Incorporating radiomic feature of pretreatment 18F-FDG PET improves survival stratification in patients with EGFR-mutated lung adenocarcinoma. PLoS One 2020;15:e0244502.
23. Hyun SH, Kim HS, Choi SH, Choi DW, Lee JK, Lee KH, Park JO, Lee KH, Kim BT, Choi JY. Intratumoral heterogeneity of (18)F-FDG uptake predicts survival in patients with pancreatic ductal adenocarcinoma. Eur J Nucl Med Mol Imaging 2016;43:1461-1468.
24. Ventura L, Scarlattei M, Gnetti L, Silini EM, Rossi M, Tiseo M, Sverzellati N, Bocchialini G, Musini L, Balestra V, Ampollini L, Rusca M, Carbognani

P, Ruffini L. Prognostic value of [18F]FDG PET/CT parameters in surgically resected primary lung adenocarcinoma: a single-center experience. Tumori 2020;106:212-222.

25. Travis WD, Brambilla E, Nicholson AG, Yatabe Y, Austin JHM, Beasley MB, Chirieac LR, Dacic S, Duhig E, Flieder DB, Geisinger K, Hirsch FR, Ishikawa Y, Kerr KM, Noguchi M, Pelosi G, Powell CA, Tsao MS, Wistuba I; WHO Panel. The 2015 World Health Organization Classification of Lung Tumors: Impact of Genetic, Clinical and Radiologic Advances Since the 2004 Classification. J Thorac Oncol 2015;10:1243-1260.
26. Song BI. A machine learning-based radiomics model for the prediction of axillary lymph-node metastasis in breast cancer. Breast Cancer 2021;28:664-671.
27. Li K, Sun H, Lu Z, Xin J, Zhang L, Guo Y, Guo Q. Value of [18F]FDG PET radiomic features and VEGF expression in predicting pelvic lymphatic metastasis and their potential relationship in early-stage cervical squamous cell carcinoma. Eur J Radiol 2018;106:160-166.
28. Önner H, Coskun N, Erol M, Karanis MIE. Association of 18F-FDG PET/CT textural features with immunohistochemical characteristics in invasive ductal breast cancer. Rev Esp Med Nucl Imagen Mol (Engl Ed) 2021;S2253-654X:30201-30208.
29. Jha AK, Mithun S, Jaiswar V, Sherkhane UB, Purandare NC, Prabhash K, Rangarajan V, Dekker A, Wee L, Traverso A. Repeatability and reproducibility study of radiomic features on a phantom and human cohort. Nature 2021. doi.org/10.1038/s41598-021-81526-8.

Original Article
Mol Imaging Radionucl Ther 2022;31:42-48 DOI:10.4274/mirt.galenos.2021.85530

Use of YouTube as an Information Source for Radioactive Iodine Therapy: Do YouTube Videos Have High Quality?

YouTube'un Radyoaktif İyot Tedavisi için Bilgi Kaynağı Olarak Kullanılması: YouTube Videoları Yüksek Kaliteye Sahip mi?

Hüseyin Şan

Ankara City Hospital, Clinic of Nuclear Medicine, Ankara, Turkey

Abstract

Objectives: Radioactive iodine (RAI) therapy is a radionuclide treatment for hyperthyroidism and well-differentiated thyroid cancer. One of the most popular sources of information for patients on the internet is YouTube. This study aimed to examine the quality of videos about RAI treatment.

Methods: This cross-sectional study was performed by using videos in YouTube. The terms "radyoaktif iyot tedavisi" and "radioactive iodine treatment" were used to search related videos in June 2021. The quality of the videos was assessed by using the Journal of the American Medical Association (JAMA) benchmark criteria, the DISCERN scale, and the global quality scale (GQS).

Results: Of the total 88 videos evaluated, 56 videos (30 in English, 26 in Turkish) were analyzed according to the inclusion and exclusion criteria. Seven (12.5%) videos were assigned to the high-quality group, 16 (28.58%) to the intermediate quality group, and 33 (58.92%) to the low quality group. The findings of this study showed that the most popular videos with the highest video power index (VPI) scores and the highest number of video likes and comments belonged to the intermediate quality group. Contrarily, popularity level, number of video likes, and number of video views were the lowest in the high-quality group. The analysis of video sources revealed that viewers most preferred non-physician-sourced videos, with average total views of 59307.80 [standard deviation (SD): 122554.13]. The most liked videos were non-physician-made videos, with average total likes of 424.35 (SD: 639.41). The mean VPI scores were the highest in non-physician-made videos, with 25.18 (SD: 25.69). The average JAMA (1.92, SD: 0.50), DISCERN (34.31, SD: 14.33), and GQS scores (2.61, SD: 0.99) were the highest in physician-made videos.

Conclusion: Although high-quality videos on YouTube may inform and encourage patients positively, unprofessional, incorrect, and incomplete information can be also uploaded on YouTube and may mislead patients.

Keywords: Video, radioactive iodine, treatment, internet

Öz

Amaç: Radyoaktif iyot (RAI) tedavisi, hipertiroidizm ve iyi diferansiye tiroid kanseri için bir radyonüklid tedavisidir. İnternette hastalar için en popüler bilgi kaynaklarından biri YouTube'dir. Bu çalışma, RAI tedavisi ile ilgili videoların kalitesini incelemeyi amaçlamaktadır.

Yöntem: Bu kesitsel çalışma YouTube kullanılarak gerçekleştirilmiştir. Haziran 2021'de ilgili videoların aranmasında "radyoaktif iyot tedavisi" ve "radioactive iodine treatment" terimleri kullanıldı. Videoların kalitesi, Amerikan Tıp Derneği Dergisi (JAMA) benchmark kriterleri, DISCERN ölçeği ve küresel kalite ölçeği kullanılarak (GQS) değerlendirildi.

Bulgular: Toplam 88 video değerlendirildi ve toplam 56 video (30 İngilizce, 26 Türkçe) dahil edilme ve hariç tutulma kriterlerine göre analiz edildi. Yedi video (%12,5) yüksek kaliteli grup, 16 video (%28,58) orta kaliteli grup ve 33 video (%58,92) düşük kaliteli grup olarak sınıflandırıldı. Çalışmamızın bulguları, en yüksek video güç indeksi puanına sahip en popüler videolar ile en fazla beğeni ve yorum sayısına sahip videoların orta

Address for Correspondence: Hüseyin Şan MD, Ankara City Hospital, Clinic of Nuclear Medicine, Ankara, Turkey
Phone: +90 537 497 06 30 **E-mail:** dr.huseyinsan@yahoo.com ORCID ID: orcid.org/0000-0002-2264-5446
Received: 17.07.2021 **Accepted:** 29.09.2021

kalite grubundaki videolar olduğunu gösterdi. Aksine, popülerlik düzeyi, video beğeni sayısı ve video izlenme sayısı yüksek kaliteli video grubunda en düşük bulundu. Video kaynaklarının analizinde; izleyiciler tarafından en çok tercih edilen videoların, ortalama 59307,80 [standart sapma (SS): 122554,13] izlenme sayısı ile hekim kaynaklı olmayan videolar olduğu saptandı. En çok beğenilen videolar ise ortalama 424,35 (SS: 639,41) beğeni ile hekim olmayanlara aitti. Video güç indeksi puanlarının ortalaması en yüksek 25,18 (SS: 25,69) olarak saptanmış ve hekim olmayanlara ait videolarda bulunmuştur. Doktorlara ait videolarda ortalama JAMA (1,92, SS: 0,50), DISCERN (34,31, SS: 14,33) ve GQS puanları (2,61, SS: 0,99) en yüksek olarak saptanmıştır.

Sonuç: Her ne kadar YouTube'deki yüksek kaliteli videolar, hastaları olumlu yönde bilgilendirebilmekte ve teşvik edici olabilmekte ise de; yanlış ve eksik bilgilendirmelerin de bu platforma yüklenebileceği ve hastaları yanıltabileceği unutulmamalıdır.

Anahtar kelimeler: Video, radyoaktif iyot, tedavi, internet

Introduction

Radioactive iodine (RAI) was the first radiopharmaceutical of clinical importance in nuclear medicine (1). RAI treatment has been used to treat hyperthyroidism and well-differentiated thyroid carcinoma (2,3), and the basic term "radiotheranostics" has been used in clinical practice since 1940s (4). RAI treatment remains the main treatment strategy, especially in well-differentiated thyroid cancer of intermediate- and high-risk features. Moreover, RAI treatment in hyperthyroidism is safe, cost-effective, and efficient (5,6,7). Detailed verbal and written information about RAI treatment, side effects, and radiation protection precautions before, during, and after treatment preparations or requirements is always given to the patient, and signed informed consent is inevitably taken. Despite the provision of adequate information, some patients may be hesitant, anxious, and curious about RAI treatment. Thus, patients use social media websites and search engines to reach information easily. Social media websites and search engines have great potential to provide free and easy access to targeted information; however, data received can be neither accurate nor free of bias and sometimes irrelevant and incomplete (8).

At present, by the increasing access to the Internet, patients tend to utilize YouTube to obtain medical information. In a study by Yoon et al. (9) of 17.704 adults, approximately 40% used the internet for health information. YouTube is one of the most important online sources used by people for medical purposes. YouTube is a worldwide video-sharing service that provides free access to videos and is an alternative platform to deliver health-related information (10). However, the advertisement and non-scientific content uploaded on YouTube raise concerns about the quality and accuracy of medical videos (10). This study aimed to evaluate the quality of contents on "radioactive iodine treatment" and "radyoaktif iyot tedavisi" by analyzing YouTube videos. To the best of our knowledge, this is the first study to evaluate the quality of YouTube videos about "radioactive iodine treatment." Results from this study can help provide reliable and scientifically accurate video content about RAI treatment.

Materials and Methods

This cross-sectional study was performed using YouTube, a video-sharing website. For video selection, the terms "radioactive iodine treatment" and "radyoaktif iyot tedavisi" were used to search for related videos on June 2021. The options "video" and "sort by the number of views" were selected as filters. All URLs retracted were recorded in an Excel sheet and assessed by a nuclear medicine specialist experienced in RAI treatment. A total of 88 videos (44 in English, 44 in Turkish) were assessed, and 56 videos (30 in English, 26 in Turkish) were included in the study according to the inclusion and exclusion criteria. The inclusion criteria were as follows: English videos on "radioactive iodine treatment" and Turkish videos on "radyoaktif iyot tedavisi." The exclusion criteria were as follows: Duplicate videos, inaccessible videos, contents unrelated to RAI treatment, and videos in a language other than English and Turkish.

Video duration (seconds), time passed since video upload (days), total views, total comments, number of comments per year, number of likes and dislikes, video like ratio [like/(like+dislike) ×100], and video view ratio (number of views/days) were recorded during the evaluation procedure. Video power index (VPI) (like ratio × view ratio/100), which is used to determine the video popularity level, was also calculated for each video.

The contents of the videos were categorized as "RAI treatment for thyroid cancer," "RAI treatment for hyperthyroidism," "patient experience of hyperthyroidism treatment with RAI," "patient experience of thyroid cancer treatment with RAI," "RAI treatment for thyroid cancer and hyperthyroidism," and "against RAI treatment." Video sources were analyzed into five categories as physician, patient, nuclear medicine physicist, nurse, and nutritionist. Video quality was assessed by using the Journal of the American Medical Association (JAMA) benchmark criteria, DISCERN Scale, and global quality scale (GQS).

The JAMA benchmark criteria, which are used to evaluate video reliability and accuracy, include the following parameters: Authorship, attribution, disclosure, and currency, with 1 point assigned for the presence of each criterion (11). A score of 0 demonstrated poor reliability and accuracy, whereas four points shows higher reliability and accuracy (11).

The DISCERN scale is an instrument consisting of questions on the quality of information about treatment options, reliability, and quality of the overall content (12). The score ranges from 0 to 80 points, with higher scores indicating the advanced level of quality (12). GQS is a 5-point instrument used to evaluate the quality, flow, and ease of use of the video content, with 1-2 points indicating low quality, three points intermediate quality, and 4-5 points high quality (13). As our study did not include any animal or human participants and the videos analyzed were accessible for everyone, the study did not require ethics committee approval. There are similar studies with the same protocol (10,14).

Statistical Analysis

Statistical analyses were performed using SPSS software version 26.0 (IBM Corp., Armonk, NY, USA). The Kolmogorov-Smirnov test was used to determine whether the obtained parameters conformed to a normal distribution. Descriptive analyses were used, and values were presented as mean ± standard deviation (SD). The Kruskal-Wallis and Mann-Whitney U tests were used to compare continuous variables. While investigating the associations between non-normally distributed or ordinal variables, the correlation coefficients (r) and their significance (p) were calculated using the Spearman test. A probability value of $p<0.05$ was considered significant.

Results

We have evaluated a total of 88 videos. Of these videos, 31.81% (n=28) had unrelated content, and 4.5% (n=4) were videos uploaded in languages other than English and Turkish. We have analyzed a total of 56 videos according to the inclusion and exclusion criteria. The videos were uploaded by physicians, patients, nuclear medicine physicists, nurses, and nutritionists, and the distribution of videos according to these sources were 64.28% (n=36), 30.35% (n=17), 1.79% (n=1), 1.79% (n=1), and 1.79% (n=1), respectively. According to the GQS score, videos were categorized into high-quality (n=7, 12.5%), intermediate quality (n=16, 28.58%), and low quality (n=33, 58.92%) groups. The categorization of video qualities according to their sources is shown in Table 1.

The specialties of the physicians were nuclear medicine (n=13, 36.11%), general surgery (n=9, 25%), endocrinology (n=4, 11.11%), oncology (n=2, 5.54%), radiology (n=1, 2.77%), and unknown (n=7, 19.44%). Moreover, 50% (9/18) of the physicians who uploaded videos in Turkish and 22.22% (4/18) who uploaded videos in English were nuclear medicine specialists.

Video contents were categorized as RAI treatment for thyroid cancer, RAI treatment for hyperthyroidism, patient experience of hyperthyroidism treatment with RAI, patient experience of thyroid cancer treatment with RAI, RAI treatment for thyroid cancer and hyperthyroidism, and against RAI treatment. The corresponding rates were 28.57% (16/56), 17.85% (10/56), 8.92% (5/56), 26.78% (15/56), 16.07% (9/56), and 1.78% (1/56), respectively.

The average duration of videos was 455.07 (SD: 410.11) seconds. The average time that has passed since video upload was 1820.16 (SD: 1193.86) days. The average total view was 36,856.52 (SD: 78591.75). The average number of comments was 47.30 (SD: 99.43). The average number of comments per year was 14.72 (SD: 32.79). The average number of video likes was 228.27 (SD: 428.29), and the average number of video dislikes was 12.95 (SD: 21.59). The average video like ratio was 85.21 (SD: 26.21). The average video view ratio was 24.08 (SD: 45.64). The average VPI was 17.04 (SD: 22.05) (Table 2).

The average durations of low-, intermediate-, and high-quality videos were 385.55 (SD: 360.34), 483.69 (SD: 519.76), and 716 (SD: 256.63) seconds, respectively. The average time that has passed since video upload of low, intermediate-, and high-quality videos were 1743.09 (SD: 1200.74), 1809.81 (SD: 1288.07), and 2207.14 (SD: 1009.98) days, respectively. The average total views of low-, intermediate-, and high-quality videos were 41,926.70 (SD: 98,390.66), 35,159.69 (SD: 41,172.20), and 16,832.71 (SD: 11,583.25), respectively. The average numbers of comments in low-, intermediate-, and high-quality videos were 41.48 (SD: 65.518), 73.13 (SD: 160.387), and 15.71 (SD: 17.49), respectively. The average numbers of comments per year in low-, intermediate-, and high-quality videos were 11.62 (SD: 22.85), 25.69 (SD: 51.10), and 4.40 (SD: 6.93), respectively. The average numbers of likes of low-, intermediate-, and high-quality videos were 199.36 (SD: 352.34), 349.56 (SD: 615.85), and 87.29 (SD: 64.76), respectively. The average numbers of dislikes of low-, intermediate-, and high-quality videos were 13.15 (SD: 21.77), 16.38 (SD: 25.31), and 4.14 (SD: 4.81), respectively. The average video like ratios of low-, intermediate-, and high-quality videos were 81.93 (SD: 29.53), 86.92 (SD: 23.76), and 96.78 (SD: 3.45),

respectively. The average view ratios of low-, intermediate-, and high-quality videos were 25.39 (SD: 55.32), 27.49 (SD: 31.14), and 10.10 (SD: 8.87), respectively. The average VPI scores of low-, intermediate-, and high-quality videos were 14.77 (SD: 19.23), 24.92 (SD: 29.35), and 9.67 (SD: 8.56), respectively (Table 2).

The mean JAMA, GQS, and DISCERN scores of the low, intermediate-, and high-quality videos were 1.75±0.54, 2.43±0.91, and 30.66±13.36, respectively. The mean JAMA and DISCERN scores were 1.55±0.5, 1.94±0.25, and 2.29±0.75 and 22.58±6.35, 35.25±6.43, and 58.29±3.45, respectively. The mean JAMA, GQS, and DISCERN scores of Turkish videos were 1.69±0.47, 2.42±0.90, and 30.65±13.87, respectively. The mean JAMA, GQS, and DISCERN scores of English videos were 1.80±0.61, 2.43±0.93, and 30.67±13.14, respectively (Table 2).

The analysis of video sources revealed that viewers most preferred non-physician-made videos, with average total views of 59,307.80 (SD: 122554.13). Similarly, non-physician-made videos were the most commented videos, with average total comments of 102.95 (SD: 149.29). In addition, the most liked videos were uploaded by non-

Table 1. Categorization of video quality and language according to sources, n (%)

		Video language						
		English			Turkish			
		Low quality	Intermediate quality	High quality	Low quality	Intermediate quality	High quality	Total
Video source	Physician	8 (14.285%)	7 (12.499%)	3 (5.357%)	10 (17.856%)	4 (7.142%)	4 (7.142%)	36 (64.285%)
	Patient	8 (14.285%)	2 (3.571%)	0 (0%)	5 (8.928%)	2 (3.571%)	0 (0%)	17 (30.357%)
	Nutritionist	0 (0%)	0 (0%)	0 (0%)	1 (1.785%)	0 (0%)	0 (0%)	1 (1.785%)
	Nuclear medicine physicist	0 (0%)	1 (1.785%)	0 (0%)	0 (0%)	0 (0%)	0 (0%)	1 (1.785%)
	Nurse	1 (1.785%)	0 (0%)	0 (0%)	0 (0%)	0 (0%)	0 (0%)	1 (1.785%)
	Total	17 (30.357%)	10 (17.857%)	3 (5.357%)	16 (28.571%)	6 (10.714%)	4 (7.142%)	56 (100%)

Table 2. General characteristics of videos according to quality and language

	Mean (SD)							
	Video quality				Video language			All videos
	Low	Intermediate	High	p value	Turkish	English	p value	
Video duration (second)	385.85 (360.347)	483.69 (519.762)	716 (256.635)	0.026	427.92 (473.74)	478.60 (352.52)	0.165	455.07 (410.11)
Number of video views	41926.70 (98390.66)	35159.69 (41172.20)	16832.71 (11583.25)	0.592	19724.77 (25625.95)	51704.3 (103233.05)	0.010	36856.52 (78591.75)
Number of video likes	199.36 (352.344)	349.56 (615.858)	87.29 (64.76)	0.576	190.15 (404.00)	261.30 (452.50)	0.027	228.27 (428.29)
Number of video dislikes	13.15 (21.775)	16.38 (25.319)	4.14 (4.81)	0.289	10.58 (22.41)	15.00 (21.03)	0.078	12.95 (21.59)
Number of comments	41.48 (65.51)	73.13 (160.38)	15.71 (17.49)	0.335	29.96 (64.12)	62.33 (121.26)	0.005	47.30 (99.43)
Number of comments per year	11.62 (22.85)	25.60 (51.10)	4.40 (6.93)	0.234	13.47 (27.69)	15.79 (37.08)	0.028	14.72 (32.79)
VPI	14.77 (19.23)	24.92 (29.35)	9.67 (8.56)	0.366	16.42 (22.34)	17.57 (22.16)	0.411	17.03 (22.05)
JAMA score	1.55 (0.5)	1.94 (0.25)	2.29 (0.75)	0.002	1.69 (0.47)	1.80 (0.61)	0.607	1.75 (0.54)
DISCERN score	22.58 (6.35)	35.25 (6.43)	58.29 (3.45)	0.001	30.65 (13.87)	30.67 (13.14)	0.573	30.66 (13.36)
GQS score	1.79 (0.41)	3 (0)	4.14 (0.37)	0.001	2.42 (0.90)	2.43 (0.93)	0.951	2.43 (0.91)

VPI: Video power index, JAMA: Journal of American Medical Association, GQS: Global quality scale, SD: Standard deviation

physicians, with average total likes of 424.35 (SD: 639.41). The mean VPI scores were the highest in videos made by non-physicians, with an average score of 25.18 (SD: 25.69). The average JAMA (1.92, SD: 0.50), DISCERN (34.31, SD: 14.33), and GQS scores (2.61, SD: 0.99) were highest in physician-made videos.

The results of this study revealed a positive and intermediate correlation between JAMA and DISCERN ($p<0.001$, $r=0.535$) scores and between JAMA and GQS ($p<0.001$, $r=0.521$) scores. In addition, a positive and high correlation was found between DISCERN and GQS scores ($p<0.001$, $p=0.833$).

No significant difference was found ($p>0.05$) between Turkish and English videos in terms of JAMA, DISCERN, and GQS scores, duration, like ratio, view ratio, number of dislikes, and VPI. The difference between Turkish and English videos was significant ($p<0.05$) with respect to the number of views, number of likes, number of comments, and number of comments per year (Table 2).

The difference between physician-made and non-physician-made videos was significant in terms of duration ($p=0.001$), total number of comments ($p<0.001$), number of likes ($p=0.006$), number of comments per year ($p<0.001$), JAMA score ($p=0.001$), DISCERN score ($p=0.012$), view ratio ($p=0.017$), VPI ($p=0.044$), number of views ($p=0.037$), and number of dislikes ($p=0.025$) (Table 3).

Table 3. General characteristics of videos according to sources

	Mean (SD)		
	Video source		
	Physician	Non-physician	p value
Video duration (sec)	315.08 (277.29)	707.05 (491.17)	0.001
Number of video views	24383.58 (33236.73)	59307.80 (122554.13)	0.037
Number of video likes	119.33 (179.27)	424.35 (639.41)	0.006
Number of video dislikes	8.81 (14.406)	20.40 (29.168)	0.025
Number of comments	16.39 (26.188)	102.95 (149.29)	<0.001
Number of comments per year	4.19 (8.38)	33.66 (48.93)	<0.001
VPI	12.51 (18.62)	25.18 (25.69)	0.044
JAMA score	1.92 (0.5)	1.45 (0.51)	0.001
DISCERN score	34.31 (14.33)	24.10 (8.24)	0.012
GQS score	2.61 (0.99)	2.1 (0.64)	0.056

VPI: Video power index, JAMA: Journal of American Medical Association, GQS: Global quality scale, SD: Standard deviation

Discussion

The development of technology and the increase in the use of computers, tablets, and smartphones has boosted internet access. Individuals have started to prefer to search for information over the internet in almost every aspect of life. Additionally, patients have recently started to use the Internet to obtain information about diseases and treatment procedures. Many studies have reported that 80% of Internet users have obtained medical information from the Internet (15,16,17). YouTube is one of the most popular sources of information for patients (17). Studies have also shown that new videos are constantly being uploaded to YouTube (17,18,19). YouTube is watched by approximately two billion daily, and internet users spend approximately 15 min a day watching videos from this site (17,18,19). The results of three studies by Fox (20,21,22,23) have revealed that the decisions of 75% of Internet users were influenced by online information when searching about their diseases and treatment. Online platforms, particularly YouTube, have a significant potential to share medical information among users (17,20,21,22,23). However, given the minimum regulatory mechanisms for uploading videos to YouTube, doubts have arisen about the accuracy, reliability, and quality of the content and information provided (17).

Since RAI treatment is not well known by patients, this topic has been searched many times on YouTube, and many videos about RAI treatment have been uploaded and watched. To the best of our knowledge, no studies have reported the quality and reliability of videos about RAI treatment.

In our study, YouTube videos related to RAI treatment were categorized according to the GQS score. Most of the videos were of low quality, and the number of high-quality videos was the lowest. This is related partly to the fact that uploaded videos contain patient experiences and are uploaded by physicians, other than nuclear medicine specialists, and non-physician health care workers.

In our study that the most viewed and commented videos, the most liked, and the most popular videos (highest VPI scores) were made by non-physicians. In addition, videos with the highest quality based on JAMA, DISCERN, and GQS scores were physician-made videos. This occurs because patients receiving RAI treatment directly describe their individual treatment-related experiences more understandably and simply. Although physician-made videos were watched and commented less because of possibly complicated scientific terms used, they were better than non-physician-made videos in terms of the scientific quality of the content.

The findings of our study showed that intermediate quality videos were the most popular with the highest VPI scores, likes, and comments. By contrast, high-quality videos had the lowest popularity level (VPI scores) and number of likes and views. This is because the number of high-quality videos is considerably lower than that of intermediate- and low quality videos. In all circumstances, the most popular YouTube videos of RAI treatment may not always include the highest quality of information based on our results. In addition, patients should choose videos that are beneficial to them, and it is thought that the most watched, liked, and commented videos may not provide accurate information to the patients.

In our study, Turkish and English videos of RAI treatment were not significantly different in terms of video quality and VPI. Approximately 50% of the physicians who uploaded videos in Turkish and 22% of the physicians who uploaded videos in English were nuclear medicine specialists. RAI treatment is specific to nuclear medicine, as it includes radiation safety issues for patients and their relatives. Nuclear medicine specialists should provide accurate information to the patients about the subject and clinical practice regarding RAI treatment. Therefore, more widespread use of YouTube by nuclear medicine specialists may be beneficial. It would be more appropriate to prepare videos about RAI treatment for online publication under the supervision of nuclear medicine specialists.

Although Turkish and English videos were not different in terms of quality, a significant difference was observed in the number of video views, likes, comments, and comments per year. This finding is considered to be due to the finding that English videos reached and are preferred by more YouTube users worldwide.

Study Limitations

This study has several limitations. In this study, we only included videos in Turkish and English. In addition, not all YouTube videos about RAI treatment in English and Turkish were included in this study. Inclusion of videos in other languages and all videos in English and Turkish about RAI treatment may change our findings, although not highly likely. Finally, GQS, which was used to evaluate video quality, is a subjective assessment scale.

Conclusion

Since RAI therapy is a specific radionuclide treatment of nuclear medicine for hyperthyroidism and well-differentiated thyroid cancer, patients should receive high-quality, and accurate information from reliable sources for their disease and treatment. Although high-quality videos on YouTube may inform and encourage patients positively, unprofessional, inaccurate, and incomplete information can be also uploaded to this platform and may mislead patients. Thus, physicians should provide detailed verbal and written information to patients about their disease and treatment and refer patients to scientific sources which they can obtain reliable information. Therefore, under the guidance of the Turkish Society of Nuclear Medicine, it is essential to prepare an official, comprehensible, illustrative, and guiding video about RAI treatment in Turkish with English subtitles. In addition, similar videos may be prepared for other radionuclide treatments and diagnostic imaging procedures of nuclear medicine and can be delivered as QR codes to patients who applied to nuclear medicine clinics.

Ethics

Ethics Committee Approval: This study does not require an ethics committee.

Informed Consent: This study does not require patient consent.

Peer-review: Externally peer-reviewed.

Financial Disclosure: The author declared that this study has received no financial support.

References

1. O'Malley JP, Ziessman HA. Nuclear Medicine and Molecular Imaging: The Requisites e-book: Elsevier; 2020.
2. Verburg FA. Differentiated Thyroid Cancer: Radioiodine Therapy. In: Ahmadzadehfar H, Biersack H-J, Freeman LM, Zuckier LS, (eds). Clinical Nuclear Medicine. Cham: Springer International Publishing, 2020;831-844.
3. Dietlein M. Radioiodine Therapy for Benign Thyroid Disease. In: Ahmadzadehfar H, Biersack HJ, Freeman LM, Zuckier LS (eds). Clinical Nuclear Medicine. Cham: Springer International Publishing, 2020;815-829.
4. Ermert J, Benešová M, Hugenberg V, Gupta V, Spahn I, Pietzsch HJ, Liolios C, Kopka K. Radiopharmaceutical Sciences. Clin Nucl Med 2020; 49-191.
5. Aktolun C, Goldsmith SJ. Nuclear medicine therapy: principles and clinical applications: Springer Science & Business Media; 2012.
6. Haugen BR, Alexander EK, Bible KC, Doherty GM, Mandel SJ, Nikiforov YE, Pacini F, Randolph GW, Sawka AM, Schlumberger M, Schuff KG, Sherman SI, Sosa JA, Steward DL, Tuttle RM, Wartofsky L. 2015 American thyroid association management guidelines for adult patients with thyroid nodules and differentiated thyroid cancer: the American thyroid association guidelines task force on thyroid nodules and differentiated thyroid cancer. Thyroid 2016;26:1-133.
7. Ross DS, Burch HB, Cooper DS, Greenlee MC, Laurberg P, Maia AL, Rivkees SA, Samuels M, Sosa JA, Stan MN, Walter MA. 2016 American thyroid Association Guidelines for diagnosis and management of hyperthyroidism and other causes of thyrotoxicosis. Thyroid 2016;26:1343-1421. Erratum in: Thyroid 2017;27:1462.
8. Drozd B, Couvillon E, Suarez A. Medical YouTube videos and methods of evaluation: literature review. JMIR Med Educ 2018;4:e3.
9. Yoon H, Jang Y, Vaughan PW, Garcia M. Older adults' internet use for health information: digital divide by race/ethnicity and socioeconomic status. J Appl Gerontol 2020;39:105-110.

10. Kocyigit BF, Nacitarhan V, Koca TT, Berk E. YouTube as a source of patient information for ankylosing spondylitis exercises. Clin Rheumatol 2019;38:1747-1751.
11. Silberg WM, Lundberg GD, Musacchio RA. Assessing, controlling, and assuring the quality of medical information on the Internet: caveant lector et viewor–let the reader and viewer beware. JAMA 1997;277:1244-1245.
12. Charnock D, Shepperd S, Needham G, Gann R. DISCERN: an instrument for judging the quality of written consumer health information on treatment choices. J Epidemiol Community Health 1999;53:105-111.
13. Bernard A, Langille M, Hughes S, Rose C, Leddin D, Veldhuyzen van Zanten S. A systematic review of patient inflammatory bowel disease information resources on the World Wide Web. Am J Gastroenterol 2007;102:2070-2077.
14. Tolu S, Yurdakul OV, Basaran B, Rezvani A. English-language videos on YouTube as a source of information on self-administer subcutaneous anti-tumour necrosis factor agent injections. Rheumatol Int 2018;38:1285-1292.
15. Atkinson NL, Saperstein SL, Pleis J. Using the internet for health-related activities: findings from a national probability sample. J Med Internet Res 2009;11:e4.
16. Rutten LJ, Squiers L, Hesse B. Cancer-related information seeking: hints from the 2003 Health Information National Trends Survey (HINTS). J Health Commun 2006;11(Suppl 1):147-156.
17. Madathil KC, Rivera-Rodriguez AJ, Greenstein JS, Gramopadhye AK. Healthcare information on YouTube: a systematic review. Health Informatics J 2015;21:173-194.
18. YouTube at five- 2 bn views a day. London. http://news.bbc.co.uk/2/hi/technology/8676380.stm/
19. YouTube statistics. California. http://www.viralblog.com/research-cases/youtube-statistics/
20. Fox S. Online health search 2006. Pew Internet & American Life Project W, DC, October 2006.
21. Fox S, Purcell K. Chronic disease and the internet. Pew Internet & American Life Project W, DC, March 2010.
22. Fox S. The engaged e-patient population: people turn to the Internet for health information when the stakes are high and the connection fast. 2008 hwpo.
23. Fox S, Jones S. The social life of health information (Americans' pursuit of health takes place within a widening network of both online and offline sources). Pew Internet & American Life Project; California HealthCare Foundation, Washington, DC, 2009.

Original Article
Mol Imaging Radionucl Ther 2022;31:49-56 DOI:10.4274/mirt.galenos.2022.59140

Can Radiomics Analyses in ^{18}F-FDG PET/CT Images of Primary Breast Carcinoma Predict Hormone Receptor Status?

Meme Kanserinde Primer Tümöre Ait ^{18}F-FDG PET/BT Radiomics Parametreleri Hormon Reseptörleri Durumunu Öngörebilir mi?

Mine Araz[1], Çiğdem Soydal[1], Pınar Gündüz[1], Ayça Kırmızı[2], Batuhan Bakırarar[3], Serpil Dizbay Sak[2], Elgin Özkan[1]

[1]*Ankara University Faculty of Medicine, Department of Nuclear Medicine, Ankara, Turkey*
[2]*Ankara University Faculty of Medicine, Department of Pathology, Ankara, Turkey*
[3]*Ankara University Faculty of Medicine, Department of Biostatistics, Ankara, Turkey*

Abstract

Objectives: This study aimed to investigate the role of preoperative ^{18}fluorine-fluorodeoxyglucose (^{18}F-FDG) positron emission tomography/computed tomography (PET/CT) radiomics features and metabolic parameters of primary breast tumors in predicting hormone receptor (HR) positivity.

Methods: A total of 153 patients with breast carcinoma who underwent preoperative ^{18}F-FDG PET/CT were included. All PET/CT images were retrospectively reevaluated. Radiomics features of primary breast lesions reflecting tumor heterogeneity as well as standardized uptake value (SUV) metrics (SUV_{min}, SUV_{mean}, SUV_{max}, and SUV_{peak}) and volumetric parameters such as metabolic tumor volume and total lesion glycolysis (TLG) were extracted by commercial texture analysis software package (LIFEx; https://www.lifexsoft.org/ index.php). WEKA and SPSS were used for statistical analysis. Binary logistic regression analysis was used to determine texture features predicting HR positivity. Accuracy, F-measure, precision, recall, and precision-recall curve area were used as data-mining performance criteria of texture features to predict HR positivity.

Results: None of the radiomics parameters were significant in predicting HR status. Only SUV metrics and TLG were statistically important. Mean ± standard deviations for SUV_{mean}, SUV_{max}, and SUV_{peak} for the HR-negative group were significantly higher than those in the HR-positive group (6.73±4.36 vs. 5.20±3.32, p=0.027; 11.55±7.42 vs. 8.63±5.23, p=0.006; and 8.37±6.81 vs. 5.72±4.86; p=0.012). Cut-off values of SUV_{mean}, SUV_{max}, and SUV_{peak} for the prediction of HR positivity were 4.93, 8.35, and 6.02, respectively. Among data-mining methods, logistic regression showed the best performance with accuracy of 0.762.

Conclusion: In addition to the relatively limited number of patients in this study, radiomics parameters cannot predict the HR status of primary breast cancer. SUV levels of the HR-negative group were significantly higher than those of the HR-positive group. To clarify the role of metabolic and radiomics parameters in predicting HR status in breast cancer, further studies involving a larger study population are needed.

Keywords: Breast cancer, PET/CT, fluorodeoxyglucose, hormone receptor

Öz

Amaç: Bu çalışmanın amacı preoperative ^{18}flor-florodeoksiglukoz (^{18}F-FDG) pozitron emisyon tomografisi/bilgisayarlı tomografi (PET/BT) radiomics ve metabolik parametrelerinin primer meme tümörünün hormon reseptör (HR) pozitifliğini öngörmedeki rolünün araştırılmasıdır.

Yöntem: Preoperatif ^{18}F-FDG PET/BT yapılan 153 meme kanseri hastası dahil edildi. Tüm PET/BT görüntüleri retrospektif olarak yeniden değerlendirildi. Primer meme tümörünün tümör heterojenitesini yansıtan radiomics parametrelerinin yanında standardize alım değeri (SUV) ölçümleri (SUV_{min}, $SUV_{ortalama}$, SUV_{maks}, SUV_{peak}) ve volümetrik parametreler [metabolik tümör hacmi ve toplam lezyon glikoliz (TLG)] doku analizi yazılım programı (LIFEx) (https://www.lifexsoft.org/ index.php) ile çıkarıldı. İstatistiksel analiz için WEKA ve SPSS kullanıldı. HR pozitifliğini

Address for Correspondence: Mine Araz MD, Ankara University Faculty of Medicine, Department of Nuclear Medicine, Ankara, Turkey
Phone: +90 532 666 73 13 **E-mail:** minesoylu@yahoo.com ORCID ID: orcid.org/0000-0001-6467-618X
Received: 24.11.2021 **Accepted:** 11.01.2022

öngörülmesi için Binary lojistik regresyon analizi kullanıldı. Doğruluk, F-measure, kesinlik, recall ve precision-recall curve HR pozitifliğini öngörmede doku parametrelerinin veri madenciliği performans kriterleri olarak kullanıldı.

Bulgular: HR durumunun öngörülmesinde hiçbir radiomics parametresi anlamlı bulunmadı. Sadece SUV ölçümleri ve TLG anlamlı bulundu. HR negatif grupta pozitif gruba göre ortalama $SUV_{ortalama}$, SUV_{maks} and SUV_{peak} değerleri istatistiksel olarak yüksek bulundu (6,73±4,36'ya karşı 5,20±3,32 p=0,027, 11,55±7,42'ye karşı 8,63±5,23 p=0,006 ve 8,37±6,81'e karşı 5,72±4,86 p=0,012). $SUV_{ortalama}$, SUV_{maks} and SUV_{peak} için HR pozitifliğini öngörmede eşik değerler sırasıyla 4,93, 8,35 ve 6,02'ydi. Veri madenciliği yöntemleri içinde lojistik regresyon 0,762 doğruluk ile en iyi performansı gösterdi.

Sonuç: Bu çalışmada kısıtlı hasta sayısı olmakla birlikte, radiomics parametreleri primer meme kanserinde HR durumunu öngöremedi. HR negatif grupta, pozitif gruba göre SUV değerleri anlamlı olarak daha yüksekti. Metabolik parametrelerin ve radiomics parametrelerinin meme kanserinde HR durumunu öngörmedeki yerinin netleşebilmesi için daha fazla sayıda hasta içeren ileri çalışmalara ihtiyaç vardır.

Anahtar kelimeler: Meme kanseri, PET/BT, fluorodeoksiglukoz, hormon reseptörü

Introduction

Breast cancer is the most common cause of cancer-related deaths in women worldwide. Clinical outcome is closely related to the disease stage at diagnosis. Early diagnosis and appropriate therapy help achieve favorable outcome. However, breast cancer is a heterogeneous type of tumor with expression of several different receptors and many defined gene mutations. These characteristics at the subcellular micro level have been well investigated as molecular targets of various therapeutic approaches. Estrogen and progesterone receptor positivity is the most important prognostic factor in breast cancer. The existence and loss of hormone receptor (HR) expression have been investigated in the estimation of prognosis (1).

^{18}Fluorine-fluorodeoxyglucose (^{18}F-FDG) positron emission tomography/computed tomography (PET/CT), the most frequently used nuclear oncology method, is also recommended for staging locally advanced breast cancer, where the incidence of distant metastasis or the necessity for neoadjuvant chemotherapy is high. The use of PET radiomics in oncology has recently emerged as a new era of clinical investigation. High levels of maximum standardized uptake value (SUV_{max}) of the primary breast tumor have been associated with high grade and poor prognosis in breast carcinoma (2). Moreover, beyond SUV_{max}, certain features of intratumoral distribution, and volumetrics of ^{18}F-FDG, the most common tracer reflecting metabolic activity of the tumor has also been defined. Some of these features have been associated with the receptor status of breast cancer (3,4,5,6,7). However, these PET features do not reflect spatial intratumoral heterogeneity. Tumor heterogeneity is closely related with proliferation rate and necrosis (8). The era of artificial intelligence in medical imaging and determination of therapy according to individual automated risk classification systems and adopted algorithms has led to further trials in metabolic imaging.

Radiomics is a method of extracting several features from medical images. It uses data reconstruction algorithms to obtain parameters that cannot be recognized by raw data. First-order features refer to histogram analysis based on intensity. Second-order features consider relationships between gray level values within the volume of interest (VOI) and reflect intralesion heterogeneity like gray level co-occurrence matrix and gray level run-length matrix (GLRLM). Higher-order features are obtained statistically from filtered or mathematically transformed medical images. This helps noise suppression, highlighting repetitive patterns or reveal important details (9).

These parameters have been shown to be related with some clinical or histopathological characteristics of disease, in our case, breast cancer. Further processing of these data has also provided information about the prognosis and possible beneficial therapy options (10).

This study aimed to analyze metabolic and radiomics features of primary breast tumors of patients who underwent preoperative ^{18}F-FDG PET/CT and their correlation with histopathological HR status.

Material and Methods

Patients

Ankara University Human Research Ethics Committee approval was obtained (ethical approval no: I1-43-21).

After excluding 32 patients who received neoadjuvant chemotherapy before primary tumor excision, 153 consecutive patients who underwent preoperative ^{18}F-FDG PET/CT with biopsy-proven breast carcinoma in our department between July 2014 and March 2020 were included in the study. All patients underwent surgical excision of the primary tumor after ^{18}F-FDG PET/CT. Histopathological characteristics of the excised tumor were noted including the size, Ki-67 index, estrogen receptor (ER), and progesterone receptor (PR) status of the tumor.

The exclusion criteria were as follows: i) No significant solid lesion on CT (n=1), ii) existence of non-^{18}F-FDG-avid tumors (n=5), iii) uncontrolled diabetes with blood glucose level >150 mg/dL (n=3), iv) multiple primary cancer (n=2), v) unavailability of details of histopathological examination data (n=10), vi) total excision of the primary tumor before ^{18}F-FDG PET/CT (n=9), and vii) existence of primary tumor smaller than 64 voxels (n=12).

Histopathological Analysis

All cases were analyzed for ER and PR status and Ki-67 proliferation rate with immunohistochemical analysis. Immunohistochemical studies were performed with external and internal positive controls; the scattered nuclear positivity of ER and PR in normal breast ducts and acini around the tumor were used as internal positive controls. The percentage of the nuclear ER- and PR-positive invasive tumor cells was recorded. The percentage of at least 1% of the tumor cells reported as positive was recommended (11). The Ki-67 proliferation rate was counted in hotspot areas, where at least 100 tumor cells were counted, and the percentage of the nuclear Ki-67 positive tumor cells were reported (12).

^{18}F-FDG PET/CT Protocol

After 6 h of fasting, approximately 370 MBq ^{18}F-FDG was injected intravenously provided that the blood glucose level was <150 mg/dL. Whole-body PET/CT images were obtained by hybrid PET/CT scanner (Discovery ST or Discovery 710, GE Medical Systems, Milwaukee, USA) from the vertex to the upper thigh 60 min after radiopharmaceutical injection. PET scan was performed 3 min/bed position. Attenuation correction was performed by low-dose CT (140 kV, 70 mA, 0.5 s/tube rotation, and slice thickness of 5 mm). Patients were allowed to breathe normally. The maximum intensity projection and attenuation-corrected PET/CT fusion images were evaluated in three planes (transaxial, coronal, and sagittal) (Advance Workstation Volumeshare 5 GE Medical Systems).

Texture and Volumetric Analysis

Whole-body PET/CT images were retrospectively reevaluated by an experienced nuclear medicine specialist (with >10 years of experience on oncological PET/CT) blinded to all histopathological and clinical data of the case. PET parameters of primary breast lesions were measured. A threshold of 40% of the SUV_{max} used to define the contours of semi-automated VOIs drawn around the primary tumor. Forty-two radiomics features reflecting tumor heterogeneity (first-, second-, and higher-order texture parameters) as well as SUV metrics (SUV_{min}, SUV_{mean}, SUV_{max}, and SUV_{peak}) and metabolic volumetric parameters such as metabolic tumor volume (MTV) and total lesion glycolysis (TLG) were extracted from the PET/CT images imported in DICOM format by the commercial texture analysis software package (LIFEx; https://www.lifexsoft.org/ index.php).

VOIs on PET and CT images were identical. The resampling setup details for LIFEx were as follows: Intensity discretization with gray levels of 64 bins and intensity rescaling bound 0-20 for PET images and between -1000 and 3000 HU of gray levels of 400 bins and absolute scale bounds for CT images. The analyzed metabolic and radiomics parameters are listed in Table 1.

Statistical Analysis

WEKA 3.7 and SPSS 11.5 programs were used to evaluate the collected data. As descriptive statistics, the mean ± standard deviation and median (minimum-maximum) for quantitative variables and number of patients (percent) for qualitative variables were used. In terms of quantitative variable, a significant difference was found between the categories of the qualitative variables of HR-positive and HR-negative groups, and Mann-Whitney U test was used because the normal distribution assumptions were not met. Binary logistic regression analysis was used to determine the texture features affecting HR positivity. Receiver operating characteristic analysis was performed to determine the cut-off values for different texture features. The significance level was set as 0.05. Classification methods of support vector machine, Hoeffding tree, J48, and multilayer perceptron were used in the WEKA program. The data set was evaluated using the 10-fold cross-validation test option. Accuracy, F-measure, precision, recall, and precision-recall curve area were used as data-mining performance criteria of texture features to predict HR positivity.

Results

A total of 153 patients with locally advanced (stage IIA-III) breast cancer (150 female, 3 male, mean age 55.83±13.37 years) were enrolled. The mean tumor size was 39.92±22.83 (7-140) mm. No patients had T4 tumor (stage IIIB). The demographic characteristics of the patients are given in Table 2. In the final histopathological examination, tumors of 37 patients were negative for HRs.

The CorrelationAttributeEval method in WEKA and binary logistic regression analysis in SPSS were used because the data set contained numerous radiomics features. By using these methods, the importance of the features and their contributions to the data set were examined. The features that were determined to be insignificant by the two methods and considered not important as clinical

information were excluded from the data set. A total of seven features remained as a result. These features were SUV_{mean}, SUV_{max}, SUV_{peak}, gray level zone length matrix long-zone emphasis (GLZLM LZE), TLG, MTV, and GLRLM gray level non-uniformity (GLNU). Descriptions for these features for HR-positive and HR-negative groups are shown in Table 3. The mean ± standard deviations for the SUV_{mean}, SUV_{max}, and SUV_{peak} for the HR-negative group were significantly higher than that in the HR-positive group (6.73±4.36 vs. 5.20±3.32, p=0.027; 11.55±7.42 vs. 8.63±5.23, p=0.006; and 8.37±6.81 vs. 5.72±4.86, p=0.012). Cut-off values for the prediction of HR status for SUV_{mean}, SUV_{max}, and SUV_{peak} were calculated as 4.93, 8.35, and 6.02, respectively (Table 4). Percentages of feature importance according to the HR status were given in Figure 1. When we looked at the binary logistic regression analysis results to determine the risk factors affecting HR status in addition to SUVs, TLG demonstrated significant importance (Table 5). None of the radiomics parameters were found as significant factors to predict HR status. When comparing the data- mining performance results for different methods in Table 6, logistic regression gave the best accuracy with 0.762.

Table 1. List of the studied metabolic and radiomics parameters

Metabolic parameters	Higher-order parameters
SUV_{max}	GLRLM SRE
SUV_{mean}	GLRLM LRE
SUV_{peak}	GLRLM LGRE
MTV	GLRLM HGRE
TLG	GLRLM SRLGE
First-order parameters	GLRLM SRHGE
Skewness	GLRLM LRLGE
Kurtosis	GLRLM LRHGE
$Entropy_{histo}$	GLRLM GLNU
Energy	GLRLM RLNU
SHAPE sphericity	GLRLM RP
SHAPE compacity	GLZLM SZE
Second-order parameters	GLZLM LZE
$Homogenity_{GLCM}$	GLZLM LGZE
$Energy_{GLCM}$	GLZLM HGZE
$Contrast_{GLCM}$	GLZLM SZLGE
$Correlation_{GLCM}$	GLZLM SZHGE
$Entropy_{GLCM}$	GLZLM LZLGE
$Dissimilarity_{GLCM}$	GLZLM LZHGE
	GLZLM GLNU
	GLZLM ZLNU
	GLZLM ZP
	$Coarseness_{NGLDM}$
	$Contrast_{NGLDM}$
	$Busyness_{NGLDM}$

SUV: Standardized uptake value, MTV: Metabolic tumor volume, TLG: Total lesion glycolysis, GLCM: Gray level co-occurrence matrix, GLRLM: Gray level run-length matrix, SRE: Short-run emphasis, LRE: Long-run emphasis, LGRE: Low gray level run emphasis, HGRE: High gray level run emphasis, SRLGE: Short-run low gray level emphasis, SRHGE: Short-run high gray level emphasis, LRLGE: Long-run low gray level emphasis, LRHGE: Long-run high gray level emphasis, GLNU: Gray level non-uniformity, RP: Run percentage, GLZLM: Gray level zone length matrix, SZE: Short-zone emphasis, LZE: Level zone emphasis, LGZE: Low gray level zone emphasis, HGZE: High gray level zone emphasis, SZLGE: Short-zone low gray level emphasis, SZHGE: Short-zone high gray level emphasis, LZLGE: Long-zone low gray level emphasis, LZHGE: Long-zone high gray level emphasis, ZLNU: Zone length non-uniformity, ZP: Zone percentage, NGLDM: Neighborhood gray level different matrix

Discussion

Staging is not the only parameter that can guide therapy in breast cancer. Intratumoral heterogeneity is a challenging issue in the management of breast cancer. Various types of genetic alterations, receptor expressions, and sensitivity to certain hormones highly affect the biological behavior and the clinical course of the disease. Classification and

Table 2. Demographic characteristics of the patients

		Mean ± SD (minimum-maximum)
Age		55.83±13.37 (26-88)
Tumor size		39.92±22.83 (7-140 mm)
		Number of patients (%)
Stage	**IIA**	65 (43%)
	IIB	61 (40%)
	IIIA	14 (9%)
	IIIB	-
	IIIC	13 (8%)
Histopathology	**Ductal**	127 (83%)
	Lobular	12 (8%)
	Mucinous	3 (2%)
	Others	11 (7%)
	Micropapillary	1 (0.6%)
	Tubular + cribriform	1 (0.6%)
	Ductal + micropapillary	4 (2.6%)
	Ductal + micropapillary	4 (2.6%)
	Ductal + cribriform	1 (0.6%)
	Ductal + mucinous	
Hormone receptor status	**Positive**	116 (76%)
	Negative	37 (24%)

SD: Standard deviation

Table 3. Descriptives for hormone receptor status

Variables	HR status				
	Negative (n=37)		Positive (n=116)		
	Mean ± SD	Median (min-max)	Mean ± SD	Median (min-max)	p value
SUV_{mean}	6.73±4.36	6.09 (0.97-24.46)	5.20±3.32	4.44 (1.16-20.67)	0.027
SUV_{max}	11.55±7.42	10.58 (3.30-44.23)	8.63±5.23	7.11 (1.46-29.20)	0.006
SUV_{peak}	8.37±6.81	7.46 (0.00-37.44)	5.72±4.86	4.66 (0.00-26.08)	0.012
TLG	86.54±113.38	38.66 (2.79-462.25)	48.45±77.18	22.74 (1.71-599.65)	0.104
MTV	23.26±70.19	5.66 (0.51-419.68)	8.57±9.92	5.89 (0.83-64.81)	0.548
GLZLM LZE	1928.13±7411.88	5.85 (0.00-33375.38)	201.24±780.95	11.24 (0.00-6851.30)	0.196
GLRLM GLNU	50.55±136.04	9.33 (0.00-718.89)	21.39±31.95	12.94 (0.00-215.10)	0.656

HR: Hormone receptor, SD: Standard deviation, min: Minimum, max: Maximum, SUV: Standardized uptake value, TLG: Total lesion glycolysis, MTV: Metabolic tumor volume, GLZLM: Gray level zone length matrix, LZE: Level zone emphasis, GLRLM: Gray level run-length matrix, GLNU: Gray level non-uniformity

Table 4. Cut-off values for the SUV_{mean}, SUV_{max}, and SUV_{peak} in the prediction of hormone receptor status

Variables	Area	Standard error	p value	95% confidence interval		Sensitivity	Specificity	Cut-off value
				Lower bound	Upper bound			
SUV_{mean}	0.623	0.053	0.027	0.518	0.727	0.617	0.611	4.935
SUV_{max}	0.651	0.050	0.006	0.553	0.748	0.635	0.667	8.355
SUV_{peak}	0.638	0.053	0.012	0.534	0.743	0.6262	0.639	6.025

SUV: Standardized uptake value, max: Maximum

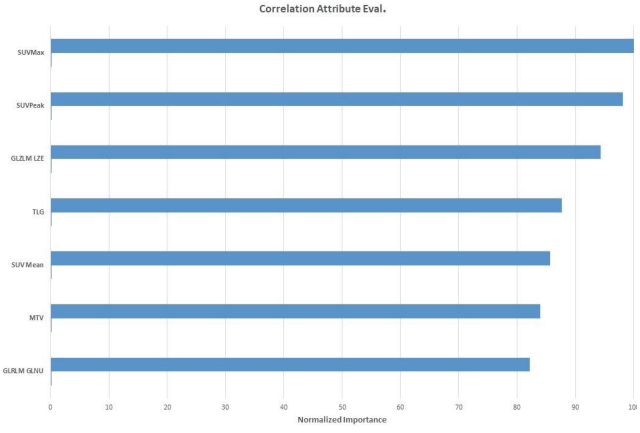

Figure 1. Variable importance for hormone receptor positivity

prognosis estimation is thus difficult because many factors are needed to consider. Breast cancers are dependent on estrogen and progesterone for growth; thus, receptor modulators and receptor downregulators are also used in the therapeutic management of disease other than conventional chemotherapy. ER and PR positivity is known as the most important prognostic factor in breast cancer. Hormonal therapy has been shown to be beneficial in overall survival and progression-free survival (13).

Imaging at diagnosis primarily aimed to correct cancer staging. However, in heterogeneous tumors like breast cancer, tumor size, local invasion, or disease extent is not enough for prognosis estimation and treatment decision. Any radiological or functional image obtained is actually more valuable than the reconstructed image, as huge amounts of processable data are hidden. Texture analysis include the parameters derived from the first-, second-, and higher-order statistics reflecting the entropy, skewness, curtosis, etc. (14). The radiomics parameters calculated from ^{18}F-FDG PET/CT have been reported to be related with molecular characteristics and outcome results in breast cancer (15).

SUV reflects the cellular content of the selected tumoral tissue. SUV_{max} is the most widely used parameter for the absolute quantification of activity concentration of the tumoral tissue in a selected voxel in proportion to the injected activity (16). SUV calculation assumes that the injected radiopharmaceutical is evenly distributed throughout the body. Thus, it is affected by various factors such as partial volume effect, motion, time interval between injection and acquisition, and reconstruction method (16,17,18). This is why the use of volumetric parameters like MTV and TLG has been recommended, which represent the tumoral load closest to real in a given tumoral lesion. Thus, they have been advocated to be more successful in estimating disease severity in various cancers, including breast cancer (19). However, in this study, we examined PET metabolic

Table 5. Binary logistic regression results for predicting hormone receptor status

Variables (reference)	β	SE	p value	OR	95% CI for OR	
					Lower bound	Upper bound
SUV_{max}	0.077	0.032	0.017	1.080	1.014	1.150
SUV_{peak}	0.082	0.035	0.018	1.086	1.014	1.163
GLZLM LZE	0.001	0.001	0.161	1.001	0.999	1.001
TLG	0.004	0.002	0.037	1.004	1.000	1.008
SUV_{mean}	0.106	0.050	0.035	1.112	1.007	1.227
MTV	0.020	0.014	0.165	1.020	0.992	1.048
GLRLM GLNU	0.005	0.003	0.103	1.005	0.999	1.011

β: Beta coefficient, SE: Standard error of mean, OR: Odds ratio, CI: Confidence interval, SUV: Standardized uptake value, max: Maximum, GLZLM: Gray level zone length matrix, LZE: Level zone emphasis, TLG: Total lesion glycolysis, MTV: Metabolic tumor volume, GLRLM: Gray level run-length matrix, GLNU: Gray level non-uniformity

Table 6. Comparison of the performance of data-mining methods

Methods	Accuracy	F-measure	Precision	Recall	PRC area
Support vector machine	0.762	0.659	0.581	0.761	0.629
Logistic regression	0.762	0.690	0.709	0.760	0.652
Multilayer perceptron	0.748	0.663	0.643	0.745	0.655

PRC: Precision-recall curve

and radiomic features of the primary breast lesion only and investigated its relationship with the hormonal status of the tumor. All SUV parameters, including maximum, peak, and mean SUV were factors related with HR status. Interestingly, and in contrast to previously mentioned hypothesis that volumetric parameters are more reliable, MTV was not significant. However, TLG, the calculated product of MTV and SUV_{mean} of the target lesion, was also significantly related with the HR status in patients with breast cancer. We attributed the difference between the significance level of MTV and TLG to the fact that TLG is eventually a derivative of SUV already. These results are compatible with those of a previous study (20). A study on patients with breast cancer who have undergone positron emission mammography (PEM) deserves attention because the authors presented PET data dedicated to breast. In contrast to many other studies, they proposed that volumetric data are not of significant importance and SUV is predictive of hormonal status of the tumor (4).

The dataset contains many radiomics features. Thus, according to WEKA and binary logistic regression analysis, among radiomics parameters, only GLZLM LZE and GLRLM GLNU were included. GLZLM reflects the size of the homogenous zones for each gray level in three dimensions, and LZE is the distribution of the long homogenous zones in an image. GLRLM is used for the size of homogenous runs for each gray level in three dimensions, and GLNU measures the similarity of values of the gray level. In this study, none of the radiomics parameters were significant in predicting HR status. However, previous reports on radiomics and molecular characteristics of primary breast cancer have mostly studied multiple histopathological and clinical parameters including the tumor type (ductal/lobular), tumor size, Her-2 status, Ki-67 index, and TNM stage along with the HR status. Binary logistic regression analysis and risk estimation were the primary endpoints in these studies. However, in the present study, we used data-mining method, a higher-order and more complicated statistical method than methods used in previous studies. After determining the variables indicative of HR status by binary logistic regression analysis, we created a data-mining model that can accurately select patients with positive HR status using data obtained from ^{18}F-FDG PET/CT by utilizing the least number of features. Attempts to define quantitative features indicative of an event or characteristic of a lesion in radiological studies all serve as preliminary studies for modeling methods to be used in artificial intelligence. Studies have used various radiomics features to define HR status. However, if a program is created to determine histopathological characteristics of tumor based on ^{18}F-FDG PET/CT study for disease staging, only a few features will be needed to create a model (21). This is why we moved one step forward in statistics compared with previous studies. We investigated the importance level of variables determined by logistic regression and generated the best model for the prediction of HR status of primary breast cancer lesions using data from ^{18}F-FDG PET/CT performed for staging. In addition to risk estimation

calculated by binary logistic regression, the proposed PET radiomics model including metabolic parameters can also distinguish hormone-positive from hormone-negative breast cancer with a prediction accuracy of 76%. Because data-mining methods necessitate an incredible amount of data to be processed statistically, only HR status was examined under the scope of this study.

Despite the high-level statistics conducted in a large patient population for the estimation of a very specific condition in this study, there are a few limitations necessary to mention. First, the hormone-negative group was relatively small compared with the hormone-positive group. If a greater number of patients could be included, some radiomics parameters would have been significant together with metabolic parameters. We had to exclude many patients because of faint ^{18}F-FDG uptake and/or small breast tumors. If the same patients could be scanned with PEM or with PET/magnetic resonance (MR), some lesions may have been clarified, and these patients could have been enrolled in the study. However, PET/CT is the standard of choice in staging breast cancer because it provides data of the M status of the disease (22). PEM or PET/MR is rather used for further evaluation of local invasion or involvement of axillary lymph nodes. Radiomics data of PEM or PET/MR would also be certainly very valuable in predicting histopathological characteristics of primary breast cancer.

Conclusion

In addition to the relatively limited number of patients in this study, radiomics parameters cannot predict HR status of primary breast cancer. SUV levels of the HR-negative group were significantly higher than those in the HR-positive group. To clarify the role of metabolic and radiomics parameters in predicting HR status in breast cancer, further studies with a larger number of patients are needed.

Ethics

Ethics Committee Approval: Ankara University Human Research Ethics Committee approval was obtained (ethical approval no: I1-43-21).

Informed Consent: Was taken.

Peer-review: Externally peer-reviewed.

Authorship Contributions

Concept: Ç.S., M.A., Design: Ç.S., M.A., S.D.S., E.Ö., Data Collection or Processing: P.G., Ç.S., A.K., Analysis or Interpretation: B.B., Ç.S., Literature Search: M.A., Ç.S., Writing: M.A.

Conflict of Interest: No conflict of interest was declared by the authors.

Financial Disclosure: The authors declared that this study has received no financial support.

References

1. Harvey JM, Clark GM, Osborne CK, Allred DC. Estrogen receptor status by immunohistochemistry is superior to the ligand-binding assay for predicting response to adjuvant endocrine therapy in breast cancer. J Clin Oncol 1999;17:1474-1481.
2. Yoon HJ, Kim Y, Kim BS. Intratumoral metabolic heterogeneity predicts invasive components in breast ductal carcinoma in situ. Eur Radiol 2015;25:3648-3658.
3. Garcia-Vicente AM, Pérez-Beteta J, Pérez-García VM, Molina D, Jiménez-Londoño GA, Soriano-Castrejón A, Martínez-González A. Metabolic tumor burden assessed by dual time point [18F]FDG PET/CT in locally advanced breast cancer: relation with tumor biology. Mol Imaging Biol 2017;19:636-644.
4. Moscoso A, Ruibal Á, Domínguez-Prado I, Fernández-Ferreiro A, Herranz M, Albaina L, Argibay S, Silva-Rodríguez J, Pardo-Montero J, Aguiar P. Texture analysis of high-resolution dedicated breast 18 F-FDG PET images correlates with immunohistochemical factors and subtype of breast cancer. Eur J Nucl Med Mol Imaging 2018;45:196-206.
5. Ha S, Park S, Bang JI, Kim EK, Lee HY. Metabolic radiomics for pretreatment 18F-FDG PET/CT to characterize locally advanced breast cancer: histopathologic characteristics, response to neoadjuvant chemotherapy, and prognosis. Sci Rep 2017;7:1556.
6. Antunovic L, Gallivanone F, Sollini M, Sagona A, Invento A, Manfrinato G, Kirienko M, Tinterri C, Chiti A, Castiglioni I. [18F]FDG PET/CT features for the molecular characterization of primary breast tumors. Eur J Nucl Med Mol Imaging 2017;44:1945-1954.
7. Acar E, Turgut B, Yiğit S, Kaya G. Comparison of the volumetric and radiomics findings of 18F-FDG PET/CT images with immunohistochemical prognostic factors in local/locally advanced breast cancer. Nucl Med Commun 2019;40:764-772.
8. Molina-García D, García-Vicente AM, Pérez-Beteta J, Amo-Salas M, Martínez-González A, Tello-Galán MJ, Soriano-Castrejón Á, Pérez-García VM. Intratumoral heterogeneity in 18F-FDG PET/CT by textural analysis in breast cancer as a predictive and prognostic subrogate. Ann Nucl Med 2018;32:379-388.
9. Lambin P, Rios-Velazquez E, Leijenaar R, Carvalho S, van Stiphout RG, Granton P, Zegers CM, Gillies R, Boellard R, Dekker A, Aerts HJ. Radiomics: extracting more information from medical images using advanced feature analysis. Eur J Cancer 2012;48:441-446.
10. Gillies RJ, Kinahan PE, Hricak H. Radiomics: images are more than pictures, they are data. Radiology 2016;278:563-577.
11. Allison KH, Hammond MEH, Dowsett M, McKernin SE, Carey LA, Fitzgibbons PL, Hayes DF, Lakhani SR, Chavez-MacGregor M, Perlmutter J, Perou CM, Regan MM, Rimm DL, Symmans WF, Torlakovic EE, Varella L, Viale G, Weisberg TF, McShane LM, Wolff AC. Estrogen and progesterone receptor testing in breast cancer: ASCO/CAP guideline update. J Clin Oncol 2020;38:1346-1366.
12. Røge R, Nielsen S, Riber-Hansen R, Vyberg M. Ki-67 proliferation index in breast cancer as a function of assessment method: a NordiQC experience. Appl Immunohistochem Mol Morphol 2021;29:99-104.
13. Pertschuk LP, Kim DS, Nayer K, Feldman JG, Eisenberg KB, Carter AC, Rong ZT, Thelmo WL, Fleisher J, Greene GL. Immunocytochemical estrogen and progestin receptor assays in breast cancer with monoclonal antibodies. Histopathologic, demographic, and biochemical correlations and relationship to endocrine response and survival. Cancer 1990;66:1663-1670.
14. Mayerhoefer ME, Materka A, Langs G, Häggström I, Szczypiński P, Gibbs P, Cook G. Introduction to radiomics. J Nucl Med 2020;61:488-495.
15. Lemarignier C, Martineau A, Teixeira L, Vercellino L, Espié M, Merlet P, Groheux D. Correlation between tumour characteristics, SUV measurements, metabolic tumour volume, TLG and textural features assessed with 18F-FDG PET in a large cohort of oestrogen

receptor-positive breast cancer patients. Eur J Nucl Med Mol Imaging 2017;44:1145-1154.

16. Thie JA. Understanding the standardized uptake value, its methods, and implications for usage. J Nucl Med 2004;45:1431-1434.
17. Nakamoto Y, Zasadny KR, Minn H, Wahl RL. Reproducibility of common semi-quantitative parameters for evaluating lung cancer glucose metabolism with positron emission tomography using 2-deoxy-2-[18F] fluoro-D-glucose. Mol Imaging Biol 2002;4:171-178.
18. Keyes JW Jr. SUV: standard uptake or silly useless value? J Nucl Med 1995;36:1836-1839.
19. Moon SH, Hyun SH, Choi JY. Prognostic significance of volume-based PET parameters in cancer patients. Korean J Radiol 2013;14:1-12.
20. Sollini M, Cozzi L, Ninatti G, Antunovic L, Cavinato L, Chiti A, Kirienko M. PET/CT radiomics in breast cancer: mind the step. Methods 2021;188:122-132.
21. Hua J, Xiong Z, Lowey J, Suh E, Dougherty ER. Optimal number of features as a function of sample size for various classification rules. Bioinformatics 2005;21:1509-1515.
22. AJCC (American Joint Committee on Cancer) Cancer Staging Manual; 8th edition, 3rd printing, Amin MB, Edge SB, Greene FL, et al (Eds), Springer, Chicago 2018.

Interesting Image
Mol Imaging Radionucl Ther 2022;31:57-59 DOI:10.4274/mirt.galenos.2021.27147

^{18}F-Fluorodeoxyglucose Positron Emission Tomography/Magnetic Resonance Imaging Appearance of Gastrointestinal Behcet's Disease

Gastrointestinal Behçet Hastalığının ^{18}F-Florodeoksiglukoz Pozitron Emisyon Tomografisi/ Manyetik Rezonans Görüntüleme Bulguları

Burak İnce[1], Ali Kibar[1], Sertaç Asa[1], Rabia Lebriz Uslu Beşli[1], Muhammet Sait Sağer[1], Ahmet Emre Eşkazan[2], Ali İbrahim Hatemi[3], Gülen Hatemi[4], Kerim Sönmezoğlu[1]

[1]*İstanbul University-Cerrahpaşa, Cerrahpaşa Faculty of Medicine, Department of Nuclear Medicine, İstanbul, Turkey*
[2]*İstanbul University-Cerrahpaşa, Cerrahpaşa Faculty of Medicine, Department of Internal Medicine, Division of Hematology, İstanbul, Turkey*
[3]*İstanbul University-Cerrahpaşa, Cerrahpaşa Faculty of Medicine, Department of Internal Medicine, Division of Gastroenterology, İstanbul, Turkey*
[4]*İstanbul University-Cerrahpaşa, Cerrahpaşa Faculty of Medicine, Department of Internal Medicine, Division of Rheumatology, İstanbul, Turkey*

Abstract

Behcet's syndrome (BS) is a variable vessel vasculitis with multi-organ involvement. Recurrent episodes of oral and genital ulcers, papulopustular and erythema nodosum-like skin lesions, and arthritis are relatively more frequent, whereas uveitis, venous and arterial lesions, nervous system, and gastrointestinal involvement are less common, but are severe manifestations. The frequency of gastrointestinal involvement shows important variation between countries as more common in the Far East and the United States, and much less common in Turkey and the Middle East. The main clinical signs of gastrointestinal Behcet's disease include abdominal pain, diarrhea, blood in the stool, fever, and weight loss. Ulcers seen in the terminal ileum, cecum, and ascending colon are common endoscopic findings. Herein, we presented the positron emission tomography/ magnetic resonance imaging findings of gastrointestinal involvement in BS.

Keywords: Gastrointestinal Behcet's disease, Behcet syndrome, myelodysplastic syndromes, monosomy 7, acute myeloid leukemia, ^{18}F-FDG, PET scan, MRI

Öz

Behçet sendromu (BS) multi-organ tutulumu ile seyreden bir değişken damar vaskülitidir. Tekrarlayan oral ve genital ülserler, papülopüstüler ve eritema nodozum benzeri deri lezyonları ve artrit epizodları nispeten daha sık görülürken, üveit, venöz ve arteriyel lezyonlar, sinir sistemi tutulumu ve gastrointestinal tutulum daha az yaygın olmakla birlikte şiddetli belirtilerdir. Gastrointestinal tutulum sıklığı ülkeler arasında farklılık göstermekte olup, Uzak Doğu ve Amerika Birleşik Devletleri'nde daha sık görülürken, Türkiye ve Orta Doğu'da daha nadir görülmektedir. Gastrointestinal Behçet hastalığının başlıca klinik bulguları karın ağrısı, ishal, kanlı dışkılama, ateş ve kilo kaybıdır. Terminal ileum, çekum ve çıkan kolonda görülen ülserler ise sık görülen endoskopik bulgulardır. Bu olgu sunumunda, gastrointestinal BS'nin, daha önce yayınlanmamış, pozitron emisyon tomografisi/ manyetik rezonans görüntüleme bulgularını göstermeyi hedefliyoruz.

Anahtar kelimeler: Gastrointestinal Behçet hastalığı, Behçet sendromu, myelodisplastik sendrom, monozomi 7, akut myeloid lösemi, ^{18}F-FDG, PET tarama, MRG

Address for Correspondence: Burak İnce MD, İstanbul University-Cerrahpaşa, Cerrahpaşa Faculty of Medicine, Department of Nuclear Medicine, İstanbul, Turkey
Phone: +90 212 414 30 00 **E-mail:** burak.ince.91@istanbul.edu.tr ORCID ID: orcid.org/0000-0003-2225-5349
Received: 11.11.2020 **Accepted:** 17.01.2021

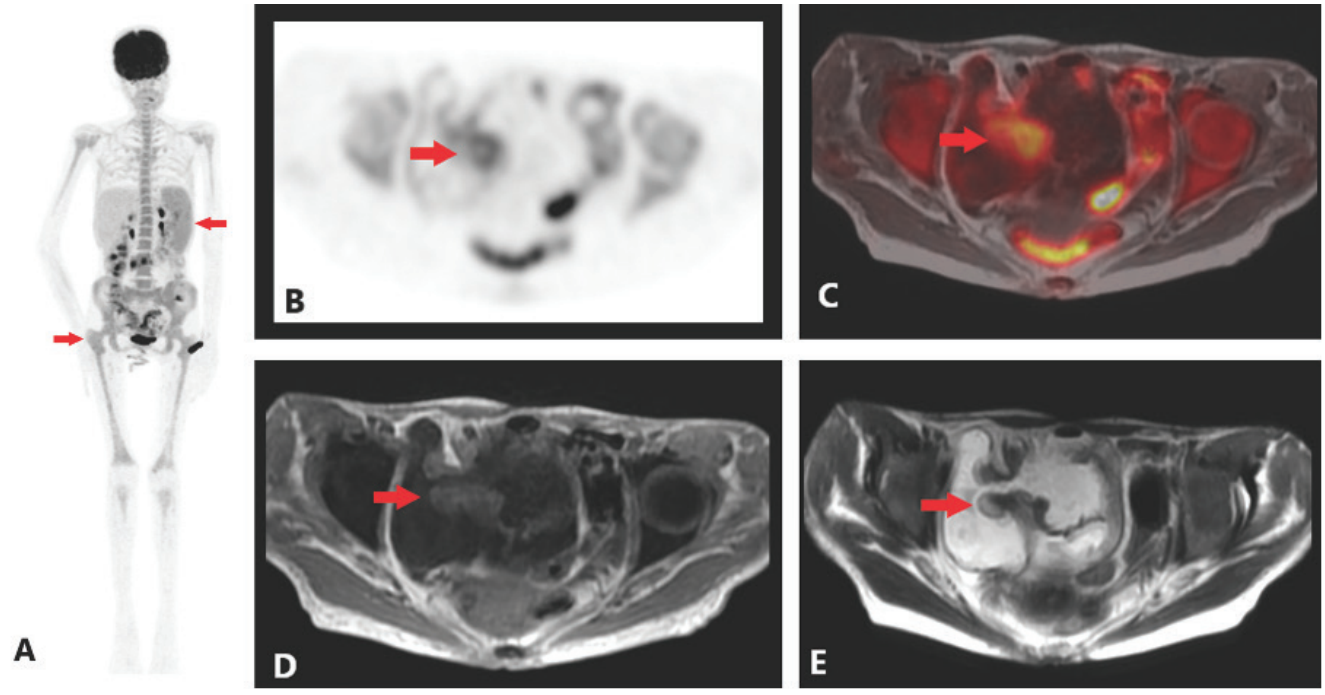

Figure 1. Behcet's syndrome (BS) is a variable vessel vasculitis with multi-organ involvement. The pathogenesis is unclear; however, genetic factors, as well as environmental factors, are thought to play a role. Human leukocyte antigen B51 allele in major histocompatibility complex locus is the best-known genetic risk factor for BS (1). It is a multi-system disease with recurrent episodes of oral and genital ulcers, papulopustular and nodular skin lesions, arthritis, uveitis, venous and arterial thromboses, arterial aneurysm, and nervous system involvement (1). According to different studies, gastrointestinal involvement occurs 4.5-6 years after the onset of oral ulcers. The frequency of gastrointestinal involvement was reported as high as 50% in the Far East, whereas approximately 1-1.5% in Turkey (2,3). The ileocolonic site is the most frequent disease localization in the gastrointestinal system (4). BS diagnosis is based on clinical manifestations, as there are no pathognomonic laboratory tests (1). However, endoscopic confirmation of typical ulcers is necessary for gastrointestinal involvement diagnosis in a patient with BS, since relying solely on clinical manifestations, such as abdominal pain and diarrhea, may be misleading. Inflammatory bowel diseases, especially Crohn's disease, and tuberculosis should be ruled out for the differential diagnosis of gastrointestinal involvement of BS (5). Medical treatment including 5-aminosalicylic acid, corticosteroids, immunosuppressive drugs, such as azathioprine, and monoclonal tumor necrosis factor-alpha inhibitors are commonly used, and surgery is generally reserved for patients who present with emergencies, such as major bleeding or perforation (6).

A 25-year-old female patient who was treated for BS, familial Mediterranean fever and myelodysplastic syndrome (MDS), and secondary acute myeloid leukemia (sAML) was referred to our center for [18]fluorine-fluorodeoxyglucose ([18]F-FDG) positron emission tomography (PET) imaging. She was diagnosed with gastrointestinal involvement of BS 3 years ago, after a colonoscopic examination for abdominal pain, weight loss, diarrhea, and mucus in the stool. Her colonoscopy revealed multiple colonic and ileocecal ulcers. Her abdominal pain, diarrhea, and elevated acute phase reactants continued despite treatment with colchicine, high dose prednisolone, thalidomide, and monoclonal TNF inhibitors. Abdominal imaging studies, which were performed due to fever, in addition to these findings, revealed a collection between the bladder and intestine. She was operated and a part of her ileum, as well as the bladder, was removed. Pathologic examination showed active chronic enteritis with multiple ulcers that extend to the subserosa in the small intestine. Additionally, lymphoplasmacytic cell infiltration, vascular proliferation, fresh thrombi, and medial calcifications in some vessels were observed in the submucosa, muscularis propria, and subserosa. The patient then developed pancytopenia and was diagnosed as MDS with positive monosomy 7 and negative trisomy 8. During the follow-up, she progressed to sAML. The association of MDS and AML with gastrointestinal involvement is an interesting and well-documented entity (7,8). [18]F-FDG PET/magnetic resonance imaging (MRI) was performed. [18]F-FDG PET maximum intensity projection (A) image revealed diffuse hypermetabolism on the bone marrow and hypermetabolism associated with splenomegaly, which was related to AML-M4. Axial PET (B), fused PET/T1-weighted (T1W) MRI (C), T1W MRI (D), and T2-weighted MRI (E) images revealed segmental dilatation and hypermetabolic wall thickening around the ileocecal valve (maximum standard uptake value: 6.23), which followed gastrointestinal involvement of BS. To our knowledge, this is the first case of intestinal BS with [18]F-FDG PET/MRI.

Ethics

Informed Consent: Was obtained from the patient.

Peer-review: Externally and internally peer-reviewed.

Authorship Contributions

Concept: M.S.S., R.L.U.B., S.A., Design: M.S.S., R.L.U.B., K.S., Data Collection or Processing: B.İ., A.K., S.A., Literature Search: B.İ., A.K., S.A., Writing: B.İ., A.K., R.L.U.B., A.E.E., A.İ.H., G.H.

Conflict of Interest: No conflict of interest was declared by the authors.

Financial Disclosure: The authors declared that this study received no financial support.

References

1. Yazici H, Seyahi E, Hatemi G, Yazici Y. Behçet syndrome: a contemporary view. Nat Rev Rheumatol 2018;14:107-119. Erratum in: Nat Rev Rheumatol 2018;14:119.
2. Lopalco G, Rigante D, Venerito V, Fabiani C, Franceschini R, Barone M, Lapadula G, Galeazzi M, Frediani B, Iannone F, Cantarini L. Update on the medical management of gastrointestinal Behçet's disease. In Mediators of Inflammation 2017. doi: 10.1155/2017/1460491.
3. Hatemi I, Hatemi G, Çelik AF. Gastrointestinal Involvement in Behçet Disease. Rheum Dis Clin North Am 2018;44:45-64.
4. Lee CR, Kim WH, Cho YS, Kim MH, Kim JH, Park IS, Bang D. Colonoscopic findings in intestinal Behçet's disease. Inflammatory Bowel Diseases 2001;7:243-249.
5. Lee HJ, Cheon JH. Optimal diagnosis and disease activity monitoring of intestinal Behçet's disease. Intest Res 2017;15:311-317.
6. Hatemi G, Christensen R, Bang D, Bodaghi B, Celik AF, Fortune F, Gaudric J, Gul A, Kötter I, Leccese P, Mahr A, Moots R, Ozguler Y, Richter J, Saadoun D, Salvarani C, Scuderi F, Sfikakis PP, Siva A, Stanford M, Tugal-Tutkun I, West R, Yurdakul S, Olivieri I, Yazici H. 2018 update of the EULAR recommendations for the management of Behçet's syndrome. Ann Rheum Dis 2018;77:808-818.
7. Yilmaz U, Ar MC, Esatoglu SN, Bavunoglu I, Erzin YZ, Hatemi AI, Yildirim S, Hatemi G, Celik AF. How to treat myelodysplastic syndrome with clinical features resembling Behçet syndrome: a case-based systematic review. Ann Hematol 2020;99:1193-1203.
8. Matsumoto Y, Ota K, Yamada H. Gastrointestinal: intestinal Behçet's disease-like ulcers associated with myelodysplastic syndrome with monosomy 7. J Gastroenterol Hepatol 2019;34:310.

Interesting Image
Mol Imaging Radionucl Ther 2022;31:60-62 DOI:10.4274/mirt.galenos.2020.78800

Superscan Appearance of ^{68}Ga PSMA PET/CT in a Patient with Refractory Prostate Cancer

Refrakter Bir Prostat Karsinomu Olgusunun ^{68}Ga PSMA PET/BT'de Superscan Görünümü

Zehra Pınar Koç[1], Pınar Pelin Özcan[1], Vehbi Erçolak[2], Mehmet Reyhan[3]

[1]*Mersin University Faculty of Medicine, Department of Nuclear Medicine, Mersin, Turkey*
[2]*Mersin University Faculty of Medicine, Department of Oncology, Mersin, Turkey*
[3]*Başkent University Faculty of Medicine, Department of Nuclear Medicine, Adana, Turkey*

Abstract

A 64-year-old male patient with metastatic prostate carcinoma diagnosis received lutetium-177 prostate-specific membrane antigen (PSMA) treatment; however, his disease progressed. Herein, presented the final images of the patient that demonstrated a superscan appearance in the Gallium-68 PSMA positron emission tomography/computed tomography, which is a rare phenomenon.

Keywords: PSMA, ^{68}Ga, Lu-177, prostate cancer

Öz

Altmış dört yaşında erkek hasta metastatik prostat karsinomu tanısıyla lutesyum-177 prostat spesifik membran antijeni (PSMA) tedavisi almış ancak hastalığı progresyon göstermiştir. Bu sunumda bu hastanın nadir bir fenomen olan superscan görünümü oluşturan Galyum-68 PSMA pozitron emisyon tomografisi/bilgisayarlı tomografi görüntülerini paylaşmak istiyoruz.

Anahtar kelimeler: PSMA, ^{68}Ga, Lu-177, prostat karsinomu

Address for Correspondence: Zehra Pınar Koç MD, Mersin University Faculty of Medicine, Department of Nuclear Medicine, Mersin, Turkey
Phone: +90 324 241 00 00 **E-mail:** zehrapinarkoc@gmail.com ORCID ID: orcid.org/0000-0002-3274-5790
Received: 17.02.2020 **Accepted:** 17.09.2020

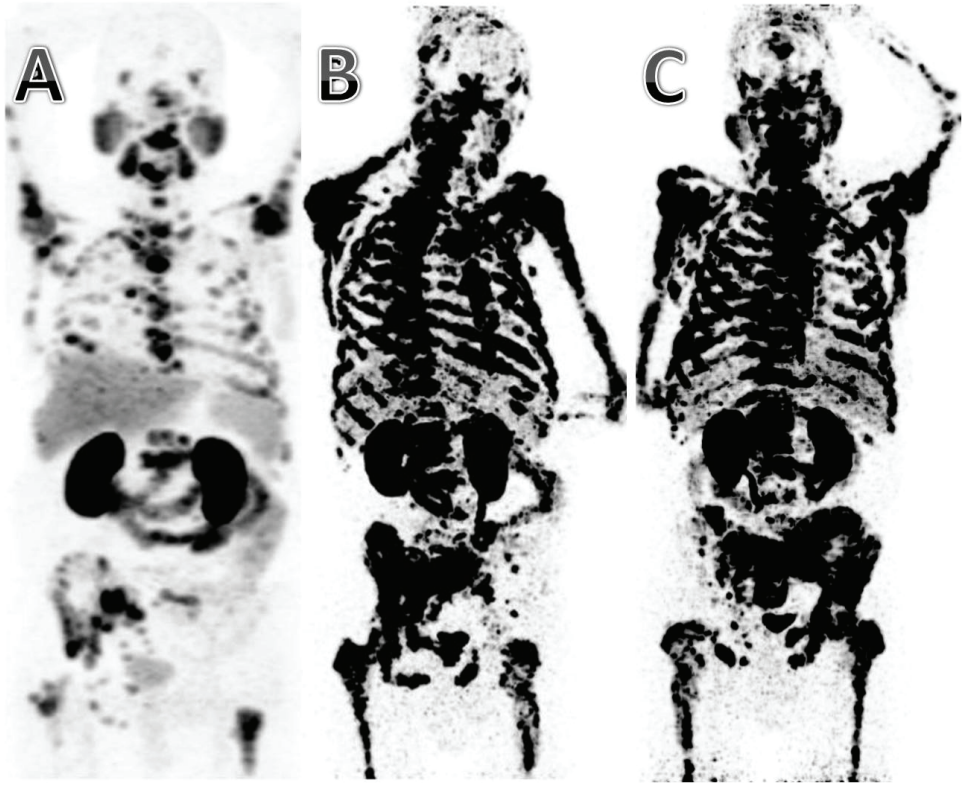

Figure 1. (A) A 64-year-old male patient with metastatic prostate carcinoma was subjected to Gallium-68 (^{68}Ga) prostate-specific membrane antigen (PSMA) positron emission tomography/computed tomography (PET/CT). The imaging was performed 60 min after intravenous administration of 5 mCi (435 mBq) Ga-68 PSMA in the craniocaudal direction in three-dimensional acquisition mode and 1 min per bed position with nondiagnostic CT scan for the attenuation correction. The ^{68}Ga PSMA imaging demonstrated disseminated disease involvement of the bone-bone marrow and multiple lymph nodes. The patient received multiple cycles of lutetium-177 (Lu-177) PSMA treatment. The patient had refractory disease, and 1 month after the last Lu-177 treatment, he was referred for the ^{68}Ga PSMA PET/CT for treatment response evaluation. Bilateral cervical, supraclavicular, axillary, mediastinal, and abdominal lymph nodes, pleural lesions, and bone-bone marrow infiltration were observed with significantly increased activity accumulation without non-lesion uptake except kidney and faint liver-spleen activity [(C, D) maximum intensity projection image of the ^{68}Ga PSMA PET/CT in the anterior and posterior projection, respectively].

Previous investigations demonstrated that superscan appearance is a consequence of the proportionally significantly increased metastatic lesions compared to normal tissues. Superscan was previously described in bone scintigraphy imaging, which is not a rare phenomenon for bone scintigraphy (1). However, this phenomenon is rare for ^{18}fluorine-fluorodeoxyglucose (^{18}F-FDG) PET/CT imaging (2,3,4,5). Only a few case reports were reported for the PET/CT with ^{68}Ga labeled radiopharmaceuticals. Chan and Schembri (6) reported a case presentation of both ^{68}Ga DOTATATE and ^{18}F-FDG PET/CT superscan. Another case report has demonstrated both bone scintigraphy and meta-iodobenzylguanidine superscan in the same patient (7). The only case report of skeletal superscan appearance in the ^{68}Ga PSMA PET/CT was presented by Agarwal et al. (8). To the best of our knowledge, this is the only report of a case with lymph nodes and skeletal superscan appearance in the ^{68}Ga PSMA imaging.

Ethics

Informed Consent: The informed consent of the patient was obtained.

Peer-review: Externally peer-reviewed.

Authorship Contributions

Surgical and Medical Practices: Z.P.K., P.P.Ö., V.E., M.R., Concept: Z.P.K., P.P.Ö., Design: Z.P.K., P.P.Ö., Data Collection or Processing: Z.P.K., P.P.Ö., V.E., M.R., Analysis or Interpretation: Z.P.K., P.P.Ö., V.E., M.R., Literature Search: Z.P.K., P.P.Ö., Writing: Z.P.K., P.P.Ö.

Conflict of Interest: No conflict of interest was declared by the authors.

Financial Disclosure: The authors declared that this study received no financial support.

References

1. Kim SE, Kim DY, Lee DS, Chung JK, Lee MC, Koh CS. Absent or faint renal uptake on bone scan. Etiology and significance in metastatic bone disease. Clin Nucl Med 1991;16:545-549.
2. Kim DW, Kim CG, Park SA, Jung SA, Yang SH. Metabolic super scan in F-FDG PET/CT imaging. J Korean Med Sci 2010;25:1256-1257.

3. Bailly M, Besse H, Kerdraon R, Metrard G, Gauvain S. 18F-FDG PET/CT superscan in prostate cancer. Clin Nucl Med 2014;39:912-914.
4. Parida GK, Soundararajan R, Passah A, Bal C, Kumar R. Metabolic Skeletal superscan on 18F-FDG PET/CT in a case of acute lymphoblastic leukemia. Clin Nucl Med 2015;40:567-568.
5. Grellier JF, Lussato D, Queneau M, Guernou M, Songy B. Secondary hyperparathyroidism with "superscan-like" hypermetabolic FDG PET/CT pattern. Clin Nucl Med 2015;40:888-889.
6. Chan M, Schembri GP. Combined 18F-FDG PET/CT and 68Ga DOTATATE PET/CT "superscan" in metastatic pancreatic neuroendocrine tumor. Clin Nucl Med 2017;42:108-109.
7. Tan TH, Wong TH, Hassan SZ, Lee BN. Unusual bone superscan, MIBG superscan, and 68Ga DOTATATE PET/CT in metastatic pheochromocytoma. Clin Nucl Med 2015;40:867-868.
8. Agarwal KK, Tripathi M, Kumar R, Bal C. Metastatic superscan in prostate carcinoma on gallium-68-prostate-specific membrane antigen positron emission tomography/computed tomography scan. Indian J Nucl Med 2016;31:150-151.

Interesting Image
Mol Imaging Radionucl Ther 2022;31:63-65 DOI:10.4274/mirt.galenos.2020.36035

Myocardial Ischemia on MPI SPECT in a Patient with Acute Myeloid Leukemia Without Significant Coronary Artery Disease

Ciddi Koroner Arter Hastalığı Olmayan Akut Miyeloid Lösemili Bir Hastada MPI SPECT'de Miyokard İskemisi

Chrissa Sioka[1], Aris Bechlioulis[2], Evangelos Ntais[3], Andreas Fotopoulos[1], Sotirios Giannopoulos[3], Eleni Kapsali[4], Christos Katsouras[2]

[1]*University Hospital of Ioannina, Department of Nuclear Medicine, Ioannina, Greece*
[2]*University Hospital of Ioannina, Department of Cardiology, Ioannina, Greece*
[3]*University Hospital of Ioannina, Department of Neurology, Ioannina, Greece*
[4]*University Hospital of Ioannina, Department of Hematology, Ioannina, Greece*

Abstract

Herein, we report the case of a 56-year-old male patient with acute myeloid leukemia (AML) in remission who had asymptomatic myocardial ischemia on myocardial perfusion imaging and transthoracic echocardiography. Angiography did not reveal any significant coronary artery disease. Although the etiology is not entirely clear, this case suggested that myocardial perfusion imaging should be considered in patients with AML who received idarubicin to screen for possible myocardial dysfunction.

Keywords: Acute myeloid leukemia, myocardial ischemia, myocardial perfusion imaging, echocardiography, angiography, coronary artery disease

Öz

Bu çalışmada, miyokard perfüzyon görüntüleme ve transtorasik ekokardiyografide asemptomatik miyokard iskemisi saptanan, remisyondaki akut miyeloid lösemili (AML) 56 yaşında bir erkek hastayı sunuyoruz. Anjiyografide ciddi bir koroner arter hastalığı saptanmadı. Etiyolojisi tam olarak net olmamakla birlikte, bu olgu, olası miyokardiyal disfonksiyon taraması için idarubisin alan AML hastalarında miyokard perfüzyon görüntülemesinin düşünülmesi gerektiğini ortaya koymuştur.

Anahtar kelimeler: Akut miyeloid lösemi, miyokardiyal iskemi, miyokardiyal perfüzyon görüntüleme, ekokardiyografi, anjiyografi, koroner arter hastalığı

Address for Correspondence: Chrissa Sioka Asst. Prof., University Hospital of Ioannina, Department of Nuclear Medicine, Ioannina, Greece
Phone: +00302651099377 **E-mail:** csioka@yahoo.com ORCID ID: orcid.org/0000-0002-2184-4945
Received: 26.06.2020 **Accepted:** 18.10.2020

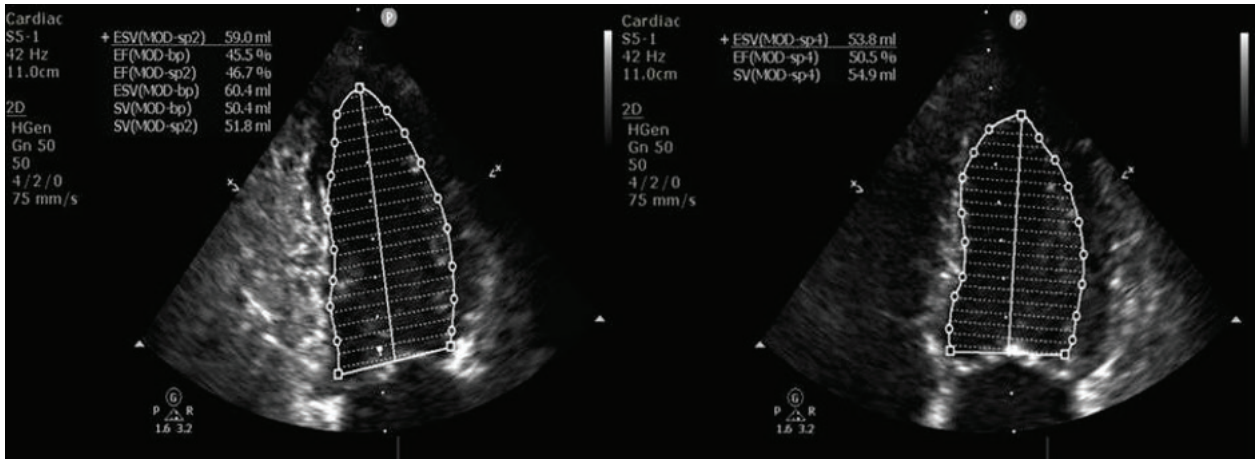

Figure 1. A 56-year-old male patient with atrial fibrillation was diagnosed with acute myeloid leukemia (AML) in August 2019 and treated with idarubicin at 12 mg/m^2/d for 3 days and aracytin at 200 mg/m^2 for 7 days, achieving complete remission. Seven months after the diagnosis of AML, he suffered a left hemispheric stroke, due to atrial fibrillation. Transthoracic echocardiographic study showed mild-moderate systolic left ventricle dysfunction (ejection fraction of 45-50%) with hypokinesia in the basal inferior intraventricular septum and middle inferior and anterior walls.

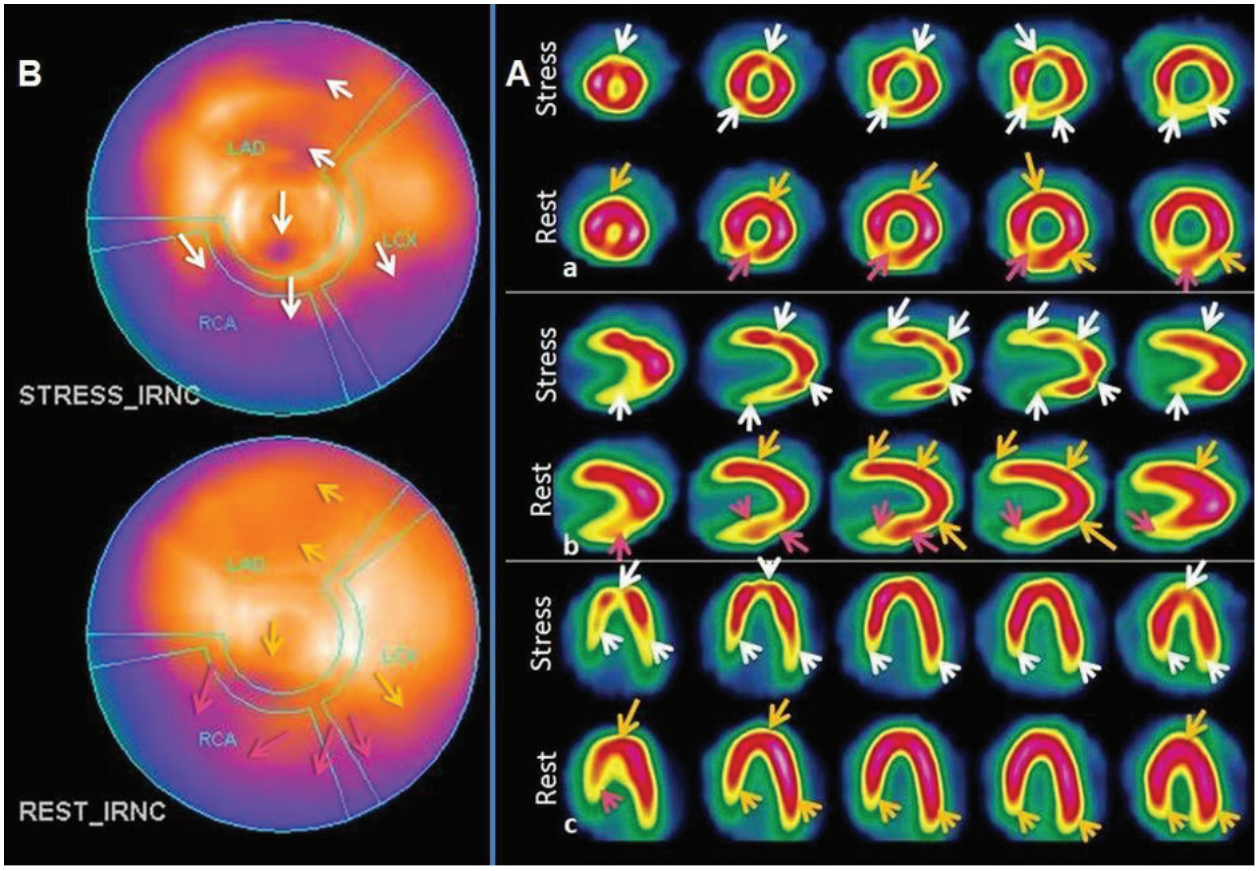

Figure 2. For further evaluation, myocardial perfusion imaging (MPI) was performed using a one-dimensional imaging protocol. No gated single-photon emission computed tomography was applied. Stress protocol and imaging were performed according to published guidelines and as previously reported (1). MPI results were similar to those of echocardiology, as seen in the Bulls-eye MPI image, which depicts the entire myocardium (A) and 3 axis images: a) Short axis, b) vertical axis, and c) horizontal axis (B). White arrows point to the hypoperfused areas during stress: Apical and basal anterior, inferior-septal, median, and basal areas of inferior and inferior-lateral wall, and a segment of the apical cardiac wall (seen in the center, A).

Yellow arrows point to the reversible and pink to the partially reversible areas at rest. The reversible ischemic parts of the myocardium involve the apical and basal anterior and inferior-septal and median areas of the inferior-lateral and apical cardiac walls. Partial reversibility was seen in the remaining hypoperfused areas. The difference in the stress and rest images indicates the reversibility of myocardial ischemia. MPI is an imaging method for myocardial evaluation (2), which detects myocardial ischemia when coronary artery stenosis (CAD) produces a reduction in blood flow of >50%, with a sensitivity and specificity of 86% and 74%, respectively (3).

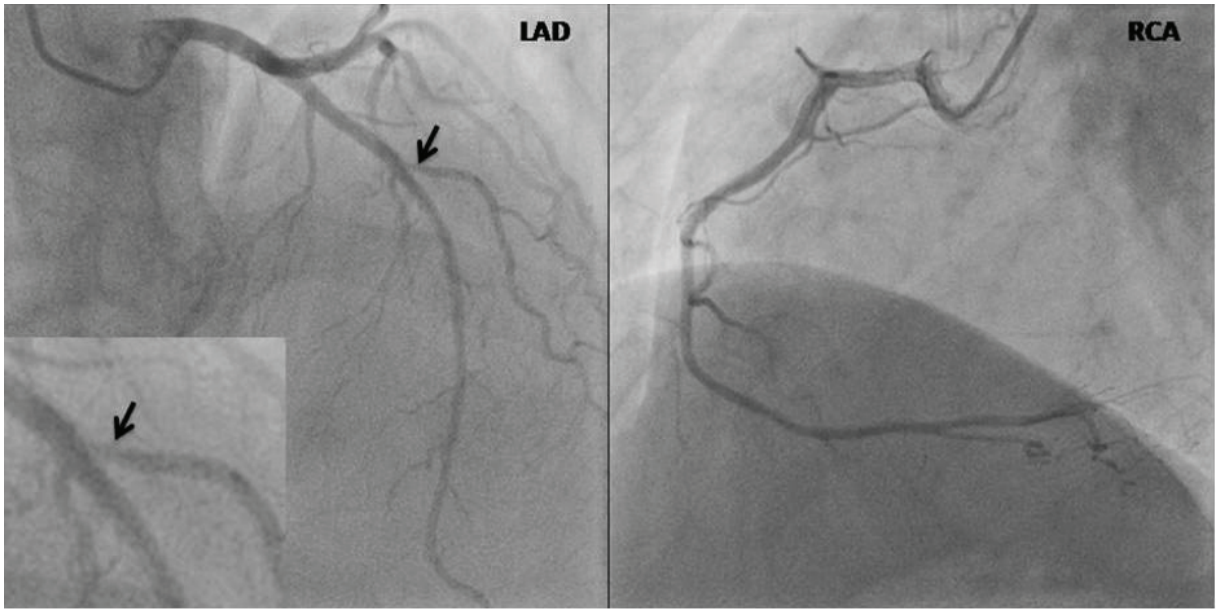

Figure 3. The patient underwent coronary angiography that showed no significant CAD. The left anterior descending artery showed a non-significant (<50%) stenosis. The right coronary artery was also depicted without stenosis. Myocardial dysfunction without significant CAD has occasionally been reported in some medical conditions (4,5). Leukostasis in AML may cause significant CAD (6); however, insufficient hemodynamic stenoses in the coronary angiogram argue against this etiology. Furthermore, the intake of idarubicin, a possible cardiotoxic drug in total doses over 290 mg/m^2 (7), is unlikely to be the main etiology of myocardial ischemia in this patient since the received dose was only 69 mg/m^2. Another contributing factor could have been myocardial ischemia secondary to leukemic cell infiltration, an exceedingly rare and unproven AML complication (8).
In any event, cardiac surveillance with MPI and/or cardiac ultrasonography in patients with AML on idarubicin should be considered to prevent and treat myocardial dysfunction.

Ethics

Informed Consent: Written informed consent was obtained from the patient.

Peer-review: Externally peer-reviewed.

Authorship Contributions

Surgical and Medical Practices: A.B., C.K., C.S., Concept: A.F., E.K., S.G., Design: C.S, C.K., A.B., Data Collection or Processing: E.N., A.F., Analysis or Interpretation: C.K, S.G., E.K., Literature Search: C.S, E.N., E.K., Writing: C.S, C.K.

Conflict of Interest: No conflict of interest was declared by the authors.

Financial Disclosure: The authors declared that this study received no financial support.

References

1. Sioka C, Exarchopoulos T, Tasiou I, Tzima E, Fotou N, Capizzello A, Ragos V, Tsekeris P, Fotopoulos A. Myocardial perfusion imaging with (99 m)Tc-tetrofosmin SPECT in breast cancer patients that received postoperative radiotherapy: a case-control study. Radiat Oncol 2011;6:151.
2. Giannopoulos S, Markoula S, Sioka C, Zouroudi S, Spiliotopoulou M, Naka KK, Michalis LK, Fotopoulos A, Kyritsis AP. Detecting myocardial ischemia with 99mtechnetium-tetrofosmin myocardial perfusion imaging in ischemic stroke. Neurohospitalist 2017;7:164-168.
3. Roberts WC, Bodey GP, Wertlake PT. The heart in acute leukemia. A study of 420 autopsy cases. Am J Cardiol 1968;21:388-412.
4. Sioka C, Papadimitropoulos K, Michalis L, Pappas K, Lakkas L, Fotopoulos A, Dounousi E. Myocardial ischemia with normal coronary angiography in a chronic kidney disease patient. Cardiol J 2019;26:620-621.
5. Kotsalou I, Georgoulias P, Karydas I, Fourlis S, Sioka C, Zoumboulidis A, Demakopoulos N. A rare case of myocardial infarction and ischemia in a cannabis-addicted patient. Clin Nucl Med 2007;32:130-131.
6. Cohen Y, Amir G, Da'as N, Gillis S, Rund D, Polliack A. Acute myocardial infarction as the presenting symptom of acute myeloblastic leukemia with extreme hyperleukocytosis. Am J Hematol 2002;71:47-49.
7. Khan AA, Ashraf A, Singh R, Rahim A, Rostom W, Hussain M, Renner I, Collins NJ. Incidence, time of occurrence and response to heart failure therapy in patients with anthracycline cardiotoxicity. Intern Med J 2017;47:104-109.
8. Prenner SB, Franken AA, Murphy IG, Mikati IA. Rapid reversal of focal left ventricular hypertrophy and systolic dysfunction resulting from myocardial infiltration by acute lymphoblastic leukemia. Circulation 2016;133:678-679.

Interesting Image
Mol Imaging Radionucl Ther 2022;31:66-68 DOI:10.4274/mirt.galenos.2020.26566

Short Latency Radiation Induced Osteosarcoma Detected on ^{18}F-FDG PET/CT Scan in Solitary Plasmacytoma

Soliter Plazmasitomada ^{18}F-FDG PET/BT Görüntülemede Saptanan Radyasyona Bağlı Kısa Latent Dönemde Gelişen Osteosarkom

Sana Munir Gill[1], Aamna Hassan[1], Namra Asghar[1], Usman Ahmad[2], Umm e Kalsoom Awan[2], Imran Khalid Niazi[3]

[1]Shaukat Khanum Memorial Cancer Hospital and Research Centre, Department of Nuclear Medicine, Lahore, Pakistan
[2]Shaukat Khanum Memorial Cancer Hospital and Research Centre, Department of Medical Oncology, Lahore, Pakistan
[3]Shaukat Khanum Memorial Cancer Hospital and Research Centre, Department of Radiology, Lahore, Pakistan

Abstract

^{18}Fluorine-fluorodeoxyglucose (^{18}F-FDG) positron emission tomography/computed tomography (PET/CT) plays a pivotal role in the staging, restaging, and surveillance of various bone tumors, including plasmacytomas and osteosarcomas. Solitary plasmacytomas most frequently occur in the bones and are primarily treated with either surgery or radiotherapy. Radiation-induced osteosarcomas (RIOS) usually develop after a median interval of 11 years between radiation and sarcoma presentation. However, these can rarely present with a short latent period of 4 years or even lesser. In such cases, whole-body imaging plays a vital role in the early detection and management of RIOS. Herein, we present the case of a 29-year-old female patient with solitary plasmacytoma undergoing a follow-up whole-body ^{18}F-FDG PET/CT, which revealed metastatic RIOS after a short latent period.

Keywords: Solitary plasmacytoma, ^{18}F-FDG PET/CT, radiation-induced osteosarcoma

Öz

^{18}Flor-florodeoksiglukoz (^{18}F-FDG) pozitron emisyon tomografisi/bilgisayarlı tomografi (PET/BT), plazmasitomlar ve osteosarkomlar dahil olmak üzere çeşitli kemik tümörlerinin evreleme, yeniden evreleme ve takibinde çok önemli bir rol oynar. Soliter plazmasitomlar en sık olarak kemiklerde görülür ve esas olarak cerrahi veya radyoterapi ile tedavi edilir. Radyasyona bağlı osteosarkomlar (RIOS) genellikle radyasyon ve sarkom prezentasyonu arasındaki ortalama 11 yıllık bir aradan sonra gelişir. Ancak, nadiren 4 yıl veya daha kısa bir latent periyotla da ortaya çıkabilir. Bu gibi durumlarda, tüm vücut görüntüleme, RIOS'nin erken tespiti ve yönetiminde hayati bir rol oynar. Burada, tüm vücut ^{18}F-FDG PET/BT takibi yapılan ve kısa bir latent dönemden sonra metastatik RIOS saptanan soliter plazmasitomu olan 29 yaşında bir kadın hastayı sunuyoruz.

Anahtar kelimeler: Soliter plazmasitoma, ^{18}F-FDG PET/BT, radyasyona bağlı osteosarkom

Address for Correspondence: Aamna Hassan MD, Shaukat Khanum Memorial Cancer Hospital and Research Centre, Department of Nuclear Medicine, Lahore, Pakistan
Phone: +92 42 35905000 **E-mail:** aamnah@skm.org.pk ORCID ID: orcid.org/0000-0003-0026-0729
Received: 08.06.2020 **Accepted:** 24.11.2020

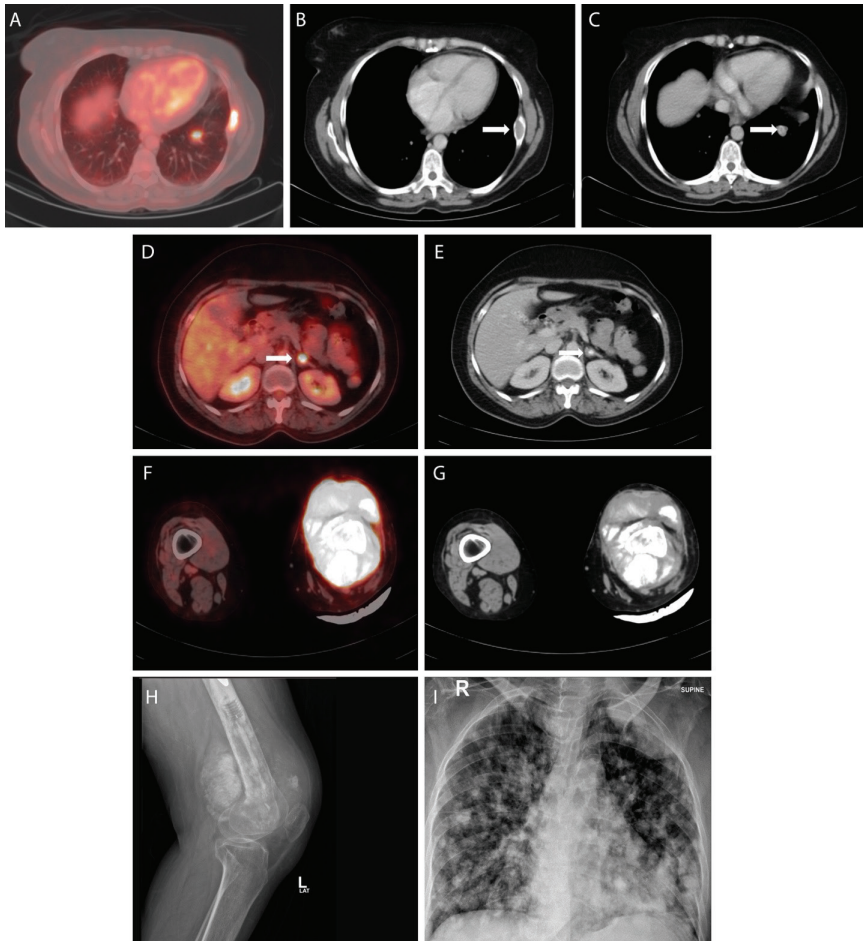

Figure 1. ^{18}Fluorine-fluorodeoxyglucose (^{18}F-FDG) positron emission tomography/computed tomography (PET/CT) has higher sensitivity (89.2%) in localizing second malignancies compared with conventional imaging modalities (23%) (1). This was highlighted in a 29-year-old female patient who presented with two primaries that occurred in the same bone at two different time intervals. She re-presented 4 years after initial treatment with intramedullary cementation/nailing and radiotherapy of the left proximal femur for plasmacytoma. Skeletal survey at re-presentation revealed a new solitary lytic lesion in the skull for which ^{18}F-FDG PET/CT, a non-invasive functional imaging modality, was acquired to optimally identify small lesions that may not be well characterized on magnetic resonance imaging and CT (2). PET/CT showed hypermetabolic lesions in the sternum, left 7th rib (A, B), left parietal bone, and fractured left intramedullary nail. Histopathology of the left proximal femur showed no recurrence. Serum protein electrophoresis showed a faint band in the gamma region, potentially a small paraprotein. Follow-up PET/CT at 2 months showed progression with partially calcified and non-calcified pulmonary nodules (A, C), calcified left adrenal nodule (D, E), and multiple soft tissue lesions along the left distal femur with intra-articular extension (F, G). Radiographs showed a destructive left distal femur lesion (H). Serum Kappa and Lambda levels and ratios were normal.

Plasmacytoma rarely metastasizes, which may lead to the development of multiple myeloma. No obvious histopathological or serological evidence of plasmacytoma/multiple myeloma biopsy of the distal femoral lesion was planned, which showed pleomorphic and atypical spindle cells with osteoid formation. It was positive on immunohistochemistry for special AT-rich sequence-binding protein 2 valuable diagnostic biomarker, which can differentiate between osteosarcoma and its mimickers. Overall findings confirmed the diagnosis of radiation-induced osteosarcoma (RIOS). The patient was later admitted to the emergency department with worsening dyspnea. Chest radiograph showed cannon-ball lesions in both lungs (I). She was then referred to the palliation team for further management.

Nanni et al. (3) were some of the first to suggest the supremacy of ^{18}F-FDG PET/CT over conventional imaging in new lesion detection. Hybrid PET/CT does not only anatomically localize the tumor but also adds further information regarding tumor aggressiveness in its metabolic activity. Osteosarcomas are notorious for being chemoradiotherapy-resistant. Therefore, early detection is imperative for optimal treatment with excision at the initial stages (4). These occur after long latency periods of up to 11 years; however, the possibility of RIOS after short latency periods should always be considered in patients with a radiation therapy history while reviewing ^{18}F-FDG PET/CT. An increased chance of metastatic disease can occur in the case of delayed diagnosis, which is the greatest adverse prognostic factor, especially in the older age group (5).

This case illustrated that reporting clinicians need to be mindful of RIOS development with a short latent period as up to 0.5-5.5% of all sarcomas are caused by radiation, which is commonly seen in osteosarcomas followed by fibrosarcomas (6). Therefore, in the current era of hybrid imaging with new hypermetabolic areas within the radiation field and evidence of distant metastases that do not fit the primary pathology, nuclear physicians should consider the possibility of RIOS.

Ethics

Informed Consent: IRB approval obtained.

Peer-review: Externally and internally peer-reviewed.

Authorship Contributions

Surgical and Medical Practices: A.H., U.A., U.K.A., I.K.N., Concept: S.M.G., A.H., Design: S.M.G., A.H., Data Collection or Processing: S.M.G., A.H., N.A., Analysis or Interpretation: S.M.G., A.H., N.A., I.K.N., U.A., U.K.A., Literature Search: S.M.G., A.H., Writing: S.M.G., A.H.

Conflict of Interest: No conflict of interest was declared by the authors.

Financial Disclosure: The authors declared that this study received no financial support.

References

1. Ali SA, Hamed MAE. The diagnostic efficacy of whole body 18F-FDG PET CT in detection of unexpected second primary malignancy in cancer patients. EJRNM 2017;48:671-676.
2. Zhang X, Guan Z. PET/CT in the diagnosis and prognosis of osteosarcoma. Front Biosci (Landmark Ed) 2018;23:2157-2165.
3. Nanni C, Rubello D, Zamagni E, Castellucci P, Ambrosini V, Montini G, Cavo M, Lodi F, Pettinato C, Grassetto G, Franchi R, Gross MD, Fanti S. 18F-FDG PET/CT in myeloma with presumed solitary plasmocytoma of bone. In Vivo 2008;22:513-517.
4. Rustemeyer P, Micke O, Blasius S, Peters PE. Radiation-induced malignant mesenchymoma of the chest wall following treatment for breast cancer. Br J Radiol 1997;70:424-426.
5. Tsuda Y, Ogura K, Shinoda Y, Kobayashi H, Tanaka S, Kawai A. The outcomes and prognostic factors in patients with osteosarcoma according to age: a Japanese nationwide study with focusing on the age differences. BMC Cancer 2018;18:614.
6. Mavrogenis AF, Pala E, Guerra G, Ruggieri P. Post-radiation sarcomas. Clinical outcome of 52 Patients. J Surg Oncol 2012;105:570-576.

Interesting Image
Mol Imaging Radionucl Ther 2022;31:69-71 DOI:10.4274/mirt.galenos.2020.84755

Hybrid Renal Cortical Imaging with Single Photon Emission Computerized Tomography/Computed Tomography in a Pediatric Patient with Severe Caudal Regression Syndrome

Şiddetli Kaudal Regresyon Sendromu Olan Pediatrik Bir Hastada Tek Foton Emisyonlu Bilgisayarlı Tomografi/Bilgisayarlı Tomografi ile Hibrid Renal Kortikal Görüntüleme

Selin Kesim, Halil Turgut Turoğlu, Salih Özgüven, Tunç Öneş, Tanju Yusuf Erdil

Marmara University Faculty of Medicine, Department of Nuclear Medicine, İstanbul, Turkey

Abstract

Caudal regression syndrome (CRS) or sacral agenesis is a rarely seen malformation with a varying degree of structural abnormalities, including multiorgan system dysfunctions, reported with higher incidence among children of mothers with diabetes, as in this case. Spinal anomalies can range from coccyx hemiagenesis to the total absence of lower lumbar vertebrae and sacrum in most severe cases. Herein, we have presented a 9-year-old patient with CRS who had renal failure. Technetium-99m dimercaptosuccinic acid renal scintigraphy revealed bilaterally non-functioning kidneys with no renal cortical uptake. Renal anomalies in CRS with vertebral, anorectal, cardiac, trachea-esophageal, renal, and limb anomalies association include one-sided renal agenesis, multicystic dysplastic kidneys, and ureter duplications.

Keywords: Caudal regression syndrome, sacral agenesis, VACTERL association, Tc-99m DMSA renal scintigraphy, SPECT/CT

Öz

Kaudal regresyon sendromu (KRS) veya sakral agenezi, çoklu organ sistemlerini etkileyen, yapısal anomaliler ile seyreden ve olgumuzda olduğu gibi diyabetik annelerin çocukları arasında daha yüksek sıklıkta görülen nadir bir malformasyondur. Vertebral anomaliler koksiksin kısmi agenezisinden ağır olgularda sakral ve/veya lomber vertebraların total agenezisine kadar değişebilmektedir. Burada, teknesyum-99m DMSA böbrek sintigrafisinde bilateral kortikal aktivite tutulumu izlenmeyen, non-fonksiyonel böbrekler saptanan KRS tanılı 9 yaşında bir pediatrik vaka sunulmaktadır. Tek taraflı renal agenezi, multisistik displastik böbrekler ve toplayıcı sistem duplikasyonları gibi renal anomaliler KRS ile vertebral, anorektal, kardiyak, trakeoözafagial, renal ve ekstremite anomalileri birlikteliğinde görülebilmektedir.

Anahtar kelimeler: Kaudal regresyon sendromu, sakral agenezi, VACTERL asosiyasyonu, Tc-99m DMSA böbrek sintigrafisi, SPECT/BT

Address for Correspondence: Selin Kesim MD, Marmara University Faculty of Medicine, Department of Nuclear Medicine, İstanbul, Turkey
Phone: +90 216 396 86 48 **E-mail:** selinkesim@yandex.com ORCID ID: orcid.org/0000-0002-6164-9781
Received: 04.08.2020 **Accepted:** 24.11.2020

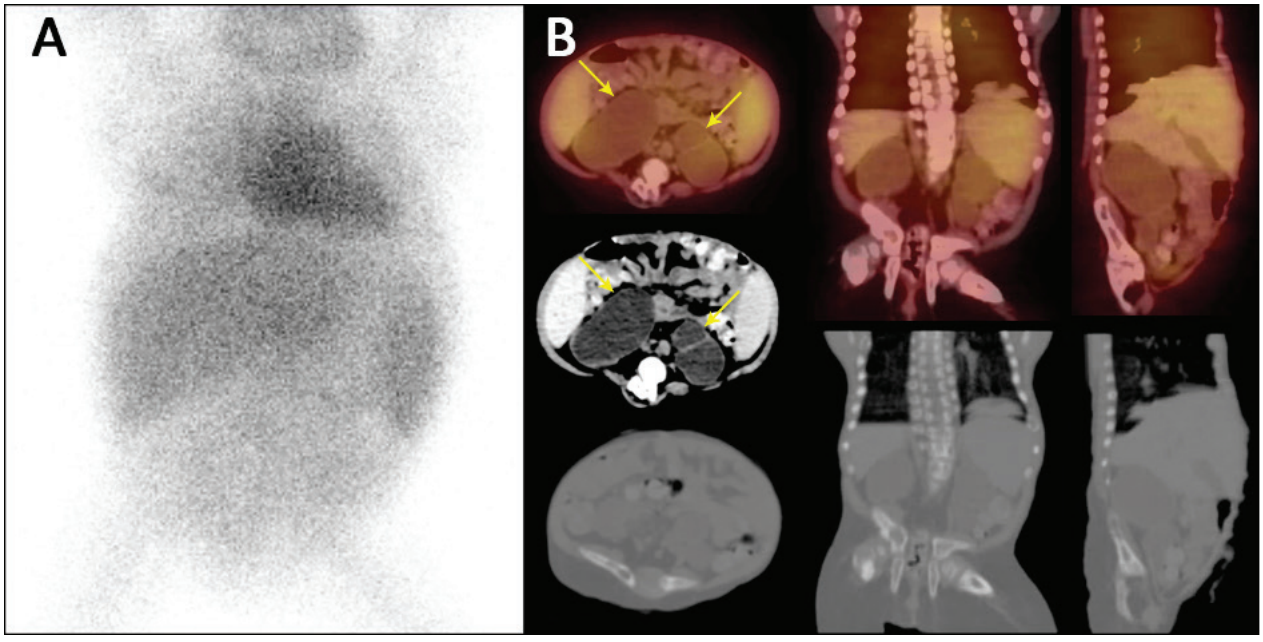

Figure 1. A 9-year-old female patient, who has dysmorphic extremities, growth retardation, congenital scoliosis, rectal, urethral, and sacral agenesis, was diagnosed with caudal regression syndrome (CRS) with a possible etiology of maternal diabetes. Elevated blood urea nitrogen (33 mg/dL) and serum creatinine (1.85 mg/dL) values necessitated the initiation of dialysis. She was referred to technetium-99m-labeled dimercaptosuccinic acid (Tc-99m DMSA) renal scintigraphy to evaluate renal functions before possible kidney transplantation. Tc-99m DMSA renal parenchymal scintigraphy revealed bilaterally "blood pool" image and increased background activity with no renal cortical uptake of Tc-99m DMSA (A). The hybrid single-photon emission computerized tomography/computed tomography (SPECT/CT) images demonstrated both kidneys having a cystic pouch appearance (arrows) suggestive of bilateral multicystic dysplastic kidneys (MCDK) with no Tc-99m DMSA uptake in both renal parenchymas consistent with bilaterally non-functioning kidneys, accompanied by bilaterally tortuous and dilated ureters. SPECT/CT also depicted thoracolumbar scoliosis and lumbosacral agenesis involving the bodies and posterior elements of the fourth and fifth lumbar vertebrae (B).

CRS is a rare, neural tube defect that comprises varying degrees of musculoskeletal, gastrointestinal, genitourinary, and cardiovascular system anomalies (1). Its incidence is reported as approximately 0.01-0.05 per 1,000 births, frequent among children of mothers with diabetes (2). Spinal anomalies, which is a characteristic component of CRS, can vary from coccyx hemiagenesis to the total absence of lower lumbar vertebrae and sacrum in severe cases (3). Four types of CRS exist according to the classification of Renshaw (4). Type IV CRS shows variable lumbar and total sacral agenesis, with a caudal endplate of the lowest vertebra resting above the fused iliac bones or iliac amphiarthrosis (4). To fulfill the so-called CRS- vertebral, anorectal, cardiac, trachea-esophageal, renal, and limb anomalies (VACTERL) entity, a minimum of three of six VACTERL anomalies must be present (5). A few cases have been presented on Tc-99m methylene diphosphonate bone scintigraphy in the literature; however, to the best of our knowledge, our case is the first to present Tc-99m DMSA scintigraphy images for CRS-VACTERL (6,7). Urologic anomalies are difficult to identify on clinical examination and form the primary cause of morbidity and mortality. Renal anomalies in CRS-VACTERL association include unilateral renal agenesis, MCDK, and duplication of the collecting system (3). MCDK and hydronephrosis (HN) in newborns both present as fluid-filled masses. Their differential diagnosis is made by the absence (in MCDK) or the presence (in HN) of radiotracer in the fluid. Our case is the late-onset hydronephrotic form of MCDK. Tc-99m DMSA renal scan is a reliable tool for non-invasive diagnosis of acute and/or chronic kidney injury in children, thus improving the prognosis (8). Hybrid imaging with SPECT/CT technique may help achieve better diagnostic accuracy and impact patient management, as it allows the anatomical correlation of functioning renal parenchymal tissue.

Ethics

Informed Consent: We have obtained all appropriate patient consent forms. In the form the patient has given her consent for her images and other clinical information to be reported in the journal.

Peer-review: Externally peer-reviewed.

Authorship Contributions

Surgical and Medical Practices: S.K., H.T.T., S.Ö., T.Ö., T.Y.E., Concept: S.K., H.T.T., Design: S.K., H.T.T., Data Collection or Processing: S.K., H.T.T., Literature Search: S.K., H.T.T, Writing: S.K., H.T.T.

Conflict of Interest: No conflict of interest was declared by the authors.

Financial Disclosure: The authors declared that this study received no financial support.

References

1. Sharma P, Kumar S, Jaiswal A. Clinico-radiologic Findings in Group II caudal regression syndrome. J Clin Imaging Sci 2013;3:26.

2. Zaw W, Stone DG. Caudal regression syndrome in twin pregnancy with type II diabetes. J Perinatol 2002;22:171-174.
3. Cunningham BK, Khromykh A, Martinez AF, Carney T, Hadley DW, Solomon BD. Analysis of renal anomalies in VACTERL association. Birth Defects Res A Clin Mol Teratol 2014;100:801-805.
4. Renshaw TS. Sacral Agenesis. The Pediatric Spine -Principles and Practice. Raven Press, New York. 1994;1:2214.
5. Fayyaz A, Ilyas M, Iqbal O. Pre-natal diagnosis of caudal regression syndrome. J Coll Physicians Surg Pak 2007;17:425-426.
6. Karacalioglu AO, Soylu K, Emer O, Ayan A, Ozguven M. Incidental finding of sacral hemiagenesis on the (99m)Tc-MDP bone scan as a casual regression syndrome type II. Hell J Nucl Med 2008;11:175-178.
7. Nguyen BD, Civelek AC. Bone scintigraphy of caudal regression syndrome. Clin Nucl Med 1996;21:802-804.
8. Harisankar CN, Mittal BR, Bhattacharya A, Sunil HV, Singh B, Rao KL. Potential diagnostic role of renal scintigraphy in the management of patients with high anorectal malformation. Hell J Nucl Med 2009;12:260-265.

Interesting Image
Mol Imaging Radionucl Ther 2022;31:72-74 DOI:10.4274/mirt.galenos.2021.28190

Diffuse Large B-Cell Non-Hodgkin Lymphoma Involving Multiple Different Organs in a Young Adult with ^{18}F-FDG PET/CT

Genç Erişkinde ^{18}F-FDG PET/BT ile Farklı Organları İçeren Diffüz Büyük B-Hücreli Non-Hodgkin Lenfoma Tutulumu

Esra Arslan[1], Tamer Aksoy[1], Göksel Alçın[1], Nilay Ermantaş[2], Yasemin Özlük[3], Gülçin Yeğen[3], Tevfik Fikret Çermik[1]

[1]University of Health Sciences Turkey, İstanbul Training and Research Hospital, Clinic of Nuclear Medicine, İstanbul, Turkey
[2]University of Health Sciences Turkey, Haseki Training and Research Hospital, Clinic of Hematology, İstanbul, Turkey
[3]İstanbul University, İstanbul Faculty of Medicine, Department of Pathology, İstanbul, Turkey

Abstract

Extranodal-multiorgan involvement is rarely presented in diffuse large B-cell non-Hodgkin lymphoma. ^{18}Fluorine-fluorodeoxyglucose positron emission tomography/computed tomography findings of a 22-year-old female patient with supra/infra-diaphragmatic nodal and skeletal involvements and thyroid, pancreas, right breast, bilateral renal, and ovarian involvements were presented.

Keywords: Extranodal-multiorgan involvement, ^{18}F-FDG, PET/CT, diffuse large B-cell non-Hodgkin lymphoma

Öz

Ekstranodal-multiorgan tutulumu, diffüz büyük B-hücreli non-Hodgkin lenfomada (DBBHNHL) nadiren görülmektedir. Yirmi iki yaşındaki kadın olguda ^{18}flor-florodeoksiglukoz pozitron emisyon tomografi/bilgisayarlı tomografi ile DBBHNHL'nin supra/infra-diyafragmatik lenf nodu, kemik tutulumu ile tiroid, pankreas, sağ meme, bilateral renal ve over tutulumu gösterildi.

Anahtar kelimeler: Ekstranodal-multiorgan tutulumu, ^{18}F-FDG, PET/BT, diffüz büyük B hücreli non-Hodgkin lenfoma

Address for Correspondence: Esra Arslan Asst. Prof., University of Health Sciences Turkey, İstanbul Training and Research Hospital, Clinic of Nuclear Medicine, İstanbul, Turkey
Phone: +90 212 459 68 02 **E-mail:** dresraarslan@gmail.com ORCID ID: orcid.org/0000-0002-9222-8883
Received: 11.11.2020 **Accepted:** 09.01.2021

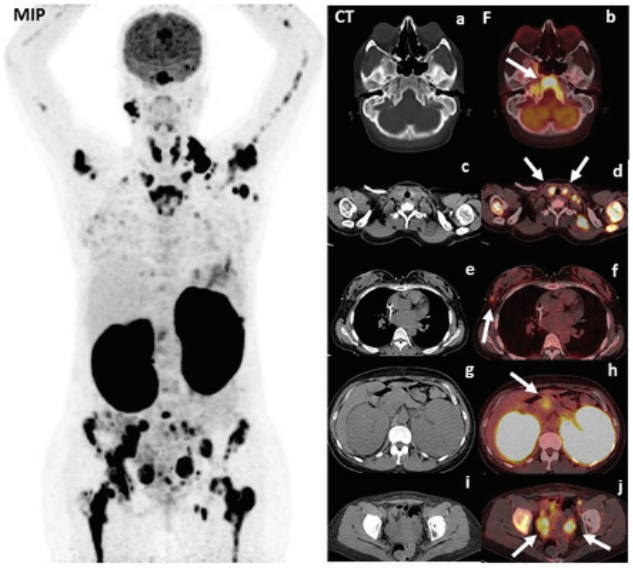

Figure 1. A 22-year-old female patient was admitted to the hospital with weakness and shortness of breath. Dialysis was started when the creatinine level was 10.95. Ultrasonography was performed, which revealed a significantly increased size of both kidneys without calculus, mass, and ectasia. A kidney biopsy was performed and reported as diffuse large B-cell non-Hodgkin lymphoma (DLBCNHL). Bone marrow biopsy was performed and large B-cell atypical mononuclear cell infiltration was detected. ^{18}Fluorine-fluorodeoxyglucose (^{18}F-FDG) positron emission tomography/computed tomography (PET/CT) imaging was performed for staging. The maximum intensity projection (MIP) image and transaxial slices revealed focal ^{18}F-FDG uptake in the upper outer right quadrant of the right breast and at the head of the pancreas and diffuse intensive ^{18}F-FDG uptake in the thyroid, kidneys, and ovaries. Along with multiple tumoral involvements in the supra/infra-diaphragmatic lymph nodes, diffuse and focal increased multiple ^{18}F-FDG accumulations were observed in the skeleton in favor of bone marrow involvement. Axial fusion (F) images revealed increased ^{18}F-FDG uptake at skull base bone marrow, thyroid lobes, head of the pancreas, bilateral kidneys, and ovaries F (b, d, f, h, j), and corresponding CT slices (a, c, e, g, i) revealed accompanying morphological findings MIP images.

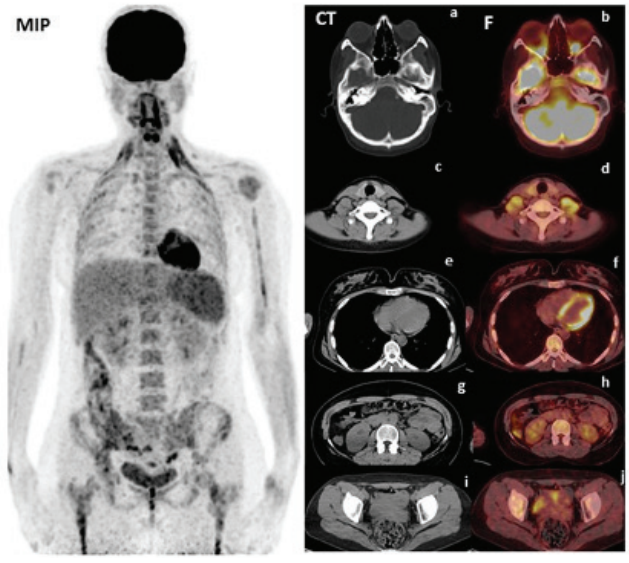

Figure 2. The rituximab, cyclophosphamide, doxorubicin, vincristine, and prednisone protocol was initiated by an adjusted renal cyclophosphamide dosage. After three cycles of chemotherapy, MIP image and axial F images (b, d, f, h, j) demonstrated a significant decrease in all nodal and extranodal involvements, and corresponding CT slices (a, c, e, g, i) revealed accompanying morphological improvements.

^{18}F-FDG PET/CT was established as the best technique for monitoring patients with extranodal involvement in HL and most NHL and must be taken into account in every stage of the disease since it can change the prognosis and treatment (1,2). A study that evaluated extranodal involvements in PET/CT among lymphomas revealed that the most common organ involvements were found in DLBCNHL, and the most common organ involvement in NHL has been reported in the gastrointestinal tract (3). Uccella et al. (4) systematically reviewed the morphological, immunohistochemical, and genetic characteristics of lymphoproliferative disorders of different endocrine organs. ^{18}F-FDG PET/CT findings of Burkitt's lymphoma involved the spleen, brain, bones, and 4 organs in the endocrine system, including thyroid, adrenal, pancreas, and testicle, which was presented in a 21-year-old patient (5). An 11-year-old female patient with anaplastic large cell lymphoma had seven different organ involvements with ^{18}F-FDG PET/CT, which presented the muscle, bone, kidney, pancreas, ovary, lymph nodes, and central nervous system (6). Another extranodal involvement of DLBCNHL, involving left orbit and ethmoid sinus, was shown with ^{18}F-FDG PET/CT (7). Puranik et al. (8) reported a case of NHL with four rare extranodal sites, including the adrenal, peripheral nerves, pancreas, and prostate, detected with ^{18}F-FDG PET/CT.

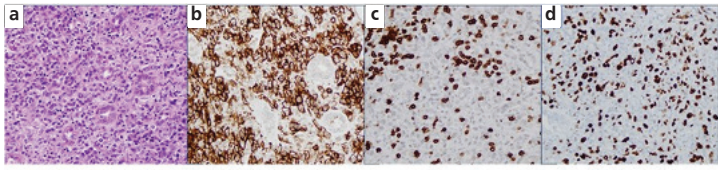

Figure 3. Renal biopsy revealed interstitial infiltration by large atypical lymphoid cells hematoxylin and eosin (a). Immunohistochemically atypical cells were positive for CD20 (b) and negative for CD3 (c). Ki67 proliferation index was high (d).

Ethics

Informed Consent: Written informed consent was obtained.

Peer-review: Externally peer-reviewed.

Authorship Contributions

Surgical and Medical Practices: Y.Ö., G.Y., N.E., Concept: E.A., T.A., G.A., T.F.Ç., Design: E.A., T.F.Ç., Data Collection or Processing: E.A., T.A., G.A., Analysis or Interpretation: E.A., T.F.Ç., Literature Search: T.A., E.A., Writing: E.A., T.A., T.F.Ç., N.E.

Conflict of Interest: No conflict of interest was declared by the authors.

Financial Disclosure: The authors declared that this study received no financial support.

References

1. Paes FM, Kalkanis DG, Sideras PA, Serafini AN. FDG PET/CT of extranodal involvement in non-Hodgkin lymphoma and Hodgkin disease. Radiographics 2010;30:269-291.
2. Buchpiguel CA. Current status of PET/CT in the diagnosis and follow up of lymphomas. Rev Bras Hematol Hemoter 2011;33:140-147.
3. Zucca E, Conconi A, Cavalli F. Treatment of extranodal lymphomas. Best Pract Res Clin Haematol 2002;15:533-547.
4. Uccella S, Magnoli F, Amaglio C, Sessa F, La Rosa S. The spectrum of lymphoproliferative disorders in endocrine organs: from histology to molecular genetics. Diagn Histopathol 2019;25:5:166-177.
5. Wen Z, Zhuang H. Burkitt's lymphoma involving multiple hormone-producing organs on FDG PET/CT. Clin Nucl Med 2019;44:995-997.
6. Zhang M, Yang X, Wang W, Yang J. Anaplastic large cell lymphoma involving 7 different organs in a pediatric patient demonstrated by FDG PET/CT. Clin Nucl Med 2020;45:255-257.
7. Natarajan A, Chandra P, Purandare N, Agrawal A, Shah S, Puranik A, Rangarajan V. Role of fluorodeoxyglucose positron emission tomography/computed tomography in various orbital malignancies. Indian J Nucl Med 2018;33:118-124.
8. Puranik AD, Agrawal A, Purandare NC, Shah S, Rangarajan V. Four rare extranodal sites seen on FDG PET/CT in a single patient of disseminated lymphoma. Indian J Med Paediatr Oncol 2013;34:101-103.